Charles University in Prague
Faculty of Mathematics and Physics

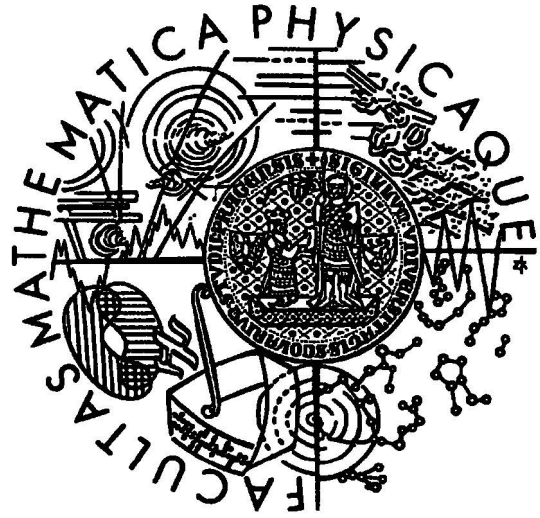

Instabilities of f-electron States in Compounds Based on Light Rare Earths

Doctoral thesis

Matúš Mihalik

Supervisor: Prof. RNDr. Vladimír Sechovský, DrSc.

8th September 2008

Acknowledgment

This thesis would not be possible to arise to the present form without help of many people whom I would like to say my best thanks.

My great thanks belong to my supervisor, Prof. RNDr. Vladimír Sechovský, DrSc. He always supported me during my study and work on my thesis. He helped me to understand the studied problems, he suggested me which additional experiments should I perform to better understand the studied problematic, also he assisted me with solving of the many problems I had, anytime I needed.

I also wish to express my gratitude to my adjunct supervisor, Dr. Hideaki Kitazawa, who supervised me during my one-year stay in National Institute for Materials Science (NIMS) in Tsukuba. His everyday care and support made my stay in Japan very fruitful and successful. Also he have taught me how to grow single crystals by float zone technique and he helped me to improve my skills in growing the single crystals by Czochralski technique. Also I am grateful for his assistance in the personal life in Japan during my stay in NIMS.

Also I am grateful to other members of Department of Condensed Matter Physics for their help during my PhD. study: Doc. RNDr. Pavel Svoboda, CSc., Doc. RNDr. Ladislav Havela, CSc., RNDr. Stanislav Daniš, PhD., Mgr. Zdeněk Matěj, RNDr. Klára Uhlířová; Mgr. Jiří Pospíšil, RNDr. Jan Prokleška PhD., RNDr. Jiří Prchal Ph.D., RNDr. Jana Poltierová Vejpravová, Ph.D., Štěpán Sechovský and Mgr. Kateřina Mikšová

Also I am grateful to members of Neutron Scattering group in NIMS and to other people in NIMS for their helps during my stay in NIMS: Dr. Andreas Dönni, Dr. Hiroyuki Suzuki, Dr. Hiroaki Mamiya, Dr. Naohito Tsujii, Dr. Masashi Hase, Dr. Noriki Terada, Hara Keiko and Akiko Kikkawa.

My gratitude also belongs to Ing. Josef Šebek Ph.D. and Ing. Eva Šantavá CSc. for their help with the experiments in the Joint Laboratory of Magnetic Studies and for discussions about many practical aspects of the experiments. This discussions made my experiments much easier to perform.

Also I would like to thank Dr. T. Komatsubara for providing the single crystal of CeRhSn and RNDr. Slavomír Gabáni Ph.D. for performing the experiment on LaRhSn in ^{3}He^{4}He refrigerator.

My thanks go also to my father RNDr. Marián Mihalik for a fruitful discussion concerning the experimental results and to Ing. Jiří Kamarád CSc. for his teaching me how to use the pressure cells, what should I be aware of and how should I understand the pressure-induced effects in the matter.

I wish to express a special thank to my wife Lucka. This thesis could not be finished without her every-day care and understanding to my work.

Contents

Chapter 1

Introduction

One of the motivations for the study of the ternary rare earth-based (RE) intermetallic compounds (RE + p- and d-metal) is that their properties are very different from the properties of the each individual components. As these compounds crystallize in the variety of the crystal structures and the crystal structures in most cases do not depend on the rare earth ion but depend on the used $p-$ and $d-$metals, one should study the evolution of the physical properties of different RE ions, but in the same crystallographic surroundings. Another motivation is that the physic of these intermetallic compounds is still not fully understood from the theoretical point of view, so experimental physicists can provide the experimental results which should test different theories in this field of physics. Also the complexity of some phase diagrams and the presence of an interesting phenomena like quantum critical point, non-Fermi liquid behavior and fluctuating valence in these compounds attracted our interest.

As the studied compounds crystallize in the crystallographic structures in which the high spatial anisotropy of the physical properties is expected, it is highly needed to study the physical properties of these compounds on the single-crystalline samples. That's why the basic aim of the thesis was to prepare the single crystals and then to measure the physical properties with respect to the crystallographic orientation of the grown single crystals. We have succeeded to prepare the majority of the studied compounds as a single crystals. Most of the prepared single crystals we have prepared for the first time, which makes them to be the world unique.

We have chosen to study the RERhSn (RE = La, Ce, Pr and Nd); REPdSn (RE = La, Pr and Nd) and REIr$_2$Si$_2$ (RE = La, Ce and Pr) series. We have measured the specific heat, magnetization, magnetic susceptibility and resistivity of these compounds with respect to the main crystallographic axes, which reflects the anisotropy in the compounds. We have chosen the RERhSn series because the results in the literature for this series are quite in the contradiction, especially in the case of NdRhSn. The REPdSn series has been chosen because the Pr- and Nd-based compounds are antiferromagnetically ordered in the ground state and in the case of NdPdSn the antiferromagnetic structure is quite complex. In the case of LaPdSn we have supposed that the compound should become superconducting, but

we have found no reference of the superconductivity in the previously published literature. We have prepared $LaIr_2Si_2$ only as a nonmagnetic analogue to the $CeIr_2Si_2$ and $PrIr_2Si_2$. As it seems that the majority of the $REIr_2Si_2$ compounds exhibit the polymorphism, the study of $CeIr_2Si_2$ and $PrIr_2Si_2$ was also focused on the polymorphism in the compound: we have performed the detailed study of magnetism in these two compounds with respect to the two different crystallographic phases.

Thesis organization

Chapter 2 deals with the basic theory, which can be applied for the RE-based intermetallic compounds. Chapter 3 is focused firstly on the general description of the used experimental methods and then to used experimental apparatuses. This chapter also describes the experimental setups, which we have used during the experiments. The most important part of the thesis is chapter 4 in which we summarize the the experimental results obtained on the studied materials. This chapter is divided into two sections. The first section is focused on the $RETX$ compounds and is further divided according the crystal structures of studied compounds. The second section is focused on RET_2X_2 compounds and is further divided according to the studied compounds. The chapter 5 briefly discuss the results obtained in this thesis and all results are summarized in the chapter 6 together with the suggestion of possible directions in the future investigation. At the end of thesis we have also added the Appendix A and B in which we have summarized the basic crystallographic parameters for the $RETX$ and RET_2X_2 compounds, respectively.

Chapter 2

Theoretical background

2.1 Rare earths

The elements between lanthanum (Z = 57) and lutetium (Z = 71) together with scandium (Z = 21) and yttrium (Z = 39) are called for historical reasons rare earths. In this work we will deal only with a subgroup of rare earths, namely with the elements from lanthanum to neodymium (Z = 60) and we will use attribution RE for these elements. These elements have usually in the crystal electronic configuration:

$$[Xe]6s^2 5d^1 4f^N \tag{2.1}$$

The $6s^2$ and $5d^1$ wave functions are quite spread into the space, which result to overlapping of $6s^2$ and $5d^1$ wave functions from different atoms and to forming the valence band from these two energy states. That's why the valency of RE ions is mainly 3+ (the exceptions might be Ce, Eu, Yb). The energy of $4f^N$ states is lower than the energy of $6s^2$ and $5d^1$ states and the $4f^N$ wave functions have much smaller radial extend than the typical RE – RE distance. That's why the $4f^N$ states remain localized on the atom and are not influenced by $4f^N$ state from another atom. In case of RE the $4f^N$ states are responsible for the magnetism so one will deal with the magnetism caused by the localized magnetic moments. The situation is however quite different for $5f^N$ states (we will not deal in details with this states) for which we can find every behavior from the localized one to itinerant one.

As the $4f$ level of a RE ion is not directly influenced by the neighboring atoms, the states of the $4f$ electrons depend on their interaction with the charge of nucleus, other $4f$ electrons and other filled shells; every $4f$ electron feels the potential from each other electron in the atom. Assuming, that the nucleus of the ion is at rest, the generic nonrelaticistic hamiltonian is:

$$\widehat{H}_{ion} = \sum_{i=1}^{N}\left(-\frac{\hbar^2}{2m_e}\nabla_i^2\right) - \sum_{i=1}^{N}\frac{Ze^2}{r_i} + \sum_{j>i}^{N}\frac{e^2}{|\mathbf{r}_i - \mathbf{r}_j|} \tag{2.2}$$

where the summations run over all coordinates of all electrons. The first term in 2.2 represents the kinetic energy of electrons, the second term represent the Coulomb attraction between nucleus and electrons and the third term represent the Coulomb repulsion between two electrons. There exist no exact solution of Schrödinger equation with $\widehat{H}_{ion}$ for systems with more than one electron. But in case of RE atoms we can approximate $\widehat{H}_{ion}$ using the central field approximation. Assumption of the central field approximation is that each f electron moves independently in a spherically symmetric effective potential $-U(\mathbf{r}_i)/e$ created by nucleus and all other electrons. Than:

$$\widehat{H}_0 = -\sum_{i=1}^{N}\left(\frac{-\hbar^2}{2m_e}\nabla^2 + U\left(\mathbf{r}_i\right)\right) \tag{2.3}$$

The sum is over the all electrons in f^N shell. The eigenfunctions of hamiltonian $\widehat{H}_0$ are of the form:

$$\psi_{nlm_lm_s}(\mathbf{r},\sigma) = R_{nl}(\mathbf{r},\sigma)Y_{lm_l}(\theta,\phi)\chi_{m_s} \tag{2.4}$$

where $R_{nl}(\mathbf{r},\sigma)$ is the radial wave function, χ_{m_s} is the one electron spinor function and $Y_{lm_l}(\theta,\phi)$ is the spherical harmonics.

Equation 2.3 is good starting point for examining the $4f$ states, however in real case one should add another terms, which behaves as an perturbation to $\widehat{H}_0$. The most important corrections in case of $4f$ ions which we will discuss are correlation interaction ($\widehat{H}_{corr}$); spin-orbit interaction ($\widehat{H}_{LS}$) and crystal field interaction ($\widehat{H}_{CF}$). Then the total hamiltonian for RE ion will be:

$$\widehat{H} = \widehat{H}_0 + \widehat{H}_{corr} + \widehat{H}_{LS} + \widehat{H}_{CF} \tag{2.5}$$

The perturbations in equation 2.5 are not necessary sorted from the biggest to the smallest perturbation. In case of RE compounds we can observe the so called weak crystal field interaction, in which the correlation interaction is stronger than spin-orbit interaction and crystal field interaction is the weakest (weak crystal field). The second possibility is the case, in which the correlation interaction is stronger than crystal field interaction and the spin-orbit interaction is the weakest one (intermediate crystal field). The third possibility in which the crystal field interaction is strongest from all perturbations (strong crystal field) is not common in RE compounds. It is common mainly for the elements with unfilled $4d$ and $5d$ orbitals.

Correlation interaction

The correlation interaction has its origin in the principle that identical particles are indistinguishable. The hamiltonian for this interaction is:

$$\widehat{H}_{corr} = \sum_{i<j}\frac{e^2}{r_{ij}} - \sum_{i=1}^{N}V_i(\mathbf{r}) \tag{2.6}$$

This interaction is the origin of splitting of the states into so-called terms. Each term is characterized by the orbital ($\mathbf{L} = \sum \mathbf{l}_i$) and spin ($\mathbf{S} = \sum \mathbf{s}_i$) number. The operators $\widehat{\mathbf{L}}^2$, $\widehat{\mathbf{S}}^2$, $\widehat{\mathbf{L}}_\mathbf{z}$ and $\widehat{\mathbf{S}}_\mathbf{z}$ commute with $\widehat{H}_{corr}$.

Each term remains (2L+1)(2S+1) degenerate. This degeneration can be partly removed by other perturbations in equation 2.5. The lowest-energy term can be defined due to first and second Hund's rule [1]:

1. The system of n electrons have the lowest energy, when spins of these electrons have the same direction. So the total spin is maximal.

2. The total orbital angular momentum of the lowest–lying states has the largest value in consistency with Hund's first rule and with the Pauli exclusion principle[1].

Spin-orbit interaction

The spin-orbit interaction is the consequence of relativistic effects and originates from the correlation between the electron spin and its own orbital moment. This interaction is linear with respect to $\widehat{S}$:

$$\widehat{H}_{LS} = \xi \widehat{L}\widehat{S} \tag{2.7}$$

where ξ is the effective spin-orbit constant. The consequence of the equation 2.7 is, that $\mathbf{L}$ and $\mathbf{S}$, are not any more good quantum numbers and have to be combined to the total angular momentum $\mathbf{J} = \mathbf{L}+ \mathbf{S}$ (Russel–Saunders Coupling). The spin-orbit interaction splits terms into so-called multiplets, according to the total angular momentum $\mathbf{J}$. The energy of this splitting is $1/2\lambda$ J(J+1). Each multiplet remains (2J+1)-fold degenerate and the ground state multiplet can be determined from the third Hund's rule, which determine the value of J:

$$\begin{aligned} \text{J} &= |\text{L - S}| \text{ for } n < (2l+1); \\ \text{J} &= \text{L + S for } n \geq (2l+1) \end{aligned}$$

Crystal field

If we insert the free ion into the crystal lattice the ion will feel the electric field from the other ions and electrons. This field we call crystal field. The crystal field, which acts on the ion reflects the crystallographic point symmetry at the position of ion and is able to partly or totally remove the (2J+1)-fold degeneracy. In the first approximation the crystal field potential can be computed using point-charge model:

$$V_{CF}(\mathbf{r}) = \sum_j \frac{q_j}{|\mathbf{R}_j - \mathbf{r}|} \tag{2.8}$$

[1]Pauli exclusion principle: There can not be two fermions in the same state (with the same all quantum numbers)

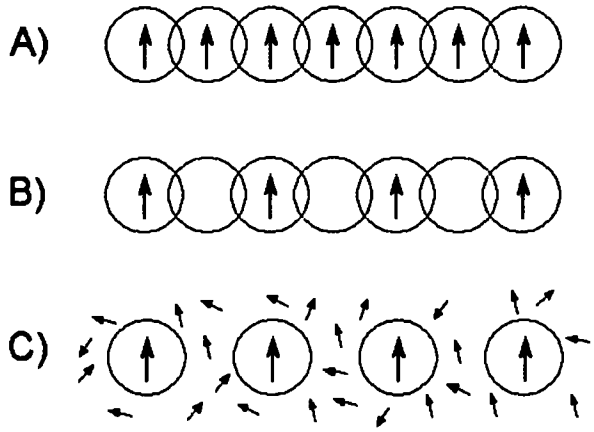

Figure 2.1: *The types of exchange interactions: a) the direct exchange; b) the superexchange in which the magnetic ions interact via the overlapping with the same nonmagnetic ion; c) indirect exchange mediated by interactions with the conduction electrons. Figure taken from [1]*

where q_j is the electric charge at position $\mathbf{R}_j$ and hence the crystal field hamiltonian can be expressed as:

$$\widehat{H}_{CF} = \sum_i q_i V_{CF}^i \tag{2.9}$$

where q_i runs over all $4f$ electrons. Hutching et al. [2] has revriten the hamiltonian 2.9 into more convenient form in which the sum over the $4f$ electrons and over the surrounding electric charges is replaced by crystal field parameters B_j^i and Steven's operators $\widehat{O}_j^i$:

$$\widehat{H}_{CF} = \sum_{i,j} B_j^i \widehat{O}_j^i \tag{2.10}$$

the crystal field parameters have to be found experimentally or calculated using *ab initio* calculations [3], while Stevens operators are tabulated operators and can be found for example in [2]. The number of parameters in equation 2.10 is restricted. The hermicity and time-reversal invariance of $\widehat{H}_{CF}$ restrict l to be even. Another restriction for f-electron systems is $m \leq l$; $l \leq 6$; and there are another restrictions given by the crystallographic point symmetry in the position of studied ion.

2.2 Magnetic exchange interactions

The magnetic ordering has its origin in the magnetic exchange interactions, which are cooperative effects of many atoms. There are few types of different magnetic exchange interactions: direct exchange; indirect exchange (for example RKKY type - interaction

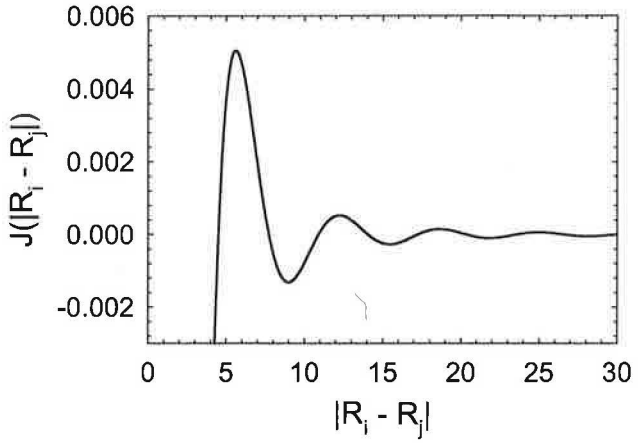

Figure 2.2: *The character of RKKY interaction.*

named after after *M. A. Ruderman, C. Kittel, T. Kasuya and K. Yosida*) and superexchange (see Fig 2.1). The superexchange occurs only in the insulating compounds and can be mediated via the hybridization of the $4f$ electrons with the electronic states of the neighboring nonmagnetic ligands.

The direct exchange can be described by Heisenberg model, where the exchange interaction energy can be described by hamiltonian:

$$\widehat{H}_{ex} = -\sum_{i \neq j} J_{ij} \mathbf{S}_i \mathbf{S}_j \tag{2.11}$$

where J_{ij} is the exchange integral between i-th and j-th spin. Its value might be either positive or negative which will favor either parallel or antiparallel alignment of spins. For direct exchange the corresponding wave function of neighboring atoms must overlap. The energy of direct exchange is typically of the order of 100 – 1000 K which implies quite high ordering temperatures of the compounds and occurs mainly for metals with partially filled $3d$ shell (for example Mn, Fe, Co, Ni).

In case of rare earths, there is practically no overlap between $4f$ orbitals, so there is no possibility to have magnetic ordering due to direct exchange interaction. One of the other possibilities how to obtain magnetic ordering is RKKY interaction [4]. In this theory the interaction between spins of different ions is mediated via conduction electrons and the each ion may obtain the information about orientation of the magnetic moments of surrounding ions. This interaction can be described by the hamiltonian:

$$\widehat{H}_{RKKY} = -\frac{1}{2} \sum_{i,j} J\left(\mathbf{R}_i - \mathbf{R}_j\right) \mathbf{J}_i \mathbf{J}_j \tag{2.12}$$

where the sum runs over all RE ions. $J\left(\mathbf{R}_i - \mathbf{R}_j\right)$ is the effective exchange parameter, which depends only on position of the two rare-earth ions and has an oscillatory character

due to formula $J(x) \sim (x\cos x - \sin x)/x^4$ (see Fig. 2.2). This interaction may lead to very complicated magnetic structures.

Different point of view of the indirect magnetic interaction in rare earths was proposed by I. A. Campbell [5]. According to his theory the strong, localized moment of $4f$ states can polarize the $5d$ states of RE. $5d$ states are more delocalized and overlap with each other. Than one can consider direct exchange between $5d$ states of neighboring atoms. Furthermore, in compounds with transition metals, the exchange between rare-earth $5d$ states and d states of the transition metal has to be considered.

According to calculations made by M. Diviš (see for example [6]) in the rare earth compounds it is common that both, RKKY interaction through conduction $6s$ states and the Campbell type of interaction through direct overlap of polarized $5d$ states coexist together in one compound.

2.3 Diamagnetism and paramegnetism

In this section we will deal with the response of the system with disordered magnetic moments to the magnetic field. This case can be described by the following field-dependent terms in the total hamiltonian (we have assumed magnetic field to be parallel to z direction) [1]:

$$\Delta\widehat{H} = \mu_B(\mathbf{L} + g_0\mathbf{S})\cdot\mathbf{H} + \frac{e^2}{8mc^2}H^2\sum_i\left(x_i^2 + y_i^2\right) \tag{2.13}$$

where μ_B is the Bohr magneton $\mu_B = e\hbar/2mc = 9.27410 \times 10^{-24}$ JT^{-1}; g_0 and is the electronic g-factor ($g_0 = 2.0023$). The energy shift of $\Delta\widehat{H}$ with respect to atomic excitations presented in previous sections is in magnetic fields up to approximately 10 T quite small so one can consider it only as an perturbation to the hamiltonian 2.5. Therefore one can calculate the changes of energies produced by $\Delta\widehat{H}$ using the second order perturbation theory:

$$\Delta E_n = \mu_B\mathbf{H}\cdot\langle n|\,\mathbf{L} + g_0\mathbf{S}\,|n\rangle + \sum_{n'\neq n}\frac{|\langle n|\,\mu_B\mathbf{H}\cdot(\mathbf{L} + g_0\mathbf{S})\,|n'\rangle|^2}{E_n - E_{n'}} \tag{2.14}$$

$$+\frac{e^2}{8mc^2}H^2\,\langle n\,|\sum_i\left(x_i^2 + y_i^2\right)|\,n\rangle$$

In case of the ion with all electronic shells filled only the last term in equation 2.14 has a nonzero value. The magnetic susceptibility of such an ion is:

$$\chi = -\frac{N}{V}\frac{\partial^2\Delta E}{\partial H^2} = -\frac{e^2}{6mc^2}\frac{N}{V}\,\langle 0\,|\sum_i\left(x_i^2 + y_i^2\right)|\,0\rangle \tag{2.15}$$

Equation 2.15 is known as the Larmour susceptibility. This susceptibility is negative, which means that the induced moments are opposite to applied magnetic field. The phenomenon,

in which the induced magnetic moments are opposite to the applied magnetic field is known as diamagnetism.

In the case of atom with the shell where the number of electrons is by one electron less than in half filled shell (J = 0 in the ground state; for example Eu) the ground state is nondegenerate and the linear term in 2.14 vanishes [1]:

$$\Delta E = \frac{e^2}{8mc^2} H^2 \langle 0| \sum_i \left(x_i^2 + y_i^2\right) |0\rangle - \sum_n \frac{|\langle 0| \mu_B \mathbf{H} \cdot (\mathbf{L} + g_0 \mathbf{S}) |n\rangle|^2}{E_n - E_0} \tag{2.16}$$

and hence the susceptibility is given by:

$$\chi = -\frac{N}{V} \left[\frac{e^2}{4mc^2} \langle 0| \sum_i \left(x_i^2 + y_i^2\right) |0\rangle - 2\mu_B^2 \sum_n \frac{|\langle 0| (\mathbf{L}_z + g_0 \mathbf{S}_z) |n\rangle|^2}{E_n - E_0} \right] \tag{2.17}$$

The first term in 2.17 is the Larmour susceptibility. The second term has opposite sign to Larmour susceptibility, so it favors alignment of spins parallel to the magnetic field - phenomenon known as paramagnetism. The second term in 2.17 describes the Van Vleck paramagnetism.

For computing the ground magnetic state of atom with $J \neq 0$ we can use the thermodynamics fundamental statistical, which ties together free energy (F) of the system with energies of the magnetic excitations ($E_n(H)$):

$$e^{-F/(k_B T)} = \sum_n e^{-E_n(H)/(k_B T)} \tag{2.18}$$

If only 2J + 1 states are thermally excited with appreciable probability (it means that there is no crystal field splitting and we neglect the higher excited states), then the free energy is given from equation 2.18 by:

$$e^{-\beta F} = \sum_{J_z=-J}^{J} e^{-\beta \gamma H J_z} \tag{2.19}$$

where $\gamma = g(JLS)\mu_B$ and $\beta = 1/(k_B T)$. The $g(JLS)$ is known as Landé $g-$factor and can be calculated according to:

$$g(JLS) = \frac{1}{2}(g_0 + 1) - \frac{1}{2}(g_0 - 1)\frac{L(L+1) - S(S+1)}{J(J+1)} \tag{2.20}$$

Using thermodynamic definition of magnetization:

$$M = -\frac{N}{V}\frac{\partial F}{\partial H} \tag{2.21}$$

we will obtain for magnetization [1]:

$$M = \frac{N}{V} \gamma J B_J(\beta \gamma J H) \tag{2.22}$$

where $B_J(x)$ is the *Brillouin function*, defined by:

$$B_J(x) = \frac{2J+1}{2J}\coth\frac{2J+1}{2J}x - \frac{1}{2J}\coth\frac{1}{2J}x \tag{2.23}$$

For small x we can approximate coth by its Taylor series up to $O(x^3)$ and then using the definition for susceptibility $\chi = \partial M/\partial H$ we can obtain the famous Curie's law:

$$\chi = \frac{N}{3V}\frac{\mu_B^2\mu_{eff}^2}{k_BT} \tag{2.24}$$

where μ_{eff} is effective moment of a free ion defined as:

$$\mu_{eff} = g(JLS)\sqrt{J\,(J+1)} \tag{2.25}$$

The Curie's law characterizes temperature dependence of paramagnetic systems with noninteracting permanent moments those alignment is favored by the magnetic field, and opposed by thermal disorder. It is important to note that this law is valid only for non-interacting magnetic moments under condition $k_BT \gg \gamma H$.

In compound, each spin feels the external field including the field from another spins, which can be described by the effective field hamiltonian $\widehat{H}_{eff}$:

$$\widehat{H}_{eff} = \mathbf{H} + \frac{1}{g\mu_B}\sum_{R'} J(\mathbf{R}-\mathbf{R}')\mathbf{S}(\mathbf{R}') \tag{2.26}$$

$\widehat{H}_{eff}$ is an operator with complicate dependency on a detailed configuration of all other spins. According to molecular field approximation we can replace $\widehat{H}_{eff}$ with its thermal equilibrium mean value and assume that each spin feels field $\mathbf{H}_{eff}$. This assumption we can accept only in the cases that each individual spin direction is quite close to its average value, or the exchange interaction is the long range interaction and many spins contribute to equation 2.26. If we replace each spin in 2.26 by its mean value, we will obtain [1]:

$$\mathbf{H}_{eff} = \mathbf{H} + \nu\mathbf{M} \tag{2.27}$$

where:

$$\nu = \frac{V}{N}\frac{J_0}{(g\mu_B)^2}, \qquad J_0 = \sum_R J(\mathbf{R})$$

Then in the mean field approximation the susceptibility is given by:

$$\chi = \frac{\partial M}{\partial H} = \frac{\partial M}{\partial H_{eff}}\frac{\partial H_{eff}}{\partial H} = \chi_0\left(1+\nu\frac{\partial M}{\partial H}\right) = \chi_0(1+\nu\chi) \tag{2.28}$$

where χ_0 is susceptibility evaluated in the field $\mathbf{H}$ and obeyed Curie's law. From this equation we can obtain the major correction to Curie's law. The resulting equation is known as Curie–Weiss law:

$$\chi = \frac{C}{T-\nu C} = \frac{C}{T-\Theta_p} \tag{2.29}$$

The Curie–Weiss law express the dominant correction to the hight–temperature Curie's law susceptibility, but close to magnetic order temperatures the measured susceptibility diverges as an inverse power of $T - T_c$ [1]:

$$\chi(T) \sim (T - \Theta_p)^{-\alpha} \tag{2.30}$$

α is typically between 1.3 and 1.4.

The last discussed contribution to the susceptibility is the contribution due to conduction electrons. This contribution occurs only in metals and can be described by equation [1]:

$$\chi = \mu_B^2 g(\varepsilon_F) \tag{2.31}$$

where $g(\varepsilon_F)$ is the density of levels at the Fermi level. The equation 2.31 is known as Pauli paramagnetic susceptibility. The Pauli paramagnetic susceptibility is pure effect of conduction electrons and is temperature independent. In most cases the Pauli paramagnetic susceptibility is much smaller than other types of susceptibilities and can be neglected.

2.4 De Gennes scaling

When one start from the indirect interactions presented in section 2.2 and assume the similar crystalline environment for different rare earths, one can show that the ordering temperature can be proportional to the de Gennes factor:

$$T_{ord} \sim (g(JLS) - 1)^2 J(J+1) \tag{2.32}$$

For schematic plot of equation 2.32 see also Fig. 2.3. This relation can be used for systematic study of isostructural compounds across series of intermetallic compounds when changing the rare-earth atom. The relation 2.32 is known as De Gennes scalling. The drawback of De Gennes scaling is that it doesn't take into account the changing of the exchange constant through the RE series and the crystal field effect, which may cause significant discrepancies between De Gennes scaling and measured ordering temperatures.

2.5 Metamagnetic phase transitions

The word "metamagnetic" was first used for the the transition from the antiferromagnetic state to the metastable field-induced ferromagnetic state of the compound. This transition is of the first order and exhibits an abrupt increase of magnetization of the compound. Later the word "metamagnetic transition" was broadened to every abrupt; discontinuous increase of magnetization induced by magnetic field. The examples compounds, which exhibit metamagnetic transitions are for example UGe_2 [7], $ErGa_2$ [8], URu_2Si_2 [9] and many other compounds.

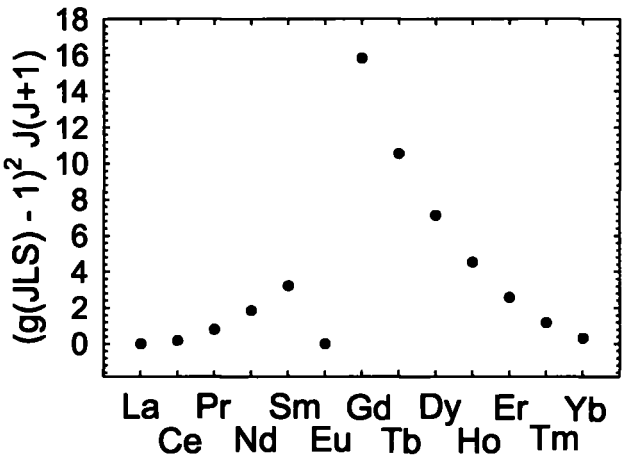

Figure 2.3: *The De Gennes scaling on the RE series.*

Basically, in the case of RE we can generally observe two different types of metamagnetic transitions: The so-called spin-flop metamagnetic transition which means that the collinear antiparallel moments rotate to direction perpendicular to the magnetic field. This type of metamagnetism occurs in compounds with small magnetocrystalline anisotropy (for example in Gd–based compounds). The second possibility is so-called spin-flip transition, which is single-step transition in which all moments suddenly jump to the direction of magnetic field. This type of transition occurs in compounds with strong magnetocrystalline anisotropy. However in most cases in RE compounds the situation is more complex as mentioned before (especially for compounds, which first order into noncollinear magnetic structure), so one can observe more than one metamagnetic transition with applied magnetic field.

Chapter 3

Experimental techniques.

3.1 Sample preparation

3.1.1 Polycrystalline samples

Polycrystalline samples are usually being prepared by melting together the constituting materials of stoichiometric amounts either under protective atmosphere or in vacuum to prevent oxidation. The radio-frequency or arc melting are most spread techniques used for heating above the melting point of the material. After heating the resulted compounds needs to be turned and remelted several times to achieve better homogeneity. The polycrystalline samples can be prepared easier than a single crystal samples, but in lot of cases the polycrystalline samples show only averaged physical properties, which in case of stronger anisotropy can lead to not very accurate conclusions.

Although, this thesis is focused on the measurement of the physical properties on the single-crystalline samples, we have also prepared some polycrystalline samples, namely both phases of $LaIr_2Si_2$, which we have used only for the specific heat measurements in the zero magnetic field and NdRhSn polycrystal for the neutron powder diffraction experiment. For this we have used mono-arc furnace on the Department of Condensed Matter Physics (DCMP).

3.1.2 Single-crystalline samples

A lot of intermetallic compounds with lower symmetry then cubic symmetry show different, sometimes very anisotropic physical behavior. That's why the single crystalline samples are more suitable than polycrystalline samples. On the other hands preparation of the single crystal is more difficult than polycrystal sample. The main difficulty in the preparation and crystal growth of rare-earth intermetallics arises from the complexities of the phase diagrams. There exist several methods, which can be used for the growing of the single crystals. Sometimes one method is more suitable than another method, so one has to

switch between the methods from time to time to obtain the desired single crystals. The methods, which we were used are:

- Czochralski method

  The Czochralski method was discovered by Jan Czochralski in 1917-18 and is the most spread method used for single crystal growing. Criterion for using this method is that the crystal should melt congruently, but the big advantage is very good control of grown material. The method is based on the propagating of one crystal grain, which has the most favorable conditions for growing and eliminating the other crystal grains. The crystal is pulled from the melt of stoichiometric composition of the constituting material placed on the hot or cold crucible. For the pulling the crystal a single crystal from the same material as pulled one, or if it is nod available, a tungsten or molybdenum rod is used as a seed. The seed is dipped into a melt and the temperature gradient between the seed and the melt causes forming the solid-liquid interface. Propagation of the one grain can be obtained by rotating the seed and simultaneously reducing the diameter of the of the grown ingot. This vexed area is named neck and the method calls "random necking procedure". After the neck there is high probability, that only single grain is propagated. The typical diameter of the neck is about 1 mm. Some of the parameters, which affect the resulting ingot are the thickness of neck, pulling rate, speed of rotation of seed and crucible, the input power (which affects the temperature of the melt) and volume of the melt.

  We have prepared practically all of the single-crystalline samples used in this thesis by this method. For the preparation we have used a tri-arc furnace installed in DCMP (*RE*RhSn series; see section 4.1.2 and $RE\mathrm{Ir_2Si_2}$ series; see section 4.2) and tetra-arc furnace installed in National Institute for Materials Science (NIMS) (*RE*PdSn series; see section 4.1.3). An example of one of the grown single crystals is shown in Fig. 3.1.

- Float zone technique

  In this method the molten zone holds between two vertical solid rods. The crystallization occurs moving the molten zone in one direction, which means, that one rod dissolves and another crystallizes. In case of using single crystal as one rod one can obtain by moving molten zone single crystal from polycrystal (feeding) rod. The molten zone is in no contact with crucible which means that one can avoid contamination of the material. The big disadvantage is that molten zone holds on rods only by surface tension, which restricts the area of possible melted material and dimensions of pulled crystals. Also the technique is suitable only for materials, which have higher surface tension in the liquid phase.

  We have prepared the $\mathrm{CeRh_2Ge_2}$ single crystal by this technique using the mirror furnace installed in NIMS. Actually, we have switched to this method after the several unsuccessful trials to grow $\mathrm{CeRh_2Ge_2}$ single crystal by the Czochralski method. This

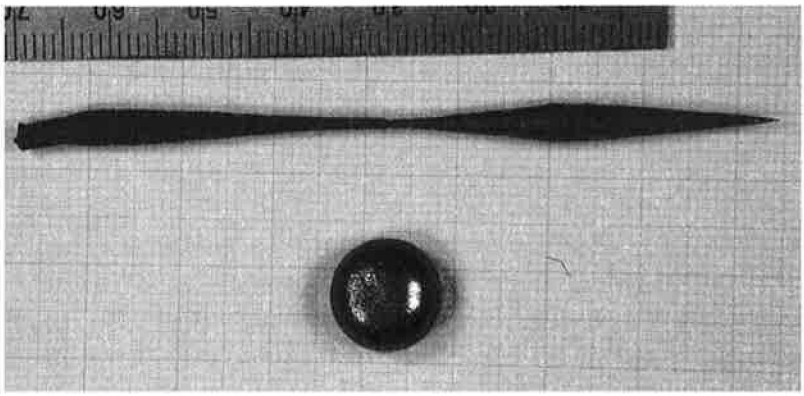

Figure 3.1: *Example of the grown single crystal (compound NdPdSn) by Czochralski method.*

single crystal was used by Dr. Kitazawa et al. for the single-crystal neutron diffraction experiment in Paul Scherrer Institut, Switzerland. We didn't include the results from this experiment into this thesis.

- Flux technique

  This method can be used for both congruent and noncongruent materials. The crystals grow from the super-saturated solution which is slowly cooled down (typical cooling rate is on the order of 1 K per hour). Crystallization occurs on spontaneously-formed nuclei of crystallization and grown crystals form well-developed facets, frequently same as in nature. Problem of the method is to find the proper solution from which the single crystals of desired compound can be grown. Another problem of the method is how to extract the grown crystal from the solution.

  After the unsuccessful trials to prepare the single crystals of PrPdIn and NdPdIn by the Czochralski method we have tried to prepare these single crystals from the indium flux. However, the product of our experiments were the single crystals of the pure praseodymium and neodymium, respectively. After this we have canceled the research on this two compounds.

To complete the list of the most-common methods for the preparation of the single crystals we should mention also the Bridgman method. As we didn't use this method, we refer the reader to the literature, for example [10].

3.2 Sample characterization and orientation

After the preparation of the sample one has to be sure, what sample he has prepared. For this serve some characterization methods. To characterize the samples used in this thesis we

have used the scanning electron microscope (SEM) (samples from the $RE\mathrm{Ir}_2\mathrm{Si}_2$ series) and the X-ray powder diffraction (presented samples) and Laue pattern (all single-crystalline samples).

3.2.1 SEM

The basic principle of scanning electron microscope (SEM) is to use the finely focused electron beam to scan the specimen and then detect outgoing signal from the specimen by proper detector. The beam current in the SEM is typically between 10^{-12} and 10^{-7} A with a beam energy in range of 200 eV to 50 keV. The beam penetration depth can then be in order of micrometer and the beam diameter is typically from 5 to 100 nm. For the characterization of the samples used in this thesis we have used SEM installed in the Department of Surface and Plasma Science and operated together with the Department of Condensed Matter physics, Charles University. From the whole events, which will occur when the electron beam hits the sample we have used:

- Secondary electrons (SE)

  This type of electrons leave specimen with energy typically lower than 10 eV, with 50 eV defined as an upper energy limit. From all of SE only these excited within approximately 10 nm from the surface can escape the specimen and can be detected. The example of the SE image can be found on Fig. 3.2a

- Backscattered electrons (BSE)

  This type of electrons leave specimen with an appreciable fraction of the primary energy, for purpose of definition with energy higher than 50 eV. The SE and BSE signals depend on the roughness of the sample surface and on the type of elements, which are present at the place, where electron beam hit the sample. So in chemical analysis SE and BSE signals can be used to visualize and allocate small precipitates in the sample and to study roughness and cracks in the specimen. The example of the BSE image can be found for example on Fig. 3.2b

- Characteristic X-rays

  When the electron beam hits the sample the majority of the energy dissipates thermally. But small fraction of the energy can be used for the ejection of the core-shell electron from the atom. The resulting vacancy is immediately filled by an outer-shell electron and the remaining energy difference is emitted by the characteristic X-ray radiation. If wee look only on the transitions of the most inner core-shells, the energy of these shells is not shifted due to the chemical bonds of the atom so this characteristic X-rays are atomic rather than molecular. The chemical composition can be investigated by assigning the position in the spectra to the tabulated positions of elements and the amount of the elements is proportional to the integrated area of the peak in the spectra. The element distribution can be obtained by scanning some

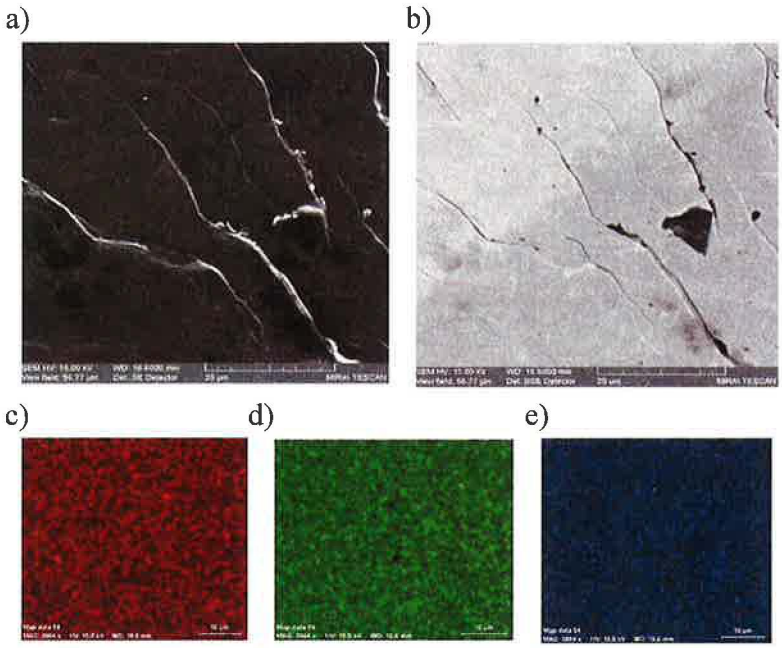

Figure 3.2: *Images from the surface of $PrIr_2Si_2$ compound: a) SE image - the contrast in the picture is produced mainly by roughness of the surface. b) BSE image - the contrast (except of cracks) in the picture is mainly produced by different composition of the sample c),d) and e) 2D scans of the characteristic X-rays, which visualize the distribution of Pr, Ir and Si distribution in the sample show the homogeneous distribution of the elements in the sample.*

area of the sample (line scan or 2D scan) and in each point measure the characteristic X-ray spectrum. The accuracy of quantitative determination of an element is 2 - 5 % and technique can determine elements with higher atomic number than boron. The example of the one of the EDX analysis we made is presented on Fig. 3.2c-e.

3.2.2 X-ray diffraction

X-ray diffraction occurs when X-rays scattered from a parallel planes of atoms constructively and destructively interfere with each other. The condition for the constructive interference is that the wavelength of X-ray (λ) is comparable with distance between parallel planes (d_{hkl}). The result of the interference are peaks in the positions well described by the Bragg's law:

$$\lambda = 2d_{hkl} \sin \Theta \tag{3.1}$$

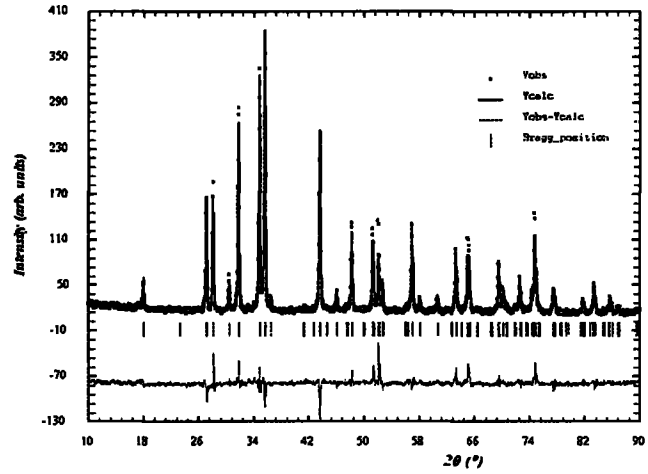

Figure 3.3: *The example of the obtained X-ray powder diffraction pattern (sample: $PrIr_2Si_2$; space group P4/nmm).*

Where Θ is the angle between incoming beam and normal to the (hkl) plane. Penetration depth of X-rays is normally smaller than 100 nm, so X-ray diffraction technique is quite surface technique.

Powder diffraction

For X-ray powder diffraction we have used the randomly oriented powder. In this case the Ewald construction consists of the circles in the reciprocal space, so we need only one scan to obtain reflections from all sets of planes with the different d_{hkl}. To obtain X-ray powder diffraction pattern we have used Cu K_α doublet (wavelengths 1.540598 Å and 1.544426 Å) and we have used the Bragg-Brentano geometrical configuration of the X-ray machine [11]. We have analyzed the obtained patterns using the Rietveld analysis [12] implemented in program *FullProf* [13] (for example see Fig. 3.3). Since *Fullprof* is only refinement program a previous knowledge of the structural model is necessary but for all presented compounds we were able to find structural models in the literature. The common structural models for the samples, we have prepared together with the crystallographic positions of the atoms are summarized in Appendix A and B. The quality of the agreement between calculated and observed pattern may be expressed using set of Rietveld $R-$factors defined for example in [12]. In all our case we have found good agreement between our refined pattern and our experimental data; the evaluated Bragg R-factor was typically in the interval 10 – 15 and RF-factor was typically between 12 and 17.

a) b)

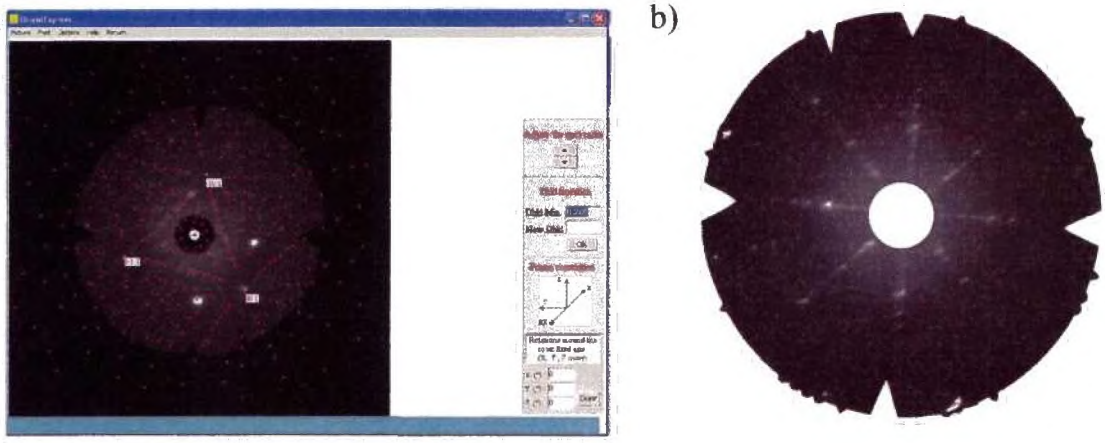

Figure 3.4: *a) the example of the simulated Laue pattern by the OrientExpress program. The experimental Laue photograph was done on the NdRhSn single crystal. b) The Laue photograph of already oriented single crystal of $PrIr_2Si_2$, where the c-axis is oriented along the incoming X-ray beam. That's why one can immediately notice the 4-fold symmetry of the diffraction spots.*

Laue method

Laue method is widely used and very efficient method for orienting single crystalline samples. In this method the white X-ray spectrum is used. The advantage of using the white X-ray spectrum is that according to the the Bragg law (equation 3.1) the Ewald construction will result to abscissas in the reciprocal space, so in any orientation of the crystal many of these abscissas intersect the Ewald sphere and we can observe the reflection. But the disadvantage of the method is that we do not know, which wavelength fulfilled the Bragg law for particular reflection. It means that we are not able to calculate the lattice parameters.

We have used Laue method for the checking, if the sample is single-crystalline and for the orientation of the single crystals of already known structure to the desired crystallographic orientation. X-ray technique is quite a surface technique, which is big disadvantage for checking if the sample is single-crystalline (we can see only the surface of the sample). That's why during the checking of the sample we have usually made several images from the different surfaces of the sample. To find out the proper orientation and to rotate to the proper orientation we have used the simulation program *OrientExpress* [14], by which we have simulate the Laue pattern, compared it with the obtained experimental pattern and found the probable indexation the diffraction spots (for example see Fig. 3.4).

3.3 Specific heat

3.3.1 Basic definitions

Thermodynamically, the specific heat of the substance is defined as an amount of heat (ΔQ)to increase the temperature of the substance (ΔT):

$$C_y = \lim_{\Delta T \to 0} = \frac{\Delta Q}{\Delta T} \tag{3.2}$$

where y indicates the control parameters kept constant. Although the definition is quite strong, to see deeper into the physics, which can be hidden in the specific heat we will mention also equivalent definition of specific heat in constant volume (C_v) based on the thermodynamics:

$$C_v = T \sum \left(\frac{\partial S}{\partial T}\right)_v = \left(\frac{\partial U}{\partial T}\right)_v \tag{3.3}$$

Where T is thermodynamic temperature, S is the entropy and U is a energy of the system.

The volume of all real compounds is temperature dependent, which causes difficulties in the measurements. In most cases it is more convenient to measure the specific heat under constant pressure (C_p) than C_v. Both specific heats are connected by the equation:

$$C_v - C_p = -\frac{9\alpha^2 V_m T}{\kappa} \tag{3.4}$$

Where α is coefficient of linear temperature expansion, V_m is molar volume and κ is coefficient of compressibility. In case of solid materials and temperatures sufficiently low the difference in the C_v and the C_p is small and can be neglected.

The total free energy of a system is the sum of the free energies of its components so the total specific heat is the sum of these contributions. The main contributions to specific heat in a solid in temperatures above 1 K are due to lattice vibrations (C_{ph}), conduction electrons (C_{el}) and magnetic contribution to specific heat (C_{mag}). In temperatures below 1 K also nuclear contribution can arise (can be recognized by $C \propto T^{-2}$ temperature dependence), but in this work we will not take into account this contribution.

3.3.2 Phonon part

The thermal vibrations of atoms are not only simply independent oscillations of the individual atoms. Atoms in compound are tied up together, so oscillation of one atom affects another atoms. The collective vibrations of the crystal (phonons) are analyzed as the traveling waves, like ordinary sound waves though of much shorter wavelengths. The theory of phonons consider, that in the matter are acoustic and optical branches of phonons. And both types can be more precisely divided into longitudinal and transversal ones. Longitudinal phonons means that atoms vibrate parallel to direction of wave and transversal

phonons vibrate perpendicular to the wave direction. In the optical branch atoms vibrate against each other, so mass center does not move. On the other hand, acoustic phonons move in the same direction, so mass center moves. There are two models, which are dealing with solving the phonon contribution to specific heat:

- Einstein model

  This model is based on three postulates:

  1. All atoms vibrate harmonically; independent from all neighbor atoms, but with the fixed freqency ω_E.
  2. The vibrations are isotropic. It means that all vibration modes are equivalent.
  3. The vibrations can be expressed as vibrations of harmonic oscillators.

  Then, solving a problem of n harmonic oscillators we can find the relation for the specific heat within the Einstein model [15]:

$$C_E = Nk_B \left(\frac{\Theta_E}{T}\right)^2 \frac{e^{\Theta_E/T}}{(e^{\Theta_E/T}-1)^2} \tag{3.5}$$

  where Θ_E is the Einstein temperature, which is connected with the frequency of the harmonic oscillators by the relation $\Theta_E = \hbar\omega_E/k_B$.

- Debye model

  Debye assumed in his theory that atoms can vibrate with more than one frequency, but the maximum allowed frequency is ω_D. Solving this problem will lead to the equation [15]:

$$C_D = 9Nk_B \left(\frac{1}{x_D}\right)^3 \int_0^{x_D} dx \frac{x^4 e^x}{(e^x-1)^2} \tag{3.6}$$

  Where $x_D = \Theta_D/T$ and $\Theta_D = \hbar\omega_D/k_B$ is the Debye temperature. In the reality, the Debye theory of specific heat describes the whole experimental curves much better than Einstein theory. The drawback of the Debye theory is, that integral in equation 3.6 can not be solved analytically. However, at the low temperatures integral in equation 3.6 can be approximated as $C_D \sim T^3$:

$$C_D = \beta T^3 \tag{3.7}$$

  where:

$$\beta = \frac{12}{5}\pi^4 N \frac{R}{\Theta_D^3} \tag{3.8}$$

  where R is a gas constant, N the number of atoms per formula unit and Θ_D is a Debye temperature.

Both theories described above predict that atoms oscillate as harmonic oscillators, which is fulfilled only at low temperatures, typically below 100 – 200 K. At higher temperatures anharmonicity of vibrating atoms may play an important role. The anharmonicity of the specific heat may be taken into account for example by multiplying the theoretical curve by factor $1/(1-\alpha T)$, where α is the correction for anharmonic oscillation and for the difference between C_p and C_v [16]. Also, another problem is, that in the matter there are acoustic and optical branches of phonons. It was found, that the Einstein model can be used for the describing of the optical branches and Debye model can be used for the describing of the accoustic branches of phonons.

3.3.3 Electronic part

Electronic contribution to the specific heat is linear dependent on temperature:

$$C_e = \gamma T \tag{3.9}$$

Coefficient γ has value from ones to tenths mJ/molK^2 for normal metals, however in heavy fermion systems γ have values up to thousands mJ/molK^2. Electronic contribution to specific heat usually dominates over the phonon part for temperature region $0.5K < T < 4K$.

3.3.4 Magnetic part

From the equation 3.3 we can see, that specific heat defines the order of the phase transition at the critical temperature ($T = T_{ord}$). In the case of a first-order phase transition the discontinuity in $S(T)$ is reflected in $C_p(T)$ as a divergence at T_{ord}. In a second-order phase transition a jump in $C_p(T)$ appears, because of the change of the dS/dT slope. The temperature dependence of $C_p(T)$ close to the transition provides useful information about the microscopic nature of the phase transition (e.g. dimensionality). When the magnetic part C_M can be extracted from the total specific heat, also the magnetic entropy of the system can be calculated:

$$S_M(T) = \int_0^T \frac{C_M}{T'} dT' \tag{3.10}$$

This equation gives an indication of the magnetic state of the rare-earth ion: the magnetic entropy S_M reaches the value of $R\ln 2$ for localized moments of spin origin (a spin 1/2 system). If the orbital components must be included, then $S_M = R\ln(2J+1)$ and for the ideal itinerant systems $S_M = 5/3\mathrm{Rln}\ 2$ [17].

However, there are huge problems to separate C_{mag} from another contributions to specific heat. One of the technique how to separate C_{mag} is to fit C_{el} and C_{ph} in the temperature range, where only negligible contribution of C_{mag} to specific heat is expected and then subtract the fitted curve from the measured curve. The different, very spread method is to measure the specific heat of a nonmagnetic analogue. After measuring the specific heat

of compound (C_{comp}) and measuring specific heat of nonmagnetic analogue (C_{anal}) we can just subtract this two specific heat from each other to obtain only C_{mag} of compound. In case, that the molar mass of the nonmagnetic analogue is quite different from the molar mass of measured compound, one should consider to make the correction of specific heat due to different molecular masses [18]:

$$C_{comp} = kC_{anal}$$

$$k = \left(\frac{\Theta_D(anal)}{\Theta_D(comp)}\right)^3 = \left(\frac{M_{comp}}{M_{anal}}\right)^{3/2} \tag{3.11}$$

where M_{comp} and M_{anal} are the molar masses and Θ_D are the Debye temperatures of the compounds.

Frequent magnetic anomaly, which is observed on the specific heat curves is the so-called Schottky anomaly. This anomaly is related to the thermal excitations in a level system split by Δ caused by removing $(2J+1)$-fold degeneracy of ground state multiplet by crystal field. This contribution to the specific heat in the paramagnetic region can be expressed as [19]:

$$C_{sch} = \frac{R}{T^2}\left[\frac{\sum_{i=0}^{n}\Delta_i^2 \exp\left(-\Delta_i/T\right)}{\sum_{i=0}^{n}\exp\left(-\Delta_i/T\right)} - \left(\frac{\sum_{i=0}^{n}\Delta_i \exp\left(-\Delta_i/T\right)}{\sum_{i=0}^{n}\exp\left(-\Delta_i/T\right)}\right)^2\right] \tag{3.12}$$

Schottky anomalies are well observed when their respective characteristic energies (or associated gaps Δ) are about $k_B\Delta < 100K$. The reason, why it is difficult to observe the Schottky anomalies with characteristic energies $k_B\Delta > 100K$ is that these anomalies occurs at higher temperatures and are broadened to the broad temperature range. This results to the situation $C_{ph} \gg C_{sch}$.

3.3.5 Experimental setup

In principle, there are two main groups of methods, which can be used for the specific heat measurements: nonadiabatic methods (for example AC calorimetric technique) [20] and the (Semi)adiabatic methods (heat pulse calorimeter) [21].

To measure the specific heat presented in this work we have used the semiadiabatic relaxation calorimeter with a weak heat link to the thermal bath realized through the thin wires. This calorimeter works in two steps: First it applies the thermal pulse to the sample. The consequence of this step is the increasing of the sample temperature. Typically we have set the apparatus to the increasing of the sample temperature approximately 2% of the temperature setpoint. This is in the most cases the reasonable compromise between the noise of the measured point and the temperature stability of the sample. The second step is the monitoring of the sample temperature, because the consequence of the weak heat link to the thermal bath is that the temperature of the sample will slowly decreases to the temperature of the bath. The total specific heat was then calculated using the fitting of the whole temperature response of the sample to the heat pulse according to the

calculations performed by Hwang et al. [21]. This calorimeter was implemented inside the PPMS(Quantum design) apparatus [22].

3.4 Electrical resistivity and magnetoresistivity

3.4.1 Electrical resistivity

The electrical resistivity ρ is defined as a proportionality constant in the phenomenological transport equation that relates the voltage applied on the sample U and the induced current I, known as Ohm's law (George Ohm, 1787-1854):

$$U = \rho I \tag{3.13}$$

The simplest approach for resistivity is Drude's theory (Paul Karl Ludvig Drude, 1863-1906), which considers electrons as gas of non-interacting particles, whose drift velocity due to field is compensating by collisions with impurities, lattice vibrations and electrons with each other. Within the relaxation time approximation we can obtain:

$$\frac{1}{\rho} = \sigma = \frac{ne^2\tau}{m} \tag{3.14}$$

where n is the number of current carriers, e is their charge m is their mass and τ is the characteristic relaxation time. The simple Drude's formula can not describe the electrical resistivity of solids sufficiently in many cases. As was shown by Matthiesen, the total resistivity in case of independent collision events in crystal can be expressed as the sum of resistivity contributions from particular collisions events:

$$\rho_{tot} = \sum_n \rho_n \tag{3.15}$$

In most of cases in resistivity we have to consider contributions from phonon-electron scattering (ρ_{ph-e}), electron-electron scattering (ρ_{e-e}), scattering on impurities and inhomogeneities of crystal lattice (ρ_0) and magnetic scattering (ρ_{mag}).

ρ_0 is temperature independent contribution to ρ_{tot}. As it is temperature independent, it can be obtained from low temperature data, where the most other contributions are negligible. The higher the quality of the crystal, the lower ρ_0. For metals we can define Residual Resistivity Ratio (RRR), which is defined as quotient of resistivity at room temperature and resistivity at the lowest-measured temperature. The good metal crystals have RRR much higher than 10.

Using Debye model to describe lattice dynamics, the simplest result for ρ_{ph-e} is given by Bloch-Grüneisen formula [23]:

$$\rho_{ph-e}(T) = 4R_{ph}\left(\frac{T}{\Theta_D}\right)^5 \int_0^{\Theta_D/T} dx \frac{x^5}{(e^x - 1)(1 - e^{-x})} \tag{3.16}$$

where R_{ph} is temperature independent parameter, which contains constants for electron-electron coupling and atom masses and Θ_D is the Debye temperature. In approximation of low temperatures (T $\ll$ than Θ_D) the equation 3.16 can be approximated by $\rho_{ph-e} \approx T^5$ and in high temperatures ($T \geq \Theta_D$) the $\rho_{ph-e} \approx T$

The electron-electron scattering for the Fermi liquid compounds can be described by T^2 dependence [24]:

$$\rho_{e-e}(T) = c\left(\frac{k_B T}{E_F}\right)^2 \tag{3.17}$$

with c being a microscopic scattering cross section and E_F being the Fermi energy.

If the crystal is made up from magnetic ions, any disorder in the arrangement of the magnetic moments will give rise to magnetic scattering. In case of paramagnetic state there is contribution from the randomly oriented magnetic moments to the resistivity which can be described by equation:

$$\rho_{spd} = \frac{3\pi N m^*}{2\hbar e^2 E_F} |\mathcal{J}|^2 (g-1)^2 J(J+1) \tag{3.18}$$

where m^* is effective mass of conduction electrons. The ρ_{spd} is temperature independent. In some intermetallic compounds an increase of resistivity was observed at transition temperature [25]. This increase is associated by the changing the periodicity of the compound due to periodicity of the magnetic unit cell. This new periodicity results in additional zone boundaries (superzones), and consequently produces further energy gaps at the Fermi surface. In the ordered state the magnetic scattering can be described for example due to Andersen's model using electron-magnon interraction [26]:

$$\rho_{mag} = ET\left(1 + \frac{2T}{\Delta}\right)\exp\left(\frac{-\Delta}{T}\right) \tag{3.19}$$

where E is temperature independent parameter, which depends only on electron-magnon coupling and Δ represents gap in the dispersion relation of ferromagnetic magnons.

3.4.2 Magnetoresistivity and Hall effect

In case of applying together electric and magnetic field on the sample, the Ohm's law (Equation 3.13) has to be written as tensor equation which can not be reduced to a scalar relation in all lattice symmetries except for the cubic one. The most convenient way how to describe the resistivity under the applied magnetic field is then via the longitudinal($\vec{B} \parallel \vec{E}$) magnetoresistivity, transverse ($\vec{B} \perp \vec{E}$) magnetoresistivity and the Hall resistance ρ_H. The $\rho_\perp$ has its origin in the curving the electron's free path by the Lorent'z force:

$$\vec{F_L} = -e(\vec{E} + \vec{v} \times \vec{B}) \tag{3.20}$$

This effect gives always rise to the $\rho_\perp$. Also Hall resistance is the direct consequence of the Lorentz force: in fact it is an effect of cumulation of the electric charge on the side of

the sample (E_y). Then the R_H can be calculated from the equation:

$$\vec{E}_y = R_H \vec{B} \times \vec{j} \tag{3.21}$$

where $\vec{j}$ is the current density, or in the case of electric current (let's say along x axis) perpendicular to magnetic field (let's say along z axis) we can calculate the normal Hall constant from the measured voltage along the y axis (V_y):

$$R_H = \frac{V_y d}{IB} \tag{3.22}$$

where d is the thickness of the sample. The sign of the R_H is depend on the charge ($+e$ or $-e$) of the electric current carriers.

At low temperatures the spin direction of charge carriers is conserved during most scattering events. This is because spin waves (magnons), which mix spin-up and spin-down states, are not strongly excited. In case of having localized moments on atoms, which are somehow ordered, one should take into account the spin-spin scattering, which contributes to the total resistivity. As the ordered magnetic moments may depend on external magnetic field, one should observe decrease as well as increase of magnetoresistivity with depend only on spin arrangement inside the sample and the response of spin arrangement to the magnetic field. Also in case of Hall effect one have to take into account anomalous contribution (R_S) to the Hall effect:

$$\rho_H = R_H B + R_S M \tag{3.23}$$

where M is the magnetization of the sample. The detailed description of the magnetoresistivity and the anomalous Hall effect can be found for example in [27, 28]

3.4.3 Experimental setup

For the electric transport measurements we have used standard four–probe AC method. This method is very powerful in eliminating the unwanted parasitic contributions to the whole measured signal. The principle of the method can be found elsewhere [29]. In all cases we have used silver paint to glue the copper or gold wires on the sample.

We have measured resistivity using the PPMS (Quantum design) measurement system [22] in constant current mode. We have applied AC current with the typical amplitude around 10 mA and frequency 71 Hz (to avoid the interference with the public electrical network). Also to avoid the overheating the sample we have restricted the electric pulse duration for the measurement to 0.5 second. In the case of measurements in temperatures below 2 K we have restricted the AC current amplitude to 1 mA or less and pulse duration to 0.1 s to avoid overheating of the sample.

3.5 Magnetic measurements

3.5.1 Magnetic phase transitions

Using the Landau theory of phase transition we can define some ordering parameter and subsequently expand the free energy function in a power series of this order parameter. In the case of magnetic phase transition we can take a spontaneous magnetization ($\vec{M}$) as a free parameter (in case of transition from paramagnetic to magnetically ordered state) and write the free energy function in form:

$$F(\vec{M},T,\vec{B}) = f_0(T) + a(T-T_c)\vec{M}\cdot\vec{M} + b\vec{M}\cdot\vec{M}^2 - \vec{M}\cdot\vec{B} \tag{3.24}$$

As the order of the transition is defined by the lowest discontinuous derivative of the free energy (F) function, the first-order magnetic phase transition shows singularities in $\partial F/\partial M$.There is also always some hysteresis effect connected with this kind of magnetic phase transition. The second order magnetic phase transition shows discontinuity only in the $\partial^2 F/\partial M^2$. Thus magnetization and susceptibility ($\chi = \partial M/\partial H$) measurements represent the important tool in the study of magnetic phase transitions.

3.5.2 Correction to demagnetizing factor

When we insert a sample into a magnetic field, the intensity of magnetic field around the sample and inside the sample will change. Generally the internal magnetic field H_i, which "feels" the sample will be smaller than external field H_e by demagnetizing field H_d:

$$H_i = H_e - H_d \tag{3.25}$$

The demagnetizing field is proportional to the magnetization of the sample:

$$H_d = DM \tag{3.26}$$

where D is the demagnetizing factor along the measured direction. The demagnetizing factor is homogeneous only in case of revolting ellipsoid. Let's define rotational axis to be a, the axis perpendicular to a let's define as b and define parameter $p = a/b$. If we suppose that $p > 1$ then we can get for demagnetizing factor along $a-$axis [29]:

$$D_a = \frac{1}{p^2-1}\left\{\frac{p}{\sqrt{p^2-1}}\ln\left(p+\sqrt{p^2-1}\right) - 1\right\} \tag{3.27}$$

The sum of the demagnetizing factors along all principal axes must be equal to 1, which implifes in our case:

$$D_b = \frac{1-D_a}{2} \tag{3.28}$$

In real measurement it is very difficult to have samples of the shape of rotational ellipsoids. But equations 3.27 and 3.28 can still be used as a first approximation to estimate

the demagnetization factor. The equations also tell that the most suitable samples for magnetization measurements are long-needle-shaped samples, because they have smallest demagnetization factor.

3.5.3 Correction to ferromagnetic impurity

Even when using as pure starting materials as possible and preparing the sample in very clean environment one still will have some amount of the impurities in the sample. These impurities may cause the serious problems for example in the case that the impurities are ferromagnetic and the measured compound is paramagnetic or diamagnetic. To avoid the problem of the ferromagnetic impurities one can assume, that in the high magnetic fields the ferromagnetic impurity is already saturated, so $dM_{imp}/dB \sim 0$. On the other hand $dM_{sample}/dB \neq 0$. Than taking into account the definition of the magnetic susceptibility:

$$\chi = \frac{dM}{dB} = \frac{d(M_{imp} + M_{sample})}{dB} = \frac{dM_{imp}}{dB} + \frac{dM_{sample})}{dB} \tag{3.29}$$

we can aproximate:

$$\chi_{sample} = \frac{M_1 - M_2}{B_1 - B_2} \tag{3.30}$$

Where M_1 is magnetization measured at field B_1; M_2 is magnetization measured at field B_2 and we assume that at field B_1 and B_2 the ferromagnetic impurity is already saturated.

3.5.4 Experimental setup

The magnetization measurements can be done using two different groups of methods: the force methods (faraday balance, torque magnetometer) and the induction methods.

All bulk magnetic measurements reported in this thesis were performed using the induction methods. These methods are based on the Faraday's law of electromagnetic induction:

$$U \sim \frac{dB}{dt} \tag{3.31}$$

where U is induced voltage in the coil. In case of pulling the sample out of coil, the change of the magnetic field inside the coil will be proportional to the magnetization of the sample, which was pulled out from the coil. Hence:

$$M \sim \int U dt \tag{3.32}$$

All bulk magnetic measurements up to 14 T reported in this thesis were performed using the induction methods. The results were measured on the extraction magnetometer implemented into PPMS (Quantum Design) system [22] and using SQUID magnetometer MPMS, also from Quantum Design [30]. To perform this experiments we have used bar-shaped samples, or cubic samples to avoid the large demagnetizing field in the samples

(see section 3.5.2). Some of the $M(B)$ curves (especially the $M(B)$ curves for the NdRhSn under applied hydrostatic pressure) were also corrected due to the demagnetizing factor. Also the measured $\chi(T)$ curves were calculated from the $M(T)$ curves measured in the two different magnetic fields to filter the possible ferromagnetic impurity in the samples (see section 3.5.3). This correction was very important especially while measuring the nonmagnetic La-based analogues and CeRhSn and $CeIr_2Si_2$.

The high field experiment on NdPdSn was done using 30 T hybrid magnet combined with the extraction magnetometer installed in the Tsukuba magnet laboratory, National Institute for Materials Science, Tsukuba, Japan. The detailed description of the magnet and the sample environment can be found in [31]. The high field experiment on $PrIr_2Si_2$ was done on the 50 T pulsed magnet in the Laboratory for pulsed magnetic fields, Leibnitz Institute for Solid State and Materials Research, Dresden, Germany. The detailed description of the magnet and the sample environment can be found in [32].

3.6 Pressure cells

Many of the physical properties of the compounds somehow change with pressure. For example observed quantum critical point at high pressures (for example [33]) or in magnetism shifting the ordering temperature due to applied pressure (for example [34]), but also changing the electron energy spectrum and carrier concentration and many other properties of semiconductors, metals and superconductors properties. These properties can be observed by magnetic (magnetization, susceptibility), transport (resistivity, Hall), optical (luminiscence, photoconductivity) and diffraction (X-ray, neutron diffraction) techniques. So one have to construct a pressure cells to achieve the different pressure range and to be useful for different experimental methods [35].

The hydrostatic pressure experiments included in this thesis were done using the copper beryllium (CuBe) piston cells with the maximum working pressure of around 1.2 GPa. This is much lower than the highest reached pressure limit for the piston cell (5 GPa) [35], but our piston cells had to fit into the MPMS apparatus, so the diameter of the cells has to be smaller than 9 mm [30]. We have used two different pressure cells. In Prague we have used the CuBe piston cell produced by Academy of Science in Czech Republic filled with mineral oils as a pressure medium. As a sealing we have used Bridgman mushroom-type seal with indium, tin and copper rings and plug with rubber and copper rings as sealing. The pressure inside the cell was measured using Pb as an internal pressure sensor. The disadvantage of this cell is that the signal of Pb pressure sensor is superimposed on the signal of the sample, which may cause difficulties especially close to the superconducting phase transition of Pb[1]. The scatch of the cell can be found on Fig. 3.5. The second pressure cell was the one which we have used in NIMS. In this case we have again used the

[1] In our experiments this happened while investigating the pressure effects connected with T_C of NdRhSn; see section 4.1.2

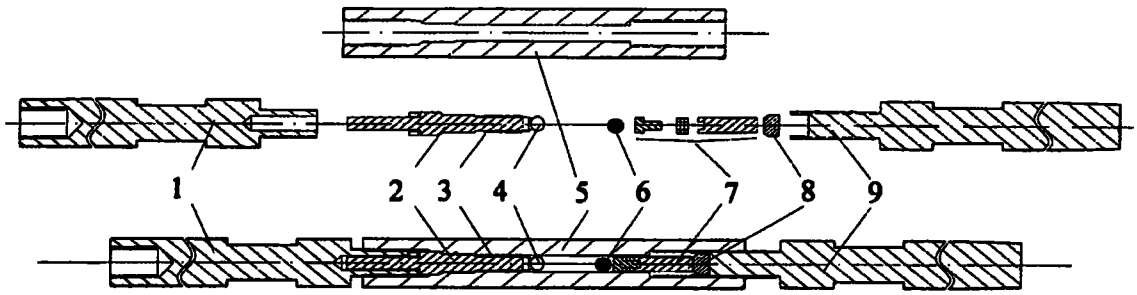

Figure 3.5: *The sketch of CuBe pressure cell used in our experiment. 1-plug supporting bolt; 2-plug with washer; 3-sealing of the plug; 4-sample on the holder; 5-pressure cell; 6-Pb pressure sensor; 7-piston with Bridgman mushroom; 8-piston backup; 9-piston supporting bolt. The figure was taken from [36].*

CuBe pressure cell, but the sample was sealed inside the teflon container which contained the Fluorinert mineral oil. This container was inserted into the pressure cell and again sealed from both sides by a copper rings. In this case the pressure was determined from the force, which we had to use for pressing the piston during the pressurizing of the cell at the room temperature. Problem in this cell arises during the clamping of the cell, because one can not check the pressure inside the clamped cell.

3.7 Neutron diffraction

Bragg law (3.1) has general validity for both X-ray diffraction and neutron diffraction. However, there are some differences between X-ray and neutron interaction with matter which makes neutron diffraction complementary technique to X-ray diffraction: neutrons are electrically neutral and can penetrate deeply into matter, which makes neutron diffraction really bulk method. Also neutrons scatter on the atomic nuclei and also on the electron cloud of the atom in contrary to X-rays, which scatter only on the electron cloud of the atom. The third difference is, that scattering cross section of neutrons on the nucleus does not depend on the atomic mass number, while X-rays scattering cross section is proportional to the atomic mass number. The consequence is that the neutrons can detect light elements and different isotopes of one element much easier than X-rays. The last very important difference is, that neutron has a spin $n_s = 1/2$, so neutron can detect also magnetic moments in the matter. In case of X-rays one needs the polarized X-rays with two different types of polarization (for example Magnetic Circular Dichroism technique) and huge intensity of the beam (synchrotron) to detect the magnetic moments. More information about the neutron and X-ray diffraction techniques can be found for example in [37]. In our experiments we have used the last mentioned feature of the neutron diffraction.

We have performed both, powder diffraction and single crystal diffraction experiment.

The only neutron experiments, which are mentioned in this thesis were done on the NdRhSn samples. In this case the absorption of the thermal neutrons by this compound was not supposed to be high[2], so we used no extra precautions to reduce the absorption of the neutrons.

The powder diffraction experiment was done on D1B diffractometer in ILL, using about 7 grams of the powdered sample. The detailed information about D1B diffractometer can be found in [39]. As the monochromator we have used the Pyrolytic graphite which provided us the monochromatic neutron beam with wavelength of 0.252 nm. As a detector we have used the 400-channel multidetector with resolution of 0.2°. We have collected patterns from 2 K to 14 K. After this we have subtracted the 14 K data from data measured at lower temperature to obtain magnetic contribution to diffraction pattern. In the studied temperature range we have neglected the lattice contraction due to temperature change. We have fit the obtained magnetic diffraction pattern using *FullProf* software [13]. The neutron form factors are directly implemented into this software and can be found for example in [40].

The single crystal experiment was done on VIVALDI diffractometer in ILL [41], using a cylindrical sample with the volume of about 40 mm^3. VIVALDI is the instrument, which use the white neutron beam and which is equipped with a large 2D detector. The advantage of such a configuration is high neutron flux, which results to small acquisition time for the desired precision. Also 2D detector combined with the white beam allow to observe many reflections at the same time. The method is from this point of view similar to the X-ray Laue diffraction (see section 3.2.2). The drawback of the technique is the data evaluation because of using the white beam. There is no way how to identify the wavelength for the specific spot so the Braggs law cannot be used. Consequently, it is impossible to determine the absolute values of the lattice parameters, only their ratio may be found. The same holds for the diffraction spots of the magnetic origin.

[2]The element with the highest absorption in our material was rhodium, which has absorption 150 Barns for the thermal neutron. Just for comparison, absorption of gadolinium is 49 000 Barns [38]

Chapter 4

Results

4.1 RETX compounds

4.1.1 Introduction

Crystal structures

The $RETX$ compounds (RE = La – Yb; T = d-metal and X = p-metal) crystallize in a variety of crystal structure types (cubic, tetragonal, hexagonal, orthorhombic, monoclinic), depending mainly upon the nature of T and X elements [42]. It means, that changing only RE element and leaving T and X element the crystal structure usually remain unchanged. In this type of compounds the magnetism is connected with RE atom, so changing the RE atom in $RETX$ compound the magnetic behavior may change dramatically.

The example for cubic $RETX$ compounds (MgAgAs crystal structure) can be RETBi compounds for T = Pd, Pt, Ni or heavy REPtSb compounds [43, 44]. As this structure is the most symmetric one, one should not suppose large magnetocrystalline anisotropy in these systems. Some of the $RETX$ compounds with germanium (RERuGe and RECoGe) and with silicon (REFeSi; RERuSi; RECoSi) crystallize in the tetragonal CeFeSi crystal structure [45]-[48]. The hexagonal ZrBeSi-type crystal structure is reported for RENiSb; [49]. Another hexagonal LiGaGe-type structure (in old articles reffered as $CaIn_2$-type structure, see appendix A.1) is reported for REPdSb and light REPtSb compounds [44, 50]. The third possibility of hexagonal $RETX$ compounds are those which crystallize in the ZrNiAl-type crystal structure. Light RERhSn and RETIn (T = Rh, Ni, Pt and Pd) compounds are representatives of this group of compounds [51]-[56]. The representatives for the orthorhombic TiNiSi-type structure are REPdX (X = Sn and Ge); RENiX (X = Sn, In) and RERhX (X = Sb, Bi, Ge) [43, 57]-[61]. Some of the $RETX$ compounds also crystallize in the monoclinic CeCoAl-type structure [62]. The detailed crystallographic information for all mentioned crystal structures is summarized in appendix A.1 and A.2.

This work is focused to $RETX$ compounds which crystallize in the hexagonal ZrNiAl-type structure (space group $P\bar{6}2m$) and TiNiSi-type crystal structure (space group $Pnma$).

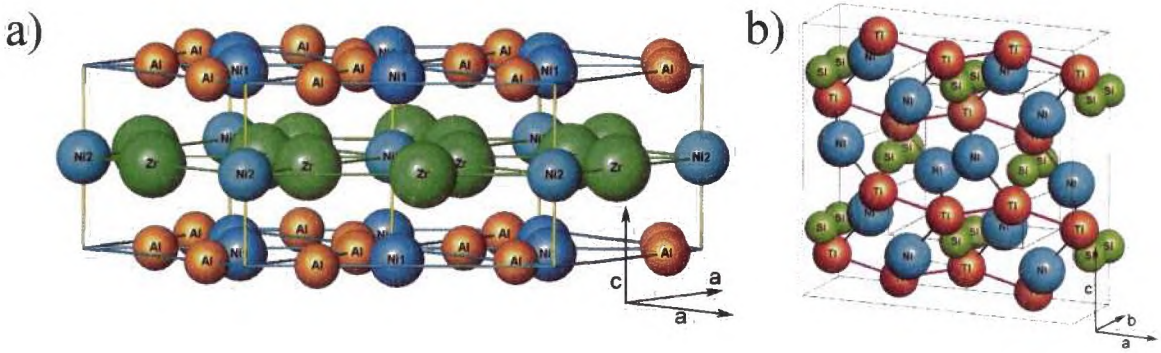

Figure 4.1: *The sketch of the structure of RETX compounds, which we were deal with: a) hexagonal ZrNiAl structure; b) orthorhombic TiNiSi structure.*

The sketch of both structures can be found on figure 4.1.

ZrNiAl structure is strictly layered structure with alternating of two types of layers (first layer: RE + 1/3 of T atoms; second layer: X + 2/3 of T atoms) along the c-axis. In this structure the shortest $RE - RE$ distance is usually within the basal plane, but it again depends on T ans X metal. The point symmetry at the position of the RE atom is orthorhombic which results to 9 crystal field parameters B_l^m. The consequence of the layers in the structure is that the single crystals of the ZrNiAl structure can be easily cleaved perpendicular to the c-axis. The lattice constants for the ZrNiAl-type compounds, which we have studied are summarized in table 4.1.

In the TiNiSi crystal structure RE atoms form zigzag chains running along the a-axis which are interconnected to adjacent chains and form a three-dimensional network. In this structure the point symmetry at the position of the RE atom is again orthorhombic which again results to 9 crystal field parameters B_l^m. The lattice constants for the TiNiSi-type compounds, which we have studied are summarized in table 4.2.

General physical properties

Typical for the LaTX compounds is the metallic behavior at higher temperatures and superconducting phase transition at temperatures around 2 K and lower [63]-[66]. Some of the these compounds can be also the Pauli paramagnets [67].

Many of the CeTX compounds are referred to exhibit Kondo behavior (CeNiIn [56]; CeNiSn [68], CePdSn [69]). CePdSb and CePtSb orders ferromagnetically at T_c = 17 K and 4.7 K, respectively [70, 71] while CePdIn is an antiferromagnetic heavy fermion compound with $\mathbf{k}$ = (1/4 0 0), which orders at T_N = 1.7 K [56, 72]. Another antiferromagnetic compound (T_N = 7 K) is CePdSn [69]. A weak Kondo effect is also observed in this compound [69]. CePtSi and CeRuSi are referred to be the heavy fermion compounds [73]. CeRhIn is the valence fluctuator [74]. Some of the CeTX compounds also exhibit

Compound	a (nm)	c (nm)	x_{RE}	x_X	ref.
LaRhSn	0.7479(3)	0.4217(1)	0.591(1)	0.243(3)	our work
	0.7478	0.4223			[51]
CeRhSn	0.7446(3)	0.4081(2)	0.592(1)	0.247(1)	our work
	0.74491(2)	0.40814(1)	0.5868(5)	0.2490(3)	[52]
PrRhSn	0.7415(1)	0.4151(2)	0.586(2)	0.249(2)	our work
	0.7539	0.392	0.605	0.265	[53]
NdRhSn	0.7399(2)	0.4128(1)	0.586(2)	0.249(2)	our work
	0.7413(1)	0.41290(2)	0.58638(5)	0.24901(5)	[54]

Table 4.1: The crystallographic parameters of the ZrNiAl–type RETX compounds obtained from the X-ray powder diffraction experiments - comparison of parameters determined by us and parameters found in literature.

Compound	a (nm)	b (nm)	c (nm)	ref.
LaPdSn	0.7642(2)	0.4728(1)	0.8047(2)	our work
	0.7631	0.4732	0.7986	[51]
PrPdSn	0.7468(3)	0.4681(3)	0.7958(3)	our work
	0.7525(3)	0.4669(2)	0.7972(4)	[50]
NdPdSn	0.7419(1)	0.4665(2)	0.7949(1)	our work
	0.7476(3)	0.4666(2)	0.7946(3)	[50]
NdRhSb	0.7329(3)	0.4584(2)	0.7839(3)	our work
	0.7307(2)	0.4593(1)	0.7860(2)	[43]

Table 4.2: The crystallographic parameters of TiNiSi–type RETX compounds - comparison of parameters determined by us and parameters found in literature. The free crystallographic parameters for position 4c are close to these attached in appendix A.2.

an opening the gap at the Fermi level and subsequently semiconducting behavior at low temperatures (CeRhSb [75], CeRhAs [76])

A lot of PrTX compounds are referred to be paramagnetic down to the lowest-reachable temperature (PrCoGe [46], PrCoSi [47], PrFeSi [48], PrIrGe [60], PrNiSb [77], PrNiSn [78], PrPdGe [79]). This is caused in the cases when the crystal field has a low point symmetry at the position of Pr^{3+} ion and subsequently splits the $^3H_4$ ground state multiplet of Pr^{3+} ion into 9 singlets (ZrNiAl and TiNiSi-type structures are good examples for such a case). In case that this splitting is large enough, the first excited level is too far to hybridize with the ground state level. This results to the singlet ground state so there will be no magnetic ordering. Another group of PrTX compounds consist of compounds, which order ferromagnetically at low temperatures (PrIrAl T_C = 9 K [80]; PrRhAl T_C = 4.7 K [66] PrRhIn T_C = 5.8(6) K [81]) or antiferromagnetically (PrRuGe T_N = 62 K [45]; PrRuSi T_N

= 74 K [45], PrNiAl T_N = 6.5 K (k = (1/2 0 0.41)) [82], PrCuAl T_N = 7.9 K [83]). PrPdAl undergoes two antiferromagnetic phase transition at $T_{N,1}$ = 4.2 K and $T_{N,2} \sim$ 1.5 K [84].

Most of NdTX compounds order magnetically at low temperatures. From these, which order antiferromagnetically we can mention NdCoGe with Neel temperature T_N = 8 K (k = (0 0 1/2)) [46], NdCoSi with T_N = 7 K [46], NdNiAl T_N = 2.4 K (k = (1/2 0 0.46)) [82], NdNiSn with T_N = 2.8 K [85], NdPdGe with T_N = 4 K (k = (0 0 0.01)) [86], NdPtGe with T_N = 6(1) K [87], NdPtSi with T_N = 3.8 K [88], NdRhGe with T_N = 14 K (k = (1/2 0 1/2)) [89] and also NdRuGe which orders at extremely nigh temperature T_N = 65 K [45]. Another part of NdTX compounds orders ferromagnetically: NdFeSi with T_C = 25 K [45], NdIrAl with T_C = 13 K [80], NdNiSb with T_C = 23 K and NdRhAl with T_C = 10.5 K [66]. NdPdAl undergoes two antiferromagnetic phase transitions at $T_{N,1}$ = 5 K and $T_{N,2}$ = 4 K. Magnetic propagation vector above $T_{N,2}$ in this compound shows pronounced temperature dependence while below $T_{N,2}$ propagation vector locks to k = (1/4 0 0.444) [84]. NdPdSb exhibits antiferromagnetic phase transition at 10 K with magnetic propagation vector k = (1/7 0 0) and antiferromagnetic - ferromagnetic phase transition at 4.2 K [90]. One of the interesting compounds of NdTX series is also NdPtBi which exhibit semiconducting or semimetallic behavior of resistivity and antiferromagnetic phase transition at T_N = 2.2 K [91].

This work is focused on hexagonal LaRhSn, CeRhSn, PrRhSn and NdRhSn compounds and on orthorhombic LaPdSn, PrPdSn, NdPdSn and NdRhSb compounds. We first summarize the known behavior of these compounds in the next paragraphs. Then we present our results in sections 4.1.2 and 4.1.3.

State of art of materials, we have studied.

Electrical resistivity and ac susceptibility measurements on polycrystalline LaRhSn sample were performed by F. Canepa and S. Cirafici [51]. These measurements revealed superconducting phase transition with the critical temperature 1.7 K [51]. After this Ho et al. also studied the superconductivity on LaRhSn polycrystalline samples and reported T_c = 2 K and the critical field for destroying the superconductivity rising from 0.1 T at 1.6 K to 0.7 T at 0.2K [92]. All these previously published results were done on polycrystalline samples. The only previously grown LaRhSn single crystal was studied only as an non-magnetic analogue within the investigation of CeRhSn compound [93], but it is worth to note that the magnetic susceptibility of LaRhSn in the normal state is remarkably higher than the susceptibility of CeRhSn [94].

Thermodynamic, transport and magnetic properties of CeRhSn were reported by several authors on both polycrystalline and single-crystalline samples [52, 53, 93, 95]. Similarly to other heavy fermion compounds the critical behaviour depends strongly on the real stoichiometry, impurity content and atomic disorder induced by different heat treatment. The specific heat measured on the single crystal exhibits the local minimum in C/T vs. T dependence at 7 K. At the lower temperatures than 7 K the upturn in specific heat data suggests non-Fermi liquid behaviour [93]. The electronic contribution to specific heat determined

from the low–temperature part of the data varies from 61 mJ $mol^{-1}K-2$ [93] to about 160 mJ mol^{-1} K^{-2} [52] depending on the quality of the sample. The resistivity of the compound is highly anisotropic. The *c*-axis resistivity exhibits metallic–like behaviour while the *a*-axis resistivity shows maximum at 70 K [93]. The longitudinal and the transversal magnetoresistivity in CeRhSn is positive up to 18 T [93]. Below 1 K the magnetic susceptibility measured along the *a*-axis is about 10 times smaller than the susceptibility measured along the *c*-axis [93] which suggest that *c*-axis is an easy axis of the magnetization.

Polycrystalline PrRhSn sample was firstly studied from magnetic point of view by Routsi et al. [53]. They have reported the absence of magnetic ordering above 4.2 K. The susceptibility measured on polycrystalline samples obeys the Curie-Weiss law for temperatures higher than 40 K with parameters Θ_p = 10 K and μ_{eff} = 3.83 μ_B [53]. Łątka et al. [96] claimed, that the compound orders ferromagnetically at T_C = 3.0 K and exhibits a hysteresis loop with a small coercive field of 2 mT. The magnetization curve measured on a polycrystal does not saturate in fields up to 5 T, which was attributed to possible high magnetic anisotropy [96] in the compound.

As concerns the magnetism of NdRhSn, only scarce information obtained from measurements on polycrystalline samples has been published by Routsi et al. [53] and two slightly contradicting works of Łątka et al. [54, 97]. Routsi et al. [53] claims that at temperatures above 40 K, the magnetic susceptibility obeys the CurieWeiss law with the values of the effective moment μ_{eff} = 3.55 μ_B/f.u. and the paramagnetic Curie temperature Θ_p = 12 K. The saturation of the low-temperature (4.6 K) magnetization (yielding the value of 1.82 μ_B/f.u. in 2 T) was interpreted in terms of a ferromagnetic state, but no information on ordering temperature was given [53]. Łątka et al. report ferromagnetism with T_c = 10.3 K and superconductivity with Tc = 6.9 K [97] and later corrects his report to only one, ferromagnetic phase transition at T_c = 10.3 K [54]. But if NdRhSn undergoes only one phase transition at 10.3 K the observed anomaly on the electrical resistivity at around 7 K [97] remains unexplained.

The LaPdSn was found to have normal metallic behavior down to 2 K [51], obeying Bloch-Grüneissen law at temperatures above 2 K. The characteristic temperature from the Bloch-Grüneissen law was found to be Θ = 270 K [51]. Recently, the low-temperature experiment on this compound discovered the superconductivity below 150 mK [98].

In the case of PrPdSn compound the results in literature are limited to polycrystalline samples. Adroja et al. [99] refers, that the compound does not order down to 4.2 K. On the other hand A. Zygmunt and A. Szytula reffer antiferromagnetic ordering with T_N = 4.3 K [50]. Neutron powder diffraction experiment done by Kolenda et. al. [100] resulted also to antiferromagnetic ordering with k = (0 1/2 1/2) at temperatures lower than 4.6 K. The susceptibility measured on the polycrystalline samples obeys Curie-Weiss law at temperatures above 30 K with μ_{eff} = 3.51 μ_B and Θ_p = -5.5 K.

In the case of NdPdSn compound A. Zygmunt et al. [50] refers that compound orders antiferromagnetically with T_N = 2.4 K, but Kolenda et al. [100] refers antiferomagnetic ordering already below 3.6 K with complicated incommensurate magnetic structure with

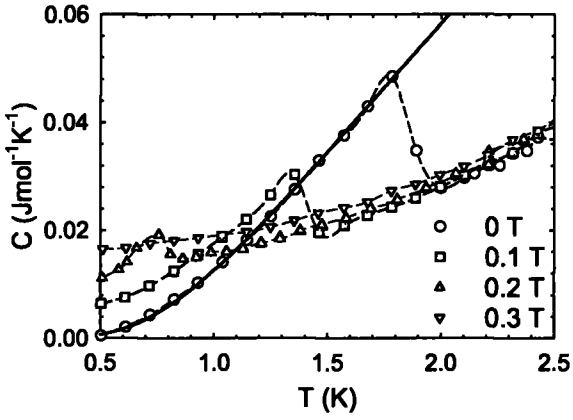

Figure 4.2: *The low temperature detail of LaRhSn specific heat measured in field applied along the c-axis. The dashed lines are guides for the eye. The full line is the best fit due to equation 4.1. The data were measured on crystal (ii).*

propagation vector k = (0.273 1/2 1/2). The susceptibility of NdPdSn also obeys the Curie-Weiss law at temperatures above 30 K with μ_{eff} = 3.68 μ_B and Θ_p = -11 K. Also in this case all previously published results were done on the polycrystalline samples.

4.1.2 ZrNiAl systems

LaRhSn

We have grown and measured two single crystals of LaRhSn (crystal (i) and crystal (ii)) by the modified Czochralski method in a tri-arc furnace in DCMP MFF UK under purified Ar atmosphere. The crystal growth was performed using about seven grams of a stoichiometric melt consisting of the elemental constituents. The purity of used starting materials was 3N for La, 3N5 for Rh and 3N for Sn. As a seed we have used a tungsten rod. The growing speed was between 8 and 12 mm/h.

The specific heat of LaRhSn in the temperature range 2 8 K can be fitted due to T^3 law. Due to this fit we have found γ = 10.9 mJ mol^{-1} K^{-2} and β = 6.2x10^{-4} J mol^{-1} K^{-4}. Then using equation 3.8 we have estimated Θ_D = 211 K.

Below 2 K, the specific heat of LaRhSn (Fig. 4.2) exhibits a lambda anomaly and reaches the maximum value C_s = 0.0485 J mol^{-1}K^{-1} at T_c = 1.85±0.05 K. This lambda anomaly we have ascribed to the transition from the normal state to the superconducting state. Value of T_c is just in between the values published by Canepa et al. [51] and Ho et al. [92]. When a magnetic field is applied along the *c*-axis the C(T) anomaly moves to the lower temperatures and becomes reduced. Finally, in the field of 0.3 T the peak is no more indicated in temperatures above 0.5 K. Below T_c the specific heat of LaRhSn can be fitted

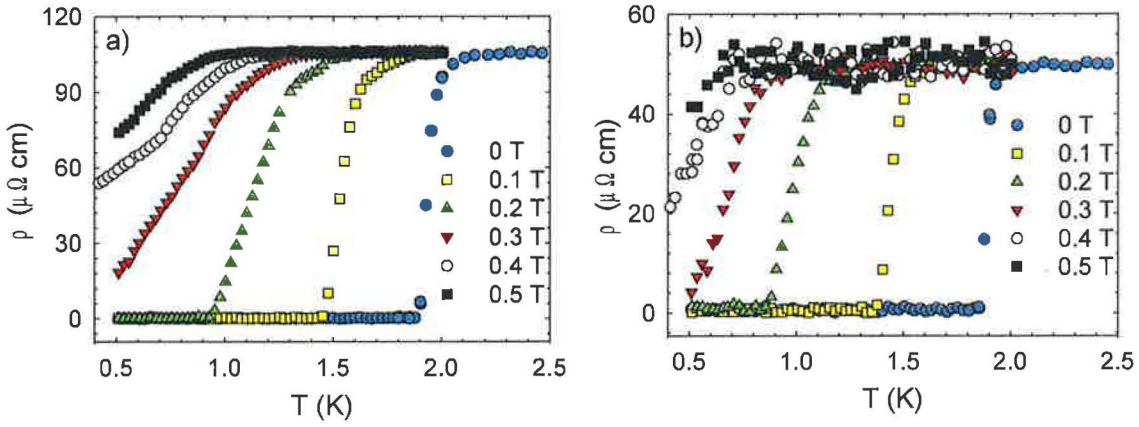

Figure 4.3: *The low temperature detail of LaRhSn resistivity measured on crystal (ii): a) Electrical current and magnetic field applied along the a-axis; b) Electrical current and magnetic field applied along the c-axis.*

by the relation:

$$C = \beta T^3 + ce^{-\Delta/T} \tag{4.1}$$

where the first term is associated with the phonon contribution to the specific heat and the second term is associated with the electronic contribution to the specific heat due to the energy gap between the normal and superconducting state. This equation differs from dependency predicted by BCS theory[1] by a prefactor $1/T^{3/2}$. During the fit we have fixed β to 6.2×10^{-4} J mol^{-1} K^{-4} - value obtained from fit of the specific heat in the normal state. The best fit (see Fig. 4.2) we have obtained for c = 0.23 J mol^{-1} K^{-1} and Δ = 3 K. One of the basic predictions of BCS theory is also the prediction of the relation between the electronic contributions to specific heat in the normal state C_{n-e} and in the superconducting state C_{s-e} at T_c [1]:

$$\frac{C_{s-e} - C_{n-e}}{C_{n-e}} \sim 1.43 \tag{4.2}$$

If we take C_{n-e} = 0.0202 Jmol^{-1}K^{-1} (calculated using γT relation with γ = 10.9 mJ mol^{-1} K^{-2}) and C_{s-e} = 0.0454 Jmol^{-1}K^{-1} (calculated from the second term in the equation 4.1) then the equation 4.2 result to the ratio 1.25. This is slightly lower than 1.43 predicted by the BCS theory [1]. If we consider Δ = 3 K to be the energy gap present in the superconducting state, then Δ/T_c = 1.62 which is again slightly less than 1.76 predicted from the BCS theory.

[1]Theory, which explains the conventional superconductivity. This theory is named after its creators J. Bardeen, L. Cooper, and J. R. Schrieffer. The basics of this theory can be found elsewhere [1]

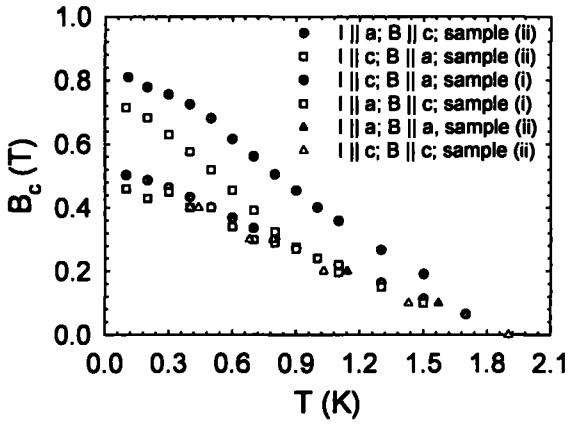

Figure 4.4: *The critical magnetic field B_{c2} as a function of temperature determined for both grown single crystals of LaRhSn. Circles and squares were derived from the field dependences of the resistivity at constant temperature and the triangles were derived from the temperature dependence of the resistivity at a fixed magnetic field.*

The relative resistivity measured on the crystal (ii) shows metallic behavior for temperatures above 2 K. In case that electrical current was applied along the a-axis the resistivity was about double of the resistivity measured for current applied along the c-axis. However the relative resistivities for both axes are similar and the RRR for current applied along the both the axes is about 7.5. At low temperatures the resistivity drops to zero value at T_c = 1.9 K (Fig. 4.3) which is in accordance with the lambda anomaly in the specific heat. This drop clearly indicates that LaRhSn is superconducting below T_c. When a magnetic field is applied along the current direction the superconducting transition shifts to lower temperatures (Fig. 4.3) and finally in fields higher than 0.2 T the T_c shifts below 0.5 K or the applied magnetic field completely destroys the superconductivity in this compound. The additional study of B_{c2}(T) dependences performed on both crystals in a ^{3}He^{4}He dilution refrigerator (experiment performed by S. Gabáni) and for both crystallographic directions revealed considerably different behavior between the configurations (I || a, B || c) and (I || c, B || a). These results are plotted in Fig. 4.4. For the field applied along the c-axis and the electrical current along the a-axis the B_{c2}(T) values increase nearly linearly with decreasing temperature with $B_{c2} \sim 0.5$ T at T = 0.1 K. In this case the shape of B_{c2}(T) curve is rather sample-independent. This agrees well with B_{c2}(T) data (also plotted in Fig. 4.4) derived from the ρ(T) results which were collected in various magnetic fields for (I || a, B || a) and (I || c, B || c). Strikingly different results were obtained on both samples for the magnetic field applied along the a-axis and electrical current applied along the c-axis. In this case the B_{c2}(T)curves show tendency to saturate below 0.4 K and also show sample dependent values of B_{c2} ($\sim$ 0.7 T for sample (i) and $\sim$ 0.8 T for sample (ii)) at the lowest-reachable temperature. These results are in good agreement with the results

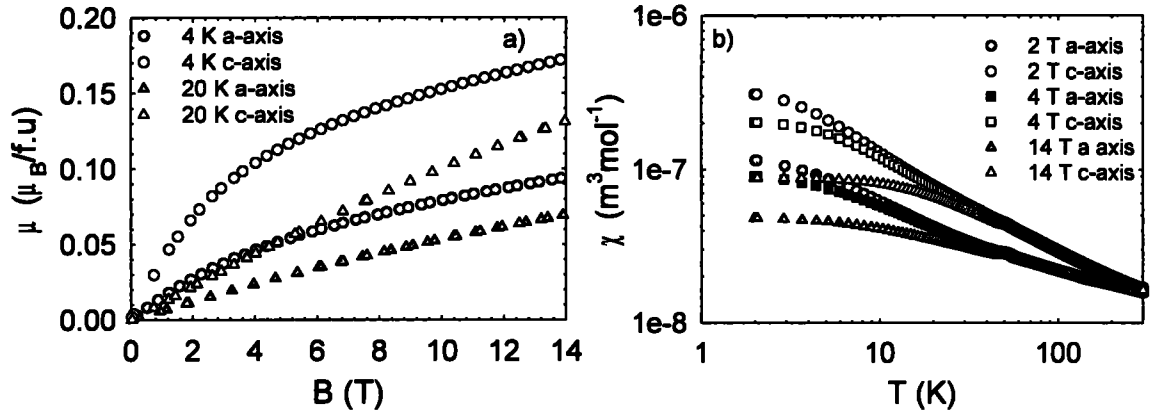

Figure 4.5: a) the mangetization curves of CeRhSn and b) the susceptibility of CeRhSn measured for both crystallographic orientations.

obtained on a polycrystalline samples [92].

CeRhSn

The single crystal of CeRhSn was grown by T. Komatsubara. We have just measure the physical properties of the grown single crystal.

The magnetization curves along both main crystallographic axes show very similar qualitative behaviour (Fig. 4.5a). Assuming that the Rh sites carry no magnetic moment, only 0.17 μ_B/Ce-ion for B || c and only 0.09 μ_B/Ce-ion for B || a in 14 T (at 4 K) can be derived. This is only small amount compared to the magnetic moment of the free Ce^{3+} ion (2.14 μ_B). However, the curves tend to be linear at higher fields with no tendency to saturation which may result to much higher magnetic moment in higher fields. We have also tried to fit the magnetization curves due to Brillouin function with aim to better determine the saturation magnetization moment in the compound but we have obtained unsatisfactory fits for all measured magnetization curves. Our χ(T) data (Fig. 4.5b) fit well with the results presented by Kim et. al. [93]. The logarithmic low-temperature χ(T) scaling for B || c can be interpreted in terms of non-Fermi-liquid (NFL) behavior. For both directions of magnetic field the $1/\chi$(T) dependences are strongly curved. The formal fitting of the data using a modified CurieWeiss law[2] (as attempted in Ref. [93]) yields parameters which are strongly dependent on the considered temperature interval. High-temperature data provide rather rough estimate of negative values of the paramagnetic Curie temperature of the order of several hundred K, which may be speculate as indication of strong hybridization of the Ce $4f$-electronic states with the valence-band states of the

[2]Modified curie Weiss law: $\chi(T) = \chi_0 + \frac{C}{T-\Theta_p}$

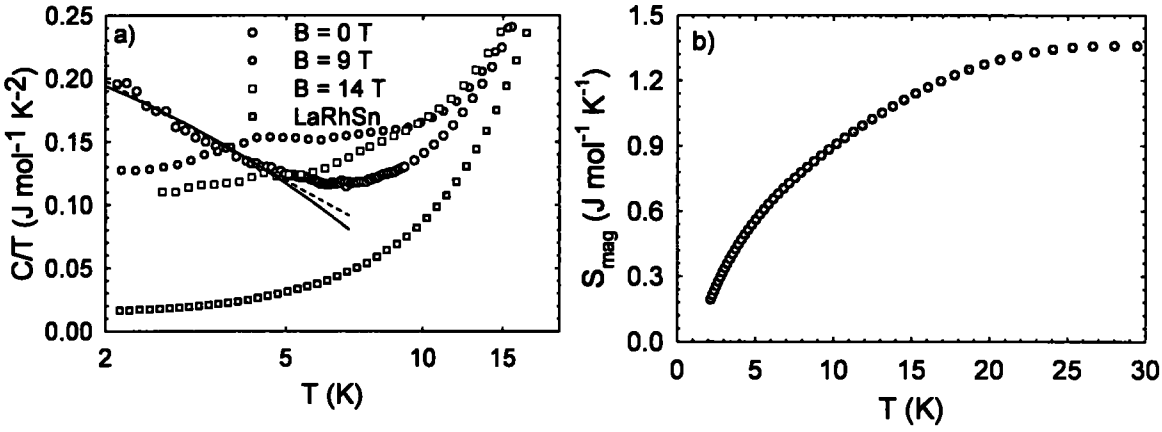

Figure 4.6: a) the evolution of the low temperature specific heat of CeRhSn due to magnetic field applied along the c-axis. The solid line represents the best fit for $C/T \sim \sqrt{T}$ and the dashed line represents the best fit for $C/T \sim -\ln T$. b) the magnetic entropy of CeRhSn.

ligands. This scenario is corroborated by the strongly reduced values of the Ce magnetic moment detected by the low-temperature magnetization curves (Fig. 4.5a)

Below 20 K the $C(T)$ curve of CeRhSn deflects from the normal-metal $C(T)$ dependence of LaRhSn reflecting some low-energy excitatons (Fig. 4.6a). Also the upturn in the C/T vs. T curve below 6.6 K points to the non-Fermi liquid behavior (see Fig. 4.6a). This upturn below 6.6 K can be fitted either by the equation $C/T \sim -\ln T$, used by Kim et al. [93] or alternatively by $C/T = \alpha - \beta\sqrt{T}$, reported for another non-Fermi liquid compound, $CeNi_2Ge_2$ [101]. Since the quality of the both fits is comparable we can not make any conclusions about the type of low temperature scaling. As can be seen from Fig. 4.6a the upturn in the specific heat can be suppressed by the magnetic field applied along the c-axis and finally at magnetic field of 14 T completely smeared out from the C/T curve. On the other hand when we have applied magnetic field along the a-axis the upturn in the specific heat remained intact. The suppression of the NFL "tail" has been observed also in the case of $CeNi_2Ge_2$ [101] with the equivalent impact for different field directions. To calculate the magnetic entropy of CeRhSn (S_{mag}) we have used the LaRhSn isostructural compound as an nonmagnetic analogue. The result of our calculations are plotted in Fig. 4.6b. The entropy monotonously increases at low temperatures with tendency of saturation at about 30 K. The value of entropy at 30 K is 1.36 $Jmol^{-1}K^{-1}$, which is only a minor fraction of $R \ln 2$.

The resistivity of CeRhSn (Fig. 4.7) measured along the c-axis (ρ_c) decreases monotonously with decreasing temperature. Such a behavior is typical for the normal metals. On the other hand the resistivity measured along the a-axis (ρ_a) firstly increases with decreasing temperature, passing the broad Kondo maximum at 54 K and exhibits a shoulder at

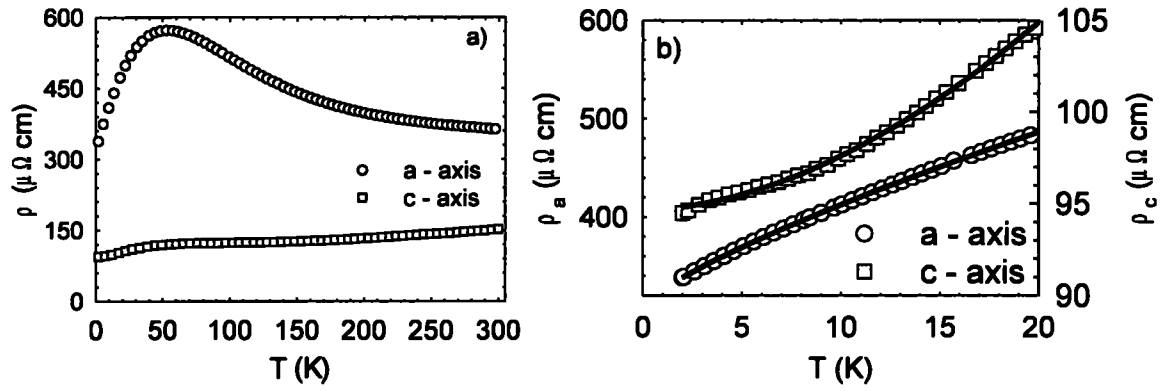

Figure 4.7: a) The full themperature plot of resisitvity of CeRhSn b) The low temperature detail of the resistivity of CeRhSn. The lines represent the best fits due to power laws.

about 3 K. Such a behavior is typical for the valence fluctuating systems. Taking into account also the fact, that ρ_a is at least two times higher than ρ_c in all temperatures the resistivity of CeRhSn points to strong anisotropy in this compound. The resistivity at temperatures lower than 20 K can be fitted by power law $\rho(T) = \rho_0 + AT^n$ with the positive A and the exponents 0.76 and 1.7 for the $\rho_a(T)$) and $\rho_c(T)$ respectively (see Fig. 4.7b). The power $n \neq 2$ also points to the NFL scenario in the CeRhSn compound. In our measurements the absolute values of the resistivity are higher than data published by Kim et al. [93]. Also the maximum in the a-axis resistivity data occurs at lower temperatures than in previously published data by Kim et al. [93]. The reason, why our results are slightly different from the results published in [93] may be the different quality of the single crystals, different amount of impurities and different real stoichiometry of the samples. The influence of the stoichiometry in CeRhSn compound was already published by Ślebarski et al. [94]. The result of the Ślebarski's experiment was that effects in CeRhSn compound are very sensitive to impurities and to off-stochiometry of the compound.

The thermal expansion experiment was performed using the Kyowa strain gages type SKF-5414 in the temperature range 5 – 300 K. As a calibration of strain gage we have measured the thermal expansion of the pure copper (purity 5N) which we have compared with the data published by Kroeger et al. [102] as a calibration data for the thermal expansion of copper. By the strain gage we were able to measure only the relative expansion of the matter. To calculate the temperature dependence of the lattice parameters we have then used the lattice parameters obtained from the X-ray powder diffraction at 300 K. The lattice parameters depend linearly on temperature in the temperature region 200 - 300 K (Fig. 4.8a). At temperatures lower than 200 K the experimental curve of c-axis vs. temperature slowly changes the slope and at the lowest temperatures tends to be temperature independent. The experimental curve of a-axis vs. temperature also slowly

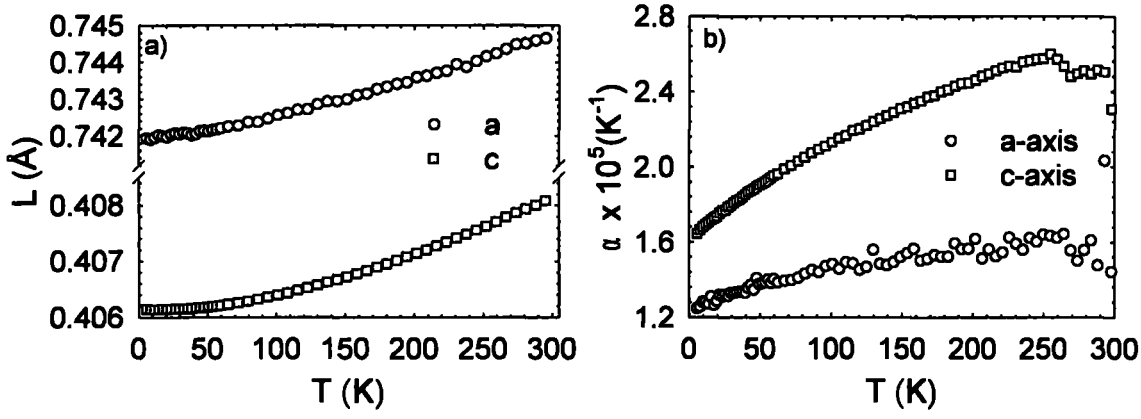

Figure 4.8: CeRhSn compound: a) the temperature evolution of the lattice parameters; b) the calculated temperature evolution of the coefficient of linear thermal expansion.

change the slope below 200 K, but the scatter at temperatures below 50 K causes that we can make no conclusions about behavior of the a lattice constant below this temperature. The a-axis lattice constant decreases from 300 K to 5 K by 0.34 % and the c-axis lattice constant decreases by 0.47 %. Applied field up to 14 T along the both main crystallographic axes does not affect the lattice parameters. We have tried to calculate the linear thermal expansion coefficient using equation $\alpha = (L - L_{300})/((L_{300}(T - T_{300}))$ where L is the lattice parameter and T is the temperature. The calculated α values (Fig. 4.8b) are of the order of 10^{-5} K^{-1}, which is comparable with α for the normal metals [102]. We have found no maximum reported by Ślebarski et al. [103] on the α/T vs. T curve.

PrRhSn

The PrRhSn single crystal was grown in the tri-arc furnace in DCMP MFF UK. The crystal growth was performed using about seven grams of melt consisting of the stoichiometric composition of the elemental constituents. The purity of used starting materials was 3N for Pr, 3N5 for Rh and 3N for Sn. As a seed we have used a tungsten rod. The growing speed was between 8 and 12 mm/h.

The specific heat of PrRhSn as a function of temperature exhibits a sharp peak at 2.85(3) K (Fig. 4.9a), which we associate with the ferromagnetic ordering phase transition. Our T_C is close to the Currie temperature published by Łątka et al. [96] for this material. Just above T_C we have found a bump in the specific heat (Fig. 4.9a) which shifts to higher temperatures and broadens with applied magnetic field along the c-axis. We attribute this feature to a Schottky contribution to the specific heat. In order to determine the magnetic part (C_{mag}) of the specific heat and subsequently to determine the Schottky contribution we have used LaRhSn as an nonmagnetic analogue. Also we have used the

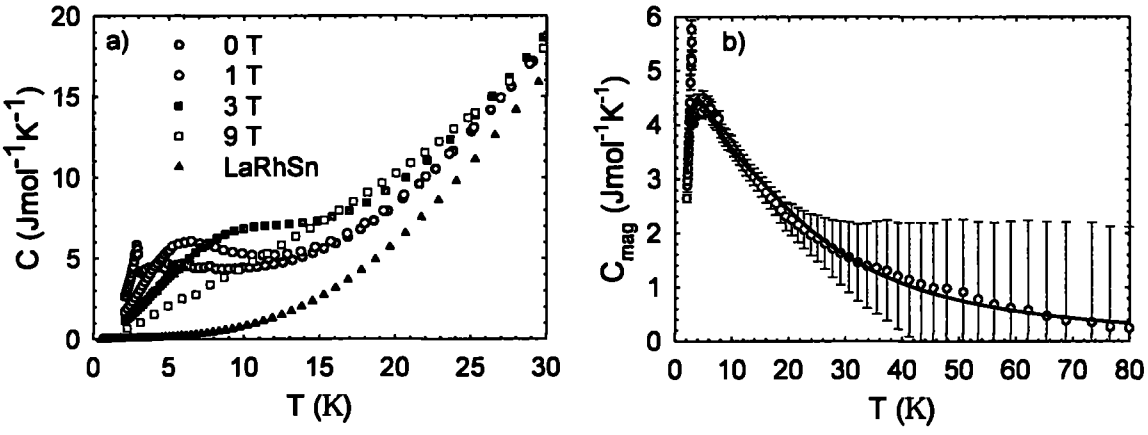

Figure 4.9: a) The low temperature of the specific heat of PrRhSn measured in magnetic field applied along the c-axis. b) comparison of the magnetic part of the zero-field specific heat of PrRhSn (circles) and theoretical fit due to Schottky contribution (line).

correction to the specific heat due to the different molar masses (equation 3.11) of LaRhSn and CeRhSn. The reasons why we have used LaRhSn as an nonmagnetic analogue is that the LaRhSn specific heat fits to the PrRhSn specific heat for temperatures above 35 K very well, both compounds have the same crystal structure and LaRhSn is compound in which one does not suppose to have C_{mag}. The C_{mag} vs. T plot is displayed in Fig. 4.9b. The crystal field at the Pr site is orthorhombic and it splits the ground state multiplet into nine singlets. The error in determining C_{mag} increases with temperature which is caused by the problem of subtracting two big numbers, both burdened with some experimental error. For temperatures above 80 K the error of C_{mag} became too large to fit this data that's why we have fitted C_{mag} only in temperature range 3.11 –80 K. According to the fit in this temperature region we were able to find four levels of the splitting of the ground state multiplet: 0 K (fixed level); 7.03(7) K; 19.0(1) K; 47(1) K.

The magnetic entropy calculated from C_{mag} saturates to the value of $R \ln 4$ (Fig. 4.10a) already at 60 K, which is consistent with the discussed CF-level scheme. After applying the magnetic field along the c-axis the entropy substantially decreases which opens the space for the speculation of using this compound for the magnetic cooling. The maximum change of entropy in field applied along the c-axis occurs at 4.3 K for B = 1 T (Fig. 4.10b). This maximum shifts to the higher temperatures with applying a higher magnetic field, reaching 9.9 K in 9 T. Such a large change of entropy at low temperatures one can use for example for magnetic cooling at temperatures near 10 K.

The AC susceptibility (see Fig. 4.11a) reaches maximum at 2.9(1) K for the a-axis data. The c-axis AC susceptibility (see Fig. 4.11b) was found to be temperature independent at temperatures below 2.8(2) K. These effects are consequences of the magnetic ordering and

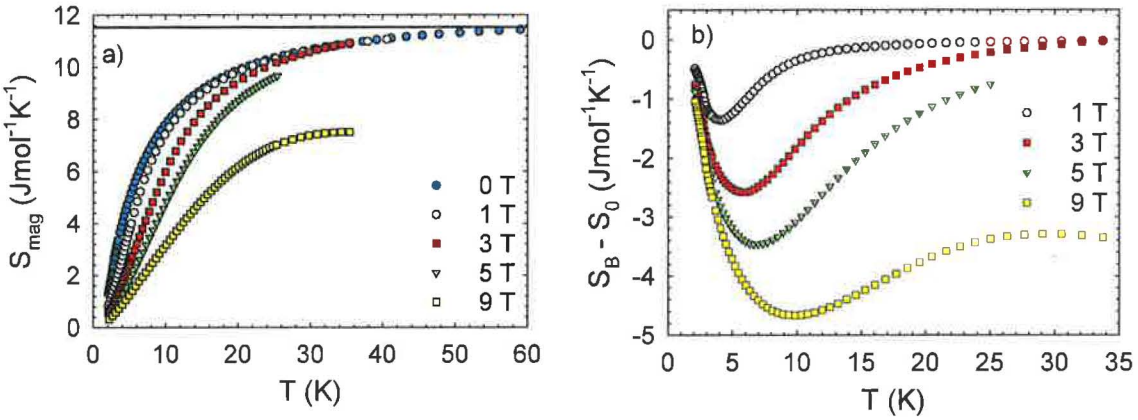

Figure 4.10: *a) The magnetic entropy calculated for PrRhSn compound and its evolution in the magnetic field applied along the c-axis. For this calculation we have also used the linear approximation from the lowest-measured point to the $S = 0$ $Jmol^{-1}K^{-1}$ for $T = 0$ K. The line represents the value $R\ln 4$. b) the relative difference of magnetic entropy.*

are in good agreement with magnetization data published on polycrystals by Łątka et al. [96]. The temperature dependence of the dc magnetization in the vicinity of T_C measured in the magnetic field of 20 mT applied along the c-axis exhibits a cusp very near to T_C. This feature is immediately smeared out with higher magnetic field, vanishing already in field of 50 mT. When we have measured the DC magnetization in the vicinity of T_C in magnetic fields applied along the a-axis, we have recorded the spurious signals of the order of 1% of the corresponding values measured in fields applied along the c-axis. We ascribe these signals to projections from the c-axis signals, which appear due to mosaicity of the crystal and/or slightly imperfect orientation of the single crystal.

The c-axis magnetization curve measured at 2 K (see Fig. 4.12a) provides a further evidence of ferromagnetism with a spontaneous magnetic moment of approximately 2 μ_B/f.u. The magnetization also saturates at fields higher than 6 T with the saturated magnetic moment of 3.5 μ_B/f.u., which is somewhat higher than $gJ\mu_B = 3.20$ μ_B (theoretical value of saturated magnetic moment for free Pr^{3+} ion). The magnetization curve measured at 10 K in a field applied along the c-axis can be fitted by the Brillouin function (line in Fig. 4.12a). From this fit we have obtained a saturated magnetization $M_{sat} = 3.6$ μ_B/f.u., which is again somewhat higher than the theoretical moment of Pr^{3+} free ion. The excess magnetic moment can be understood for example in terms of induced moments of $\sim 0.2\mu_B$ and $\sim 0.1\mu_B$ due to the polarized Rh $4d$-electron states and Sn $5p$-states as published in [6]. The magnetization measured in B || a configuration is much smaller and proportional to the field up to 9 T. This result demonstrates strong uniaxial magnetocrystalline anisotropy with the c-axis to be an easy magnetization axis. When we have extrapolated the a-axis

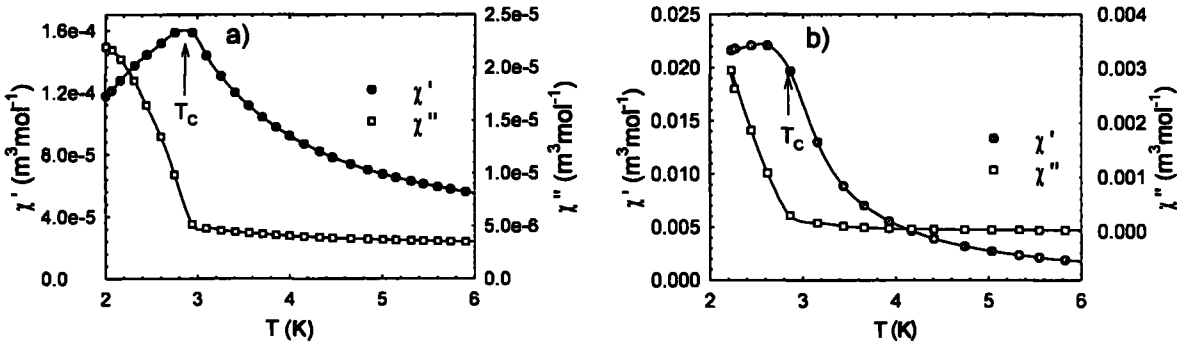

Figure 4.11: The AC susceptibility measured on the PrRhSn compound at field of 10 Oe-with frequency of 1000 Hz: a)applied along the a-axis b) applied along the c-axis. The lines are guides for the eye. The plotted T_C has the value as determined from the specific heat measurements.

magnetization we have estimated that a-axis magnetization will reach te value of the c-axis magnetization at approximately 65 T. This value can be used as a first approximation of the anisotropy in the compound.

The paramagnetic inverse susceptibility is also strongly anisotropic (Fig. 4.12b), but linear in temperatures above 50 K for the a-axis and above 150 K for the c-axis, respectively. Fit using the CurieWeiss law at temperatures above 50 K for the a-axis and above 150 K for the c-axis, respectively resulted to effective moment $\mu_{eff,a} = 3.3\ \mu_B$/f.u. and paramagnetic Curie temperature $\Theta_{P,a}$ = -42.5 K for the a-axis and $\mu_{eff,c} = 3.5\ \mu_B$/f.u. and $\Theta_{P,c} = 38$ K for the c-axis. The large difference in the Θ_p values reflect the strong anisotropy present also in the paramagnetic range whereas the values of the effective magnetic moment determined for the two principal directions are not far from the value of the free Pr^{3+} ion. The pronounced curvature of the $1/\chi$ vs. T plots at lower temperatures documents a considerable crystal field influence.

The electrical resistivity of PrRhSn measured along both main crystallographic axes exhibit a metallic behavior above 20 K. At lower temperatures the resistivity goes through a broad bump extended up to 20 K. The transition temperature is not significant on the resistivity data (Fig. 4.13), but it is clearly visible on the temperature derivative of the resistivity. In case of transversal magnetoresistivity the magnetic field suppress the resistivity for both measured configurations i || a; B || c and i || c; B || a. This resulted to a considerable negative magnetoresistance in the temperature interval 2 – 20 K. Although we are not able to provide a rigorous theoretical explanation we believe that the bump on the temperature dependence of the resistivity is mostly due to CF influence, which becomes suppressed in magnetic fields applied along the c-axis.

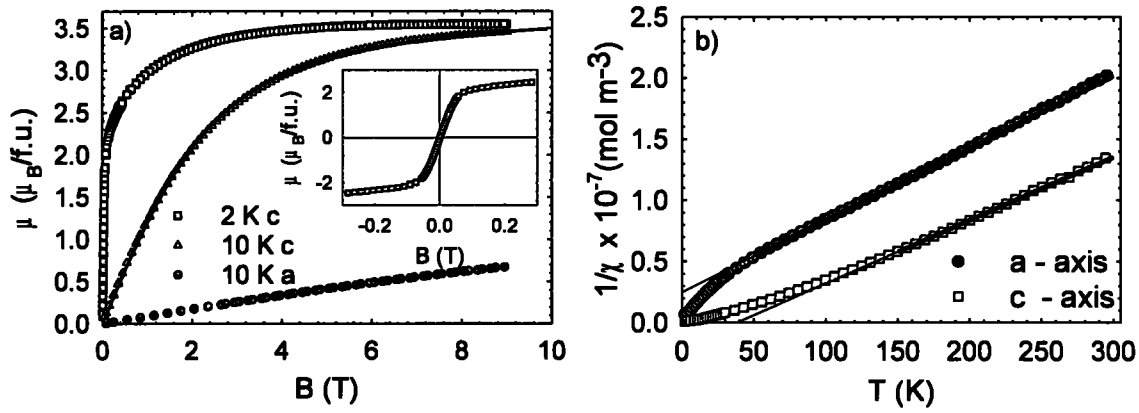

Figure 4.12: a) the magnetization curves of PrRhSn measured in the magnetic field applied along the c-axis (open symbols) at 2 K and 10 K and along the a-axis (full symbols) at 10 K. In inset we have plotted the hysteresis loop measured at 2 K in the magnetic field applied along the c-axis. b) temperature dependence of the inverse magnetic susceptibility measured on a PrRhSn single crystal along the a- and c-axis, respectively. The lines represent the theoretical fits using the CurieWeiss law.

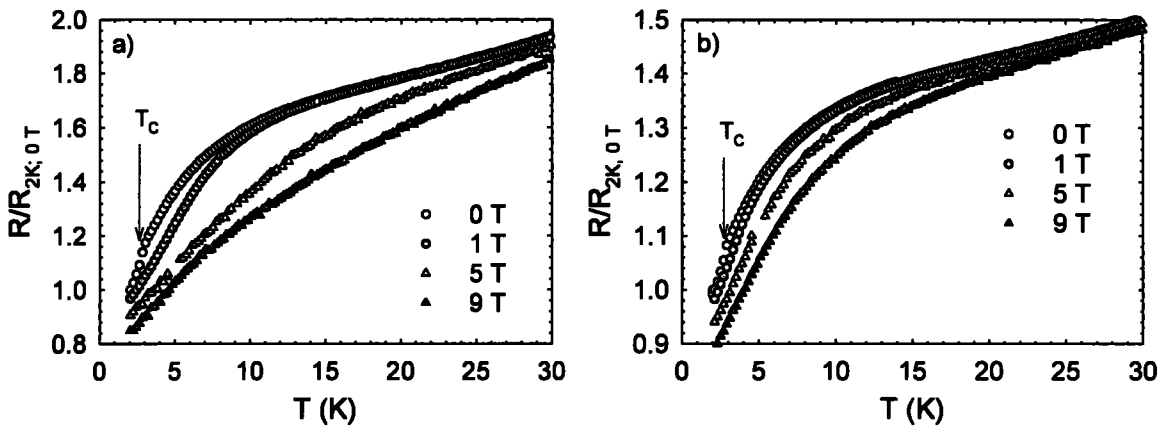

Figure 4.13: The low temperature detail of PrRhSn resistivity and magnetoresistivity: a) configuration i || a; B || c b) configuration i || c; B || a

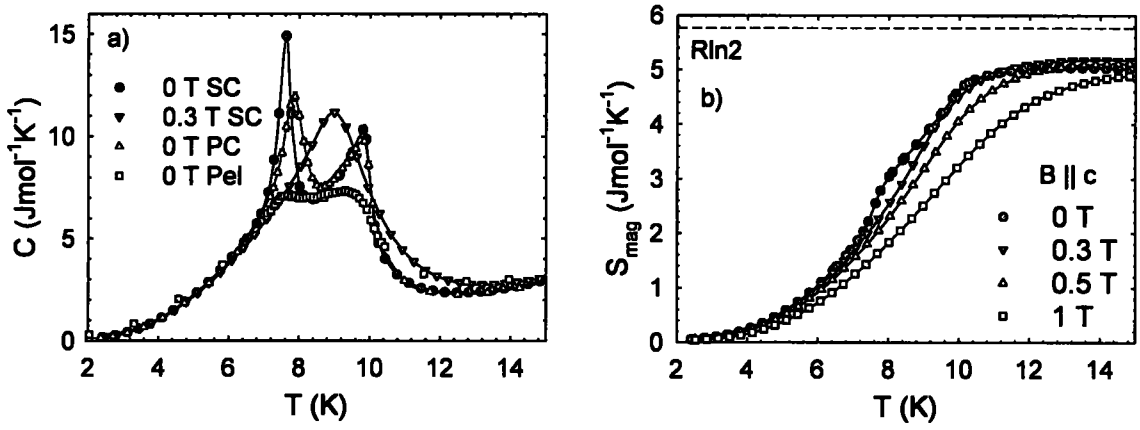

Figure 4.14: a) the specific heat (C) of NdRhSn measured on single-crystalline sample (SC) in B || c configuration compared with the measurement done on polycrystalline sample (PC) and on the pellet made from pressed powder (Pel). b) the magnetic entropy calculated from the single crystal C data.

NdRhSn

In case of NdRhSn we have grown two single crystals: one in tri-arc furnace in DCMP MFF UK and second in NIMS in tetra-arc furnace. The single crystal grown in Prague we have used for specific heat, magnetization, susceptibility, resistivity and magnetoresistivity measurements. The single crystal grown in NIMS we have used for a single crystal experiment on VIVALDI diffractometer in ILL. Also we have prepared a polycrystalline sample of NdRhSn which we have used for neutron powder diffraction on D1B diffractometer in ILL and also for checking the specific heat of the polycrystalline sample.

The specific heat of NdRhSn shows two distinct anomalies below 10 K (Fig. 4.14a). Both anomalies we have observed on single crystal, polycrystal and also on the pressed powder sample. So due to specific heat measurements there are two magnetic phase transitions at 9.8 K and 7.6 K. This is in contrary to only ferromagnetic phase transition at T_C = 10 K published by Łątka et al. [54, 97]. After applying small field (0.3 T) along the c-axis the "two-peak" structure was destroyed and only one broader peak remained. Using the comparative analysis of the specific heat and LaRhSn as an nonmagnetic analogue we have calculated the magnetic contribution to the specific heat and subsequently the magnetic entropy of the compound. The magnetic entropy of NdRhSn firstly increases and then saturates to values less than $R \ln 2$ at temperature around 10 K. Also the entropy decreases with increasing magnetic field B || a-axis (Fig. 4.14b).

The magnetization measured for B || c-axis exceeds the magnetization measured for B || a-axis for all temperatures and all magnetic fields (Fig. 4.15). This result confirms the pronounced uniaxial anisotropy with the easy magnetization direction confined to the

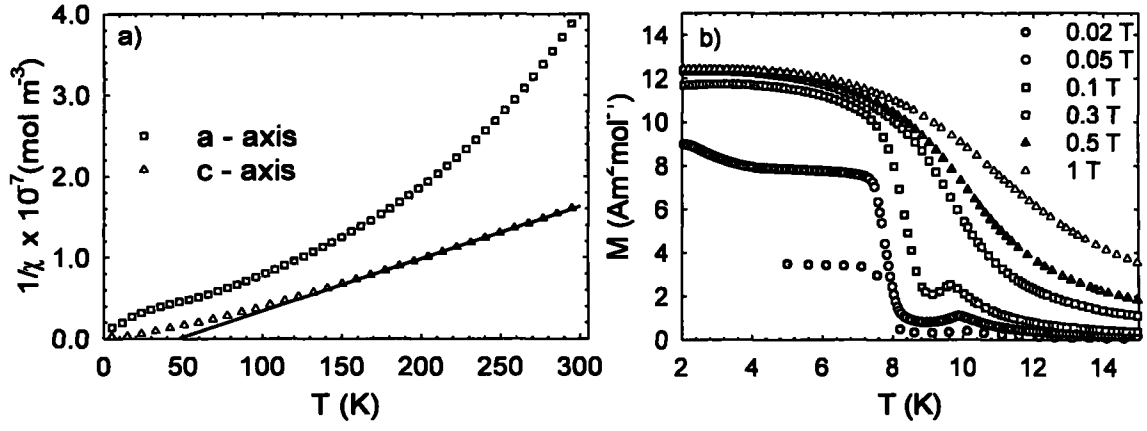

Figure 4.15: *a) the inverse susceptibility of NdRhSn. The line represent the best fit using the Curie-Weiss law. b) the low-temperature behavior of magnetization of NdRhSn.*

c-axis. The high temperature inverse susceptibility is linear only in case of the c-axis. For this axis we were also be able to fit Curie-Weiss law in temperature range 150 – 300 K. The resulted parameters were Θ_D = 47 K and μ_{eff} = 3.14 μ_B. At low temperatures and magnetic fields of 0.05 T we have observed on the c-axis magnetization a cusp at 9.9 K and an abrupt increase below 8 K (see Fig. 4.15b). When the magnetic field was increased the 9.9 K cusp moved to the lower temperatures and smeared out already in fields larger then 0.1 T. Also the position of abrupt increase of magnetization below 8 K shifted to the higher temperatures with the higher magnetic field. This suggests that the higher phase transition is from the paramagnetic to the antiferromagnetic state and the lower transition is from the antiferromagnetic to ferromagnetic state.

The low-temperature magnetic isotherms are shown in Fig. 4.16. The magnetization measured along the a-axis is much smaller than along the c-axis and the M(B) dependence is almost linear down to the lowest temperatures. In contrast, the c-axis magnetization measured at temperatures below 7.6 K saturates already in low fields to the value of 2.24 μ_B/f.u. which also can be taken as a good estimate of the spontaneous magnetic moment in the low-temperature limit. This value is however considerably smaller than the theoretical moment of a free Nd^{3+} ion.

Fragility of the antiferromagnetic phase is documented by the onset of the metamagnetic transition indicated by magnetization curves (Fig. 4.16b) at magnetic field between 0.08 T and 0.1 T and temperatures between T_N and T_C. The existence of the metamagnetic transition itself is further argument for antiferromagnetism between 7.6 and 9.8 K. The c-axis magnetic isotherms measured below T_C (Fig. 4.16a) show behavior as expected for a ferromagnet: the moment firstly increases with applied magnetic field and then saturates.

We have performed two different hydrostatic pressure experiments on two different

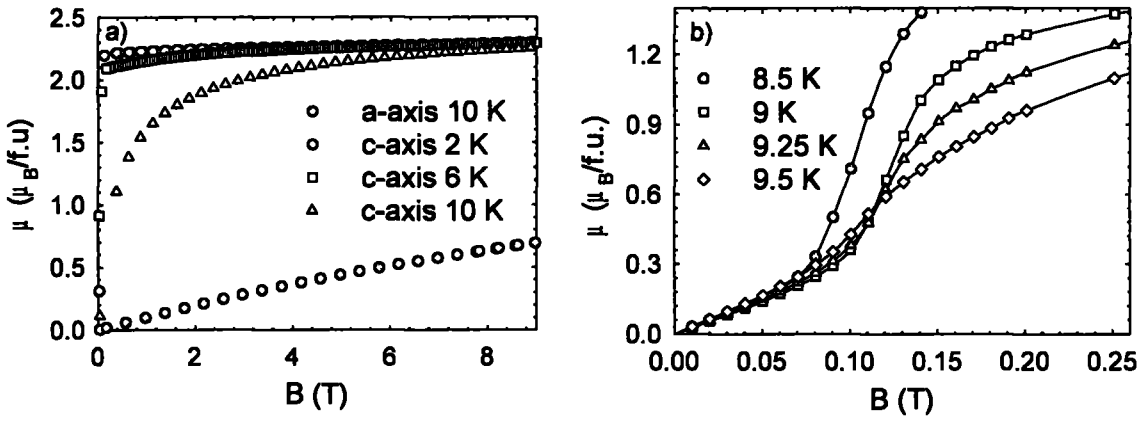

Figure 4.16: The magnetization of NdRhSn. a) measured along both crystallographic axes b) low field detail for the c-axis magnetization.

hydrostatic pressure cells. One experiment was done in Prague and one in NIMS. The details of used pressure cells are summarized in section 3.6. When we have measured the magnetization under applied hydrostatic pressure we have found that both T_N and T_C linearly shift to lower temperatures with applied hydrostatic pressure (see Fig. 4.17) by $\partial T_N/\partial p = -0.76$ K/GPa and $\partial T_C/\partial p = -1.10$ K/GPa. In case of T_N the data measured in Prague and NIMS fit together very well, but in case of T_C the results measured in NIMS are systematically higher then those obtained in Prague. The probable reason for this is, that we have measured the transition in field of 0.01 T, which is still small enough to see also the superconducting transition of lead. This transition occurs at around 7 K, so very close to T_C of NdRhSn. As lead was quite close to the sample (cca 3 – 5 mm) the signal from lead is superimposed on the signal from the sample. That's why we suppose that for the study of the T_C the pressure experiments performed in NIMS are more accurate than the pressure experiments performed in Prague.

The evolution of metamagnetic transition in applied hydrostatic pressure (Fig. 4.17b) resulted to the behavior that metamagnetic transition shifts to the higher fields with applied higher hydrostatic pressure. This tendency we have observed for temperatures 8.2 K, 8.6 K, 9 K and 9.3 K. Also at 10 K (in paramagnetic state) we have observed slight decreasing of the magnetization with increasing the hydrostatic pressure. But this might be connected with shifting of the T_N with applied hydrostatic pressure. On the other hand, magnetization curve measured at 5 K remained intact to the applied hydrostatic pressure.

The neutron powder diffraction pattern (Fig. 4.18a) measured at temperatures lower than 9.4 K can be completely indexed by integer *hkl* indexes. This is in contradiction to our other measurements in which we have observed two magnetic phases. To obtain the magnetic contribution to neutron powder diffraction pattern we have subtracted the

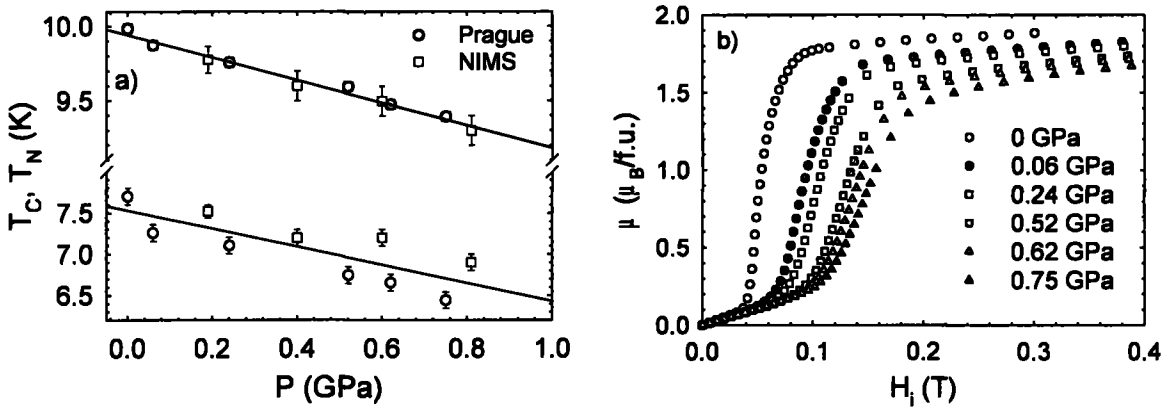

Figure 4.17: The hydrostatic pressure experiment on NdRhSn: a) the evolution of T_N and T_C. The lines represent the best linear fit. b) the evolution of the metamagnetic transition at $T = 8.2$ K.

powder pattern measured at 14 K from the patterns measured at lower temperatures. Then, we have performed Rietveld fitting of the magnetic part of neutron powder pattern using program *FullProf* [13]. We have obtained the best Rietveld fit for magnetic moments localized only on the Nd^{3+} and alligned along the c-axis. The resulting magnetic moment (Fig. 4.18b) saturates for temperatures lower than 7 K to the value 2.2(1) μ_B/Nd which is in very good agreement with our bulk measurements data. At 9.4 K the magnetic part of the diffraction pattern completely vanishes.

The subsequent single crystal experiment was performed by J. Prokleška and is summarized in [104]. The result of this experiment is, that we have confirmed antiferromagnetic phase with the propagation vector k = (0 0 0.0904) at temperature range 7 –10 K and ferromagnetic ordering below 7 K.

4.1.3 TiNiSi systems

LaPdSn

LaPdSn single crystal was grown in the tetra-arc furnace in NIMS. The crystal growth was performed using about 7.7 grams of melt consisting of the stoichiometric composition of the elemental constituents. The purity of used starting materials was 3N for La, 3N5 for Pd and 5N for Sn. As a seed we have used a tungsten wire. We have decided to use the growing speed of 6 mm/h and by this growing speed we have obtained good LaPdSn single crystal.

We have measured LaPdSn as a nonmagnetic analogue for comparative analysis of the specific heat for PrPdSn and NdPdSn. Its specific heat (Fig. 4.19) was found with no

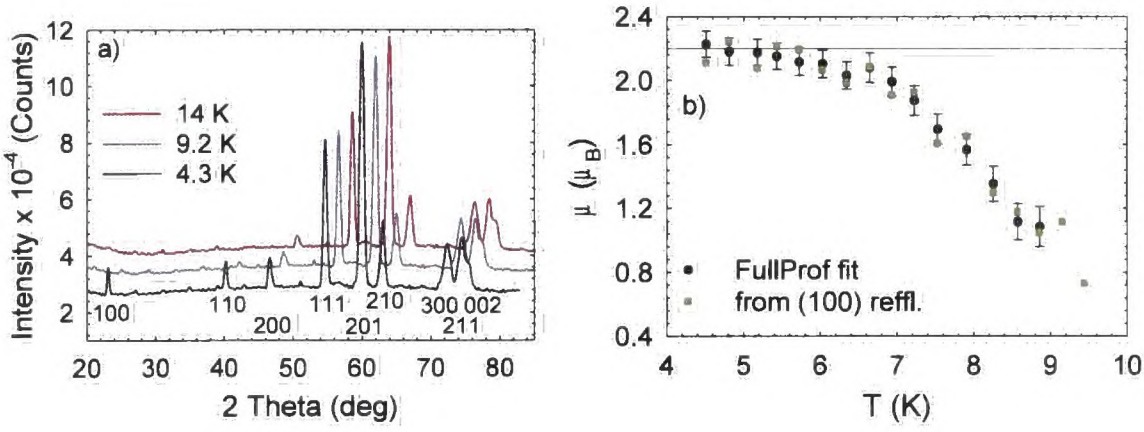

Figure 4.18: *Neutron powder diffraction data of NdRhSn: a) the example of the powder pattern; b) the evolution of the magnetic moment of* Nd^{3+}.

anomaly which should refer to some phase transition for temperatures higher than 1.9 K. The specific heat was fitted in the whole temperature range using only Debye theory for phonon contribution and γT relation for electronic contribution to specific heat. The fitted constants are $\gamma = 11(1)$ mJmol^{-1}K^{-2} and $\Theta_D = 196(1)$ K.

The resistivity of LaPdSn show a metallic character down to 0.4 K. These results are in an agreement with the previously published one [51]. At 0.4 K we have observed the onset of the superconducting transition. However this superconducting transition is just at the lowest-reachable temperature in our system (approximately 0.37 K). Nevertheless we can claim, that LaPdSn is superconducting with critical temperature close to 0.4 K.

PrPdSn

PrPdSn single crystal was grown in the tetra-arc furnace in NIMS. The crystal growth was performed using about 8 grams of melt consisting of the stoichiometric composition of the elemental constituents. The purity of used starting materials was 3N for Pr, 3N5 for Pd and 5N for Sn. As a seed we have used a tungsten wire. The good single crystal was grown using the growing speed from 6 mm/h (necking and increasing the diameter) to 10 mm/h (decreasing the diameter of grown ingot).

In the specific heat data (Fig. 4.19 and Fig. 4.20a) we have found a peak at 4.2(1) K. This peak we have assigned (taking into account also magnetization and resistivity measurements presented below) to the paramagnetic-antiferromagnetic phase transition with $T_N = 4.2(1)$ K. Our measured T_N is lower than the one published from powder neutron diffraction data [100]. The peak shifts to the lower temperatures with field applied along the b-axis and completely smears out at magnetic field of 1 T. Monoclinic local crystal field on the site of Pr atoms splits the ground state of Pr ion into 9 singlet states. That's

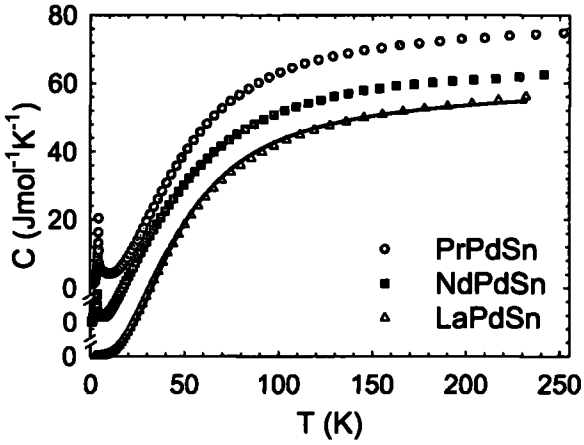

Figure 4.19: *The comparison of the specific heat of REPdSn compounds (RE = La, Pr and Nd). Data for PrPdSn and NdPdSn are shifted to make figure more obvious.*

why one can obtain the magnetic ordering in PrPdSn only if the energy difference between ground state and first excited state is small enough to mix them together and form a quasidoublet state. To find a magnetic contribution to the specific heat we have used LaPdSn specific heat as a nonmagnetic analogue. After subtracting the LaPdSn specific heat from the PrPdSn specific heat we have found some magnetic contribution to the specific heat at temperatures from 5 to 15 K which we have ascribed to Schottky contribution to specific heat. We were able to fit this enhancement by four Schottky levels: 0 (fixed level), 12(2) K (two levels at the same energy) and 63(5) K. So it seems, that ground state is quasitriplet state formed from Schottky levels 0 K and two levels close to 12 K. The magnetic entropy calculated from the magnetic contribution to the specific heat (Fig. 4.20b) increases almost linearly at lowest temperatures, changing the slope at T_N. This suggests that the phase transformation at T_N is of the second order. The magnetic entropy reaches value $R \ln 3$ at 4.2 K which is another indication for quasitriplet as a ground state.

The inverse susceptibility measured for all three main crystallographic directions (Fig. 4.21a) was found to be linear at higher temperatures. We have successfully fitted the Curie-Weiss law in temperature range 100 – 300 K for a-axis and in temperature range 50 – 300 K for b- and c-axis. The obtained Curie temperatures are $\Theta_{P,a}$ = -27.8 K; $\Theta_{P,b}$ = 11.3 K and $\Theta_{P,c}$ = -40 K, respectively. The fitted effective moments are $\mu_{eff,a}$ = 3.57 μ_B; $\mu_{eff,b}$ = 3.69 μ_B and $\mu_{eff,c}$ = 3.70 μ_B, respectively. The completely different Θ_P for all crystallographic axes is the consequence of the strong anisotropy in this compound (will be discussed later). However, the interesting result is that Θ_P is positive for field applied along the b-axis and negative for other two directions. The effective moment obtained for different crystallographic axes is almost the same and slightly higher than the theoretical moment of free Pr^{3+} ion. At low temperatures (Fig. 4.21b) we have found the anomalies on the

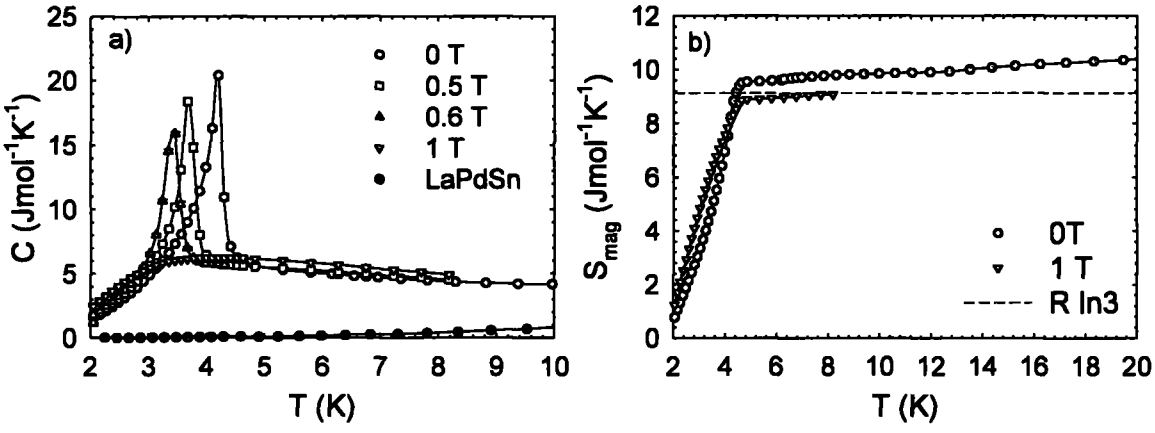

Figure 4.20: *PrPdSn compound: a) the low temperature detail of the specific heat show the evolution of the T_N with respect to the magnetic field applied along the b-axis. b)the calculated magnetic entropy. For this calculation we have also used the linear approximation from the lowest-measured point to the $S = 0$ $Jmol^{-1}K^{-1}$ for $T = 0$ K.*

susceptibilities connected with T_N: the maximum on b- and c-axis data, while in case of a-axis data abrupt increase of susceptibility at T_N and tendency of saturation at lower temperatures. When we have applied higher magnetic field, we have observed the shift of anomalies: in case of a-axis the anomaly shifted to higher temperatures with higher magnetic field, but in case of b- and c-axis the anomalies shifted to lower temperatures with applied higher magnetic field. The results of the shifting of the anomalies connected with T_N are summarized in magnetic phase diagram of PrPdSn (Fig. 4.22). Taking into account all these results we can conclude that there is a ferromagnetic coupling of magnetic moment along the a-axis and an antiferromagnetic coupling of magnetic moments along the b- and c-axis. These results are in very good agreement with the neutron diffraction data presented by Kolenda et al. [100]. We have found no differences between zero field cooled and field cooled susceptibility measured at 0.01 T.

The strong crystal field in the PrPdSn compound resulted to the case in which the b-axis is an easy magnetization direction, which is clearly visible from Figure 4.22b. We have observed the metamagnetic transition for the b-axis magnetization which occurs at 0.78(2) T at 1.9 K. The metamagnetic transition at higher temperatures than 1.9 K occurs at the lower applied magnetic fields, reaching 0.32 T at 4.1 K and completely smearing out at T_N. Also we have observed that 14 T is not enough to induce the metamagnetic transition along the a- and c-axis, nor enough to saturate moment along these two axes. This is also the consequence of the strong crystal field in PrPdSn compound. According the molecular field approximation, each Pr ion feels the effective field from all other ions according to equaiton 2.27. When we have included this effective field, we have found

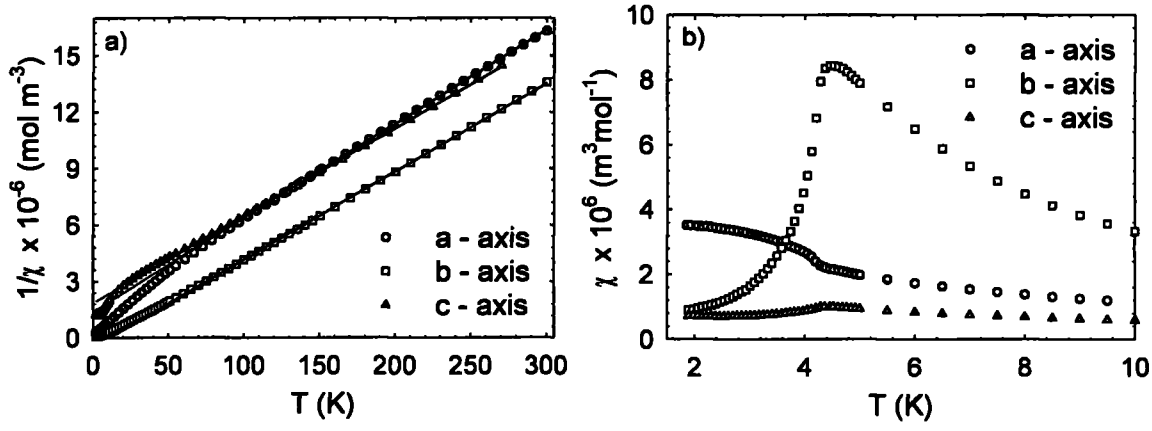

Figure 4.21: The a) inverse susceptibility measured by applied field of 1 T and b) detail of the susceptibility of PrPdSn measured along all main crystallographic axes for field of 0.01 T. The lines represent the best fit due to the Curie-Weiss law.

	ρ_0 ($\mu\Omega$cm)	A ($\mu\Omega$cmK^{-2})	B ($\mu\Omega$cmK^{-5})
a-axis	8.12(6)	0.11(1)	0.0021(1)
b-axis	11.45(5)	0.18(1)	0.0017(1)
c-axis	14.81(6)	0.26(1)	0.0010(1)

Table 4.3: The obtained parameters for PrPdSn resistivity fitted to equation 4.3 in the magnetically ordered state.

that the $M(B)$ curves of PrPdSn measured at $T = 10$ K can be fitted using the Brillouin function where H is replaced by H_{eff} according to equation 2.27 and as J and $g(JLS)$ is taken the theoretical values for the Pr^{3+} ion (see Fig. 4.22b). The saturated moments obtained from the fits amount 2.07, 2.95 and 1.23 μ_B for the a-, b- and c-axis, respectively and the obtained ν amount -0.71, 1.95, -4.79 T/μ_B, respectively. The saturated magnetic moments are considerably smaller than the Pr^{3+} ion expectation value (3.20 μ_B) apparently due to the lack of population of higher energy crystal field levels. The signs of the ν in the $M(B)$ curves fits are the same as the signs of Θ_P in the fits of the $M(T)$ curves, which is expected as the both fits were done within the same approximation.

The PrPdSn resistivity (Fig. 4.23) decreases with decreasing temperature for all three main crystallographic axes, passing a knee at T_N. Below 4.2 K we have tried to fit the resistivity using the Andersen's model for the magnetic contribution to the resistivity, however, the obtained parameters from the fit were unsatisfactory. That's why we have tried to describe the resistivity below 4.2 K using only electron-electron, electron-lattice imperfection and electron-phonon scattering events. Hence we have described the resistivity

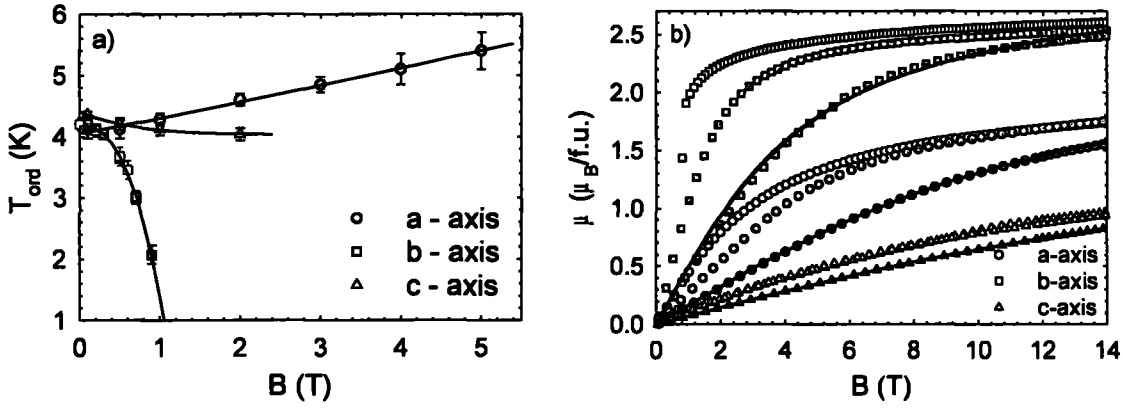

Figure 4.22: *PrPdSn compound: a) the phase diagram constructed from the anomalies in the magnetization data (color symbols) and using the specific heat data (opened symbols). The lines are guides for the eye. b) the magnetization curves measured along all three main crystallographic axes at 1.9 K (opened symbols); 5 K (lighter symbols) and at 10 K (darker symbols). The lines represent the best fit due to Brillouin function.*

by the equation:

$$\rho = \rho_0 + AT^2 + BT^5 \tag{4.3}$$

The results from the fitting are summarized in the Table 4.3 and graphically compared with the experimental data in Fig. 4.23b. The coefficient A can be used to checking the Kadowaki-Woods relation [105]. Testing the Kadowaki-Woods relation we have found that A/γ^2 (γ taken from LaPdSn nonmagnetic analogue) parameter has approximate value of 10^{-3} $\mu\Omega$cm mJ^{-2}mol^{2}K^2 instead of 10^{-5} $\mu\Omega$cm mJ^{-2}mol^{2}K^2. So the compound does not obey the Kadowaki-Woods relation. After applying magnetic field parallel to the electrical current we have observed only shift of transition in case of a-axis. In case of b-axis we have observed completely smearing out the magnetic transition in fields around 1 T, which scale perfectly with critical field for metamagnetic transition measured on magnetization. In case of c-axis we have found no response of the resistivity to the magnetic field (Fig. 4.23b).

NdPdSn

NdPdSn single crystal was grown in the tetra-arc furnace in NIMS under the similat experimental conditions as in case of PrPdSn single crystal.

The specific heat data of this compound (Fig. 4.24a) revealed two peaks: at T_N = 3.4(1) K and at T_1 = 1.91(3) K. The higher peak occurs close to the temperature at which also Kolenda et al. [100] reported the paramagnetic-antiferomagnetic phase transition, but

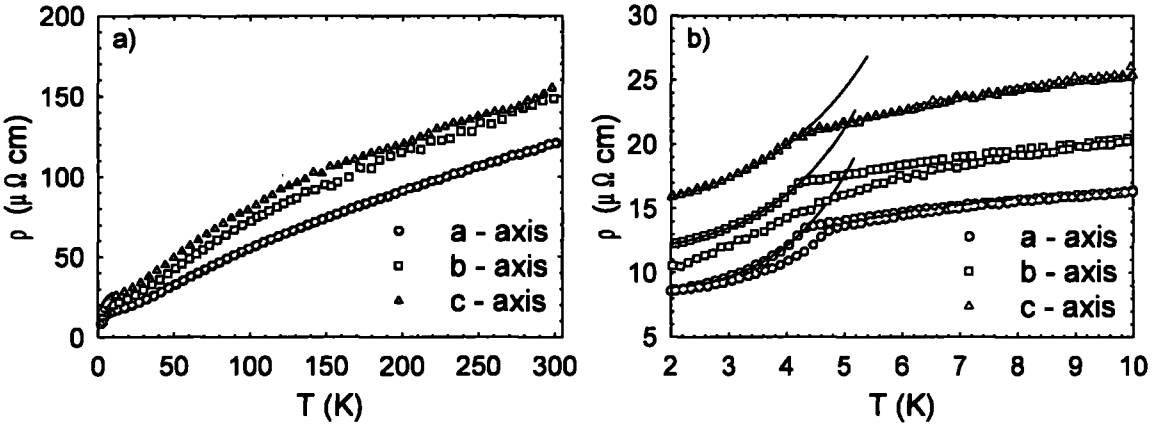

Figure 4.23: *The resistivity and longitudinal magnetoresistivity of PrPdSn. a) the temperature range 2 - 300 K; b) the low temperature detail. The lines represent the best fit of the 0 T data due to equation 4.3. The low temperature detail of PrPdSn resistivity. The opened symbols represent the data measured at zero field. The color symbols represent the resistivity measured in field B = 1 T for b-axis and B = 2 T for a- and c-axis, respectively.*

the lower one was never published before [50, 100]. This peak changes to a very broad bump at fields higher than 2 T; B || a-axis, moves to the lower temperatures and completely smears out at B = 5 T. That's why we conclude that this peak is connected with another order-to-order magnetic phase transition at T_1. As this transition is supposed to be from the antiferromagnetic phase to a different antiferromagnetic phase, the neutron diffraction experiment is highly needed to clarify the magnetic phase below T_1.

In case of Nd^{3+} ion in the monoclinic crystal field the ground state is split into 5 Krammers doublets. After subtracting the LaPdSn specific heat from the NdPdSn specific heat we have found the Schottky contribution to the magnetic part of the specific heat (Fig. 4.24b) and we were able to find four Schottky levels: 0 K (ground state), 41(3) K; 80(10) K; 110(20) K. The last doublet we were unable to calculate from our data, because its energy is probably very high and the experimental error in determining the magnetic contribution to the specific heat rapidly increases with increasing temperature. Also from the magnetic contribution to the specific heat we have calculated the magnetic entropy of the system. On the magnetic entropy we have found anomalies connected with both magnetic transitions, but also we have found that entropy at 3.6 K is much lower than $R\ln 2$ and at 80 K the magnetic entropy approaches only $R\ln 7$. One can estimate, that there is a significant amount of entropy hidden at temperatures lower than 400 mK.

The inverse susceptibility of NdPdSn compound is linear at temperatures higher than 100 K (Fig. 4.25a) for all three main crystallographic axes in which we have successfully fitted the Curie-Weiss (CW) law. The fitted coefficients for NdPdSn are Θ_P = -15.8 K;

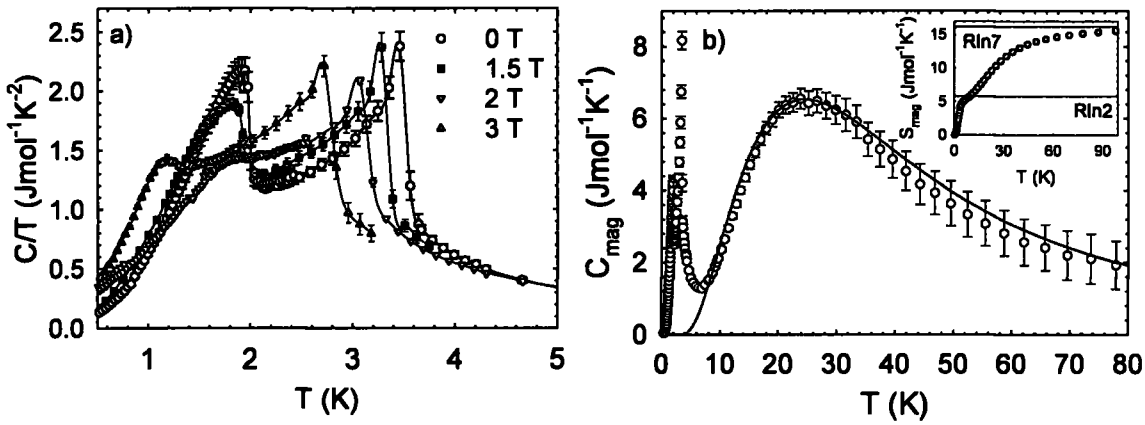

Figure 4.24: The specific heat of the NdPdSn compound: a) the low temperature detail for field applied along the a-axis b) the magnetic contribution to the specific heat. The line represent the best fit due to the Schottky contribution. In the insert the calculated magnetic entropy is emphasized.

μ_{eff} = 3.69 μ_B for the *a*-axis; Θ_P = -2.89 K; μ_{eff} = 3.68 μ_B for the *b*-axis and Θ_P = -14.8 K; μ_{eff} = 3.74 μ_B for the *c*-axis, respectively. The fitted CW constants are quite close to each other, which may suggest that there is no strong anisotropy between all three main crystallographic axes. But based on the measured magnetization curves (see next text) we believe that the similar CW constants are only a coincidence and there is strong crystal field in the sample. Also Θ_P is negative in all cases, which is expected for an antiferromagnet. The fitted effective moment is very close to the theoretical moment of Nd^{3+} ion and also close to the effective moment measured on the polycrystal sample [50]. At the low temperatures (Fig. 4.25b) we have found the anomalies on the susceptibility at temperatures close to the temperatures in which we were observed peaks on specific heat data. We have found no differences between zero field cooled and field cooled susceptibility measured at 0.01 T. At temperatures below T_N the susceptibility of NdPdSn measured along the *b*-axis still increases while the susceptibilities measured along remaining two main crystallographic axes decrease (Fig. 4.25b). The anomaly connected with T_1 is visible only on *b*- and *c*-axis susceptibility. This may be caused by the fact that T_1 is very close to the lowest temperature, which can be reached by the used apparatus (MPMS system from Quantum Design). In the higher magnetic field both transitions shift to the lower temperatures, which suggest that the magnetic transition at T_1 is from antiferromagnetic to another, different antiferromagnetic phase. The shift of the magnetic transition at T_N due to the applied field for fields lower than approximately 1.6 T is similar for all three main crystallographic axes. At higher fields the shift of T_N due to the magnetic field is more dramatic for field applied along the *c*-axis than along other two axes (see Fig. 4.26).

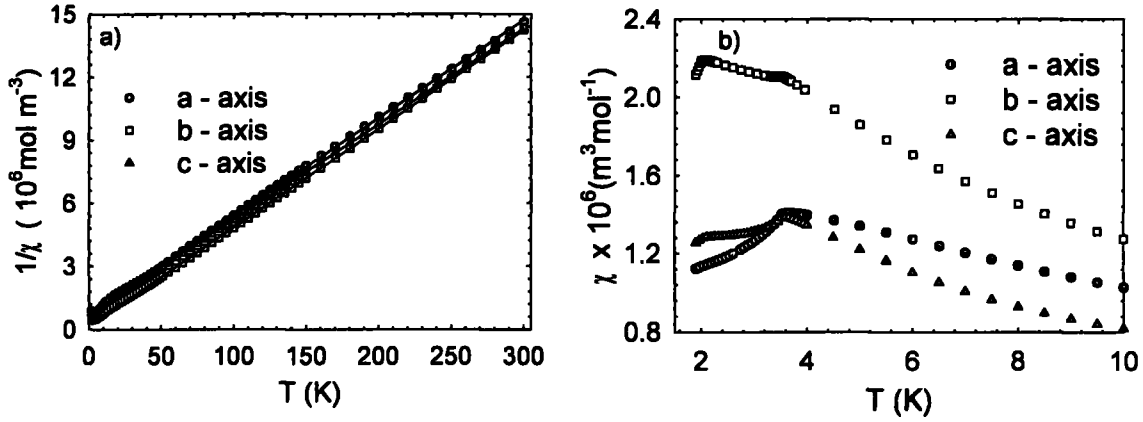

Figure 4.25: NdPdSn compound: a) the inverse susceptibility measured in B = 1 T; b) the detail of the susceptibility measured in B = 0.01 T. The lines represent the best CW fit.

	T (K)	B (T)	reached magnetic moment (μ_B)
a-axis	2	14	1.83
	10	14	1.54
b-axis	2	14	2.13
	10	14	1.89
c-axis	2	14	1.51
	2	30	1.95
	10	14	1.26

Table 4.4: The comparison of the reached magnetic moments in the applied magnetic fields along all three main crystallographic axes.

The magnetization curves (Fig. 4.27) do not saturate at magnetic fields up to 14 T for a- and b-axis, respectively and up to 30 T for the c-axis. The reached magnetic moment at the highest magnetic field is also substantially smaller than the moment of free Nd^{3+} ion (for the details see Table 4.4). Also the magnetization curves measured at 4.5 K (in the paramagnetic state) do not obey Brillouin function. In the ordered-state region we have found no anomaly on the a- and b-axis magnetization, however we have found the step-like metamagnetic transition for B || c-axis at B = 2.8(1) T and T = 2 K. The magnetization for configuration B || c-axis is linear in fields higher than 10 T. As magnetization curves are far from the saturation and are completely different for all three main crystallographic axes we have conclude that the magnetocrystalline anisotropy in the NdPdSn is high.

The resistivity exhibit a metallic behavior at temperatures higher than 10 K, but at low temperatures (Fig. 4.28) the resistivity exhibits a local minimum for a- (at 3.4 K) and

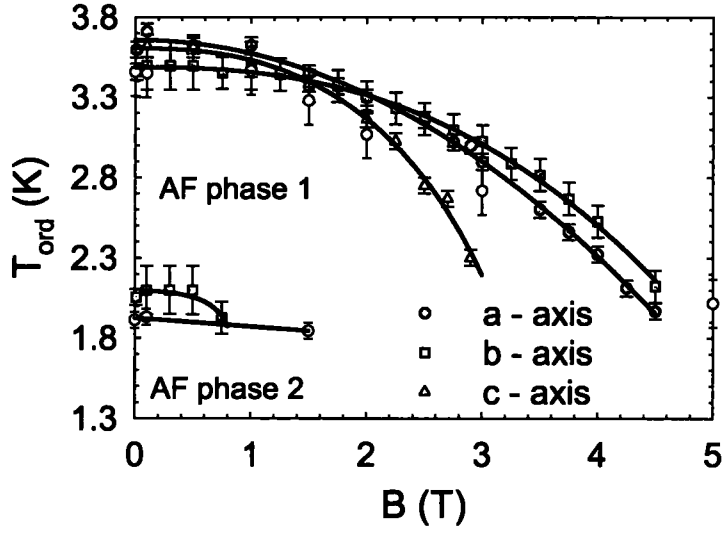

Figure 4.26: *The phase diagram of NdPdSn. The open symbols are obtained using the specific heat measurements; the color symbols are obtained using magnetization measurements.*

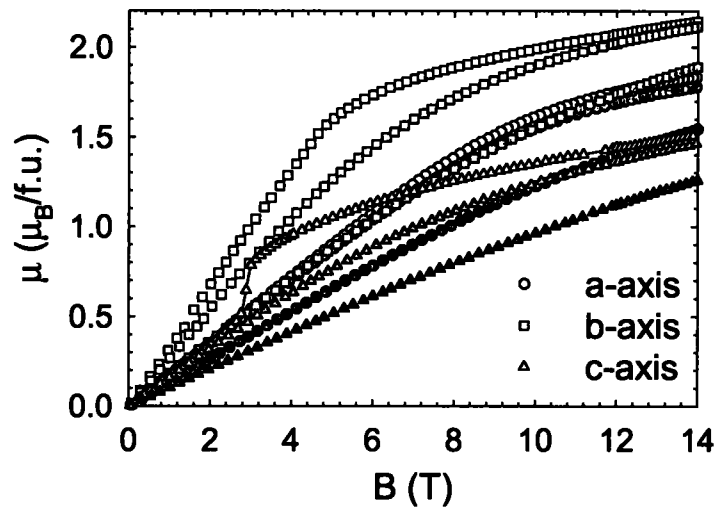

Figure 4.27: *The magnetization curves of the NdPdSn compound measured along all three main crystallographic axes. To simplify the figure we have chosen only data for $T = 2$ (opened symbols), 5 (pale symbols) and 10 K (dark symbols). As the magnetization curve for $B \parallel$ c-axis from the 30 T shot is linear at fields higher than 10 T we didn't include this curve in the figure.*

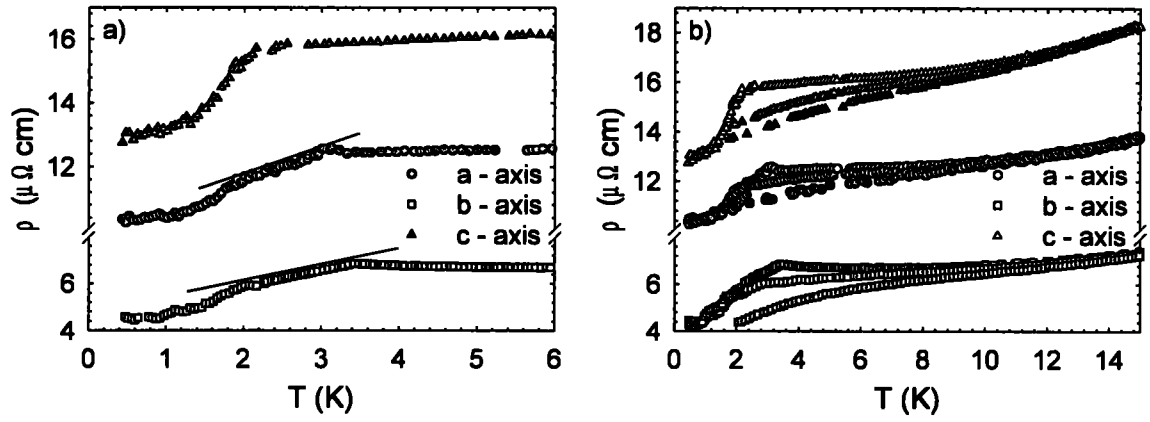

Figure 4.28: *The resistivity of NdPdSn compound: a) the low temperature detail. The lines are only guides for the eye. b) the longitudinal magnetoresistivity. To simplify the figure we have chosen only data for B = 0, 3 and 5 T.*

for *b*-axis (at 6.2 K), respectively. The paramagnetic-antiferromagnetic transition at T_N is clearly visible for *a*- and *b*-axis resistivity as a maximum in the ρ(T) curve. However, on the *c*-axis resistivity we have observed only a broad knee at T_N and then decrease of the resistivity. The transition at T_1 is also clearly visible only for the *a*- and *b*-axis resistivity as a change of slope of the resistivity. We have found no anomaly at the *c*-axis resistivity at T_1. The resistivity in temperature region between T_1 and T_N decreases linearly for current applied along *a*- and *b*-axis. At temperatures below T_1 the resistivity again decreases. We have tried to fit this region due to Andersen's model, but we haven't obtained satisfactory fit. Also the noise in the resistivity data measured below T_1 do not allow us to obtain more information from this resistivity data. After measuring the longitudinal magnetoresistivity we have found the decrease of the resistivity with applied magnetic field for all three main crystallographic axes (Fig. 4.28b). We have also observed the shift of T_N to the lower temperatures for *a*- and *b*-axis, respectively and completely smearing out the anomalies connected with T_N in magnetic field of 5 T. From the *c*-axis resistivity data we were unable to judge if the knee in the resistivity connected with T_N shifts to lower temperatures.

4.2 RET2X2 compounds

4.2.1 Introduction

Crystal structure

The RET_2X_2 compounds (RE = La – Yb; T = d-metal and X = p-metal) mostly crystallize in an ordered variants of the tetragonal $BaAl_4$ crystal structure - $CaBe_2Ge_2$-type or $ThCr_2Si_2$-type crystal structure or in the hexagonal $CeAl_2Si_2$ crystal structure [42]. For the complete summary of the crystallographic data for all three crystal structures see appendix B.1. In this work we have studied only the compounds which crystallize in the $ThCr_2Si_2$ and $CaBe_2Ge_2$-type crystal structure.

The $ThCr_2Si_2$-type crystal structure (space group I4/mmm) is presented on the Fig. 4.29a. This structure is layered with stacking layers consisting only from one element. These layers are stacked along the c-axis with a stacking sequence RE–X–T–X–RE–X–T–X–RE. In this structure RE occupy the 2(a) crystallographic position and the local crystal field in the RE position is tetragonal. The compounds which crystallize in this crystal structure are for example RCr_2Si_2 (R = Sm, Gd – Lu) series [106] or RNi_2Si_2 (R = Gd –Tm) series [107].

The $CaBe_2Ge_2$-type crystal structure (space group P4/nmm) differ from the $ThCr_2Si_2$-type crystal structure only by the different stacking sequence of the layers: RE–T–X–T–RE–X–T–X–RE. In this case the RE atom occupies the 2(c) crystallographic position and the local crystal field at the position of RE atom is again tetragonal. The sketch of the structure is plotted on Fig. 4.29b. The examples of the compounds which crystallize in this crystal structure can be RPt_2Si_2 (R = La – Nd; Sm; Gd – Yb) series [108].

Our studied $REIr_2Si_2$ (RE = La, Ce and Pr) adopt both $CaBe_2Ge_2$ structure at higher temperatures (HT phase) and undergoes the change of the structure to the $ThCr_2Si_2$-type structure at lower temperatures (LT phase). The HT phase can be stabilized even at the low temperatures by rapidly cooling down from the melt to the room temperature. However by subsequent annealing of the HT phase the samples completely transform to the LT phase, which makes HT phase highly unstable at low temperatures. The crystallographic parameters for $REIr_2Si_2$ compounds are summarized in Table 4.5. The crystallographic phase transition is not connected with the changing of the volume, but the c/a ration in all cases changes of several % and also the distances between nearest-neighbours and next-nearest-neighbours of RE atom changes, which has crucial impact to the magnetism in these compounds. All previously mentioned remarks to the crystallography in $REIr_2Si_2$ compounds makes them quite unique in the family of RET_2X_2 compounds.

Physical properties

$LaIr_2Si_2$ compound was already studied from the point of the polymorphism in this compound [109]. It was referred that the HT phase can be obtained by quenching from the temperature above 1720 °C. The HT phase was found to be superconducting with the

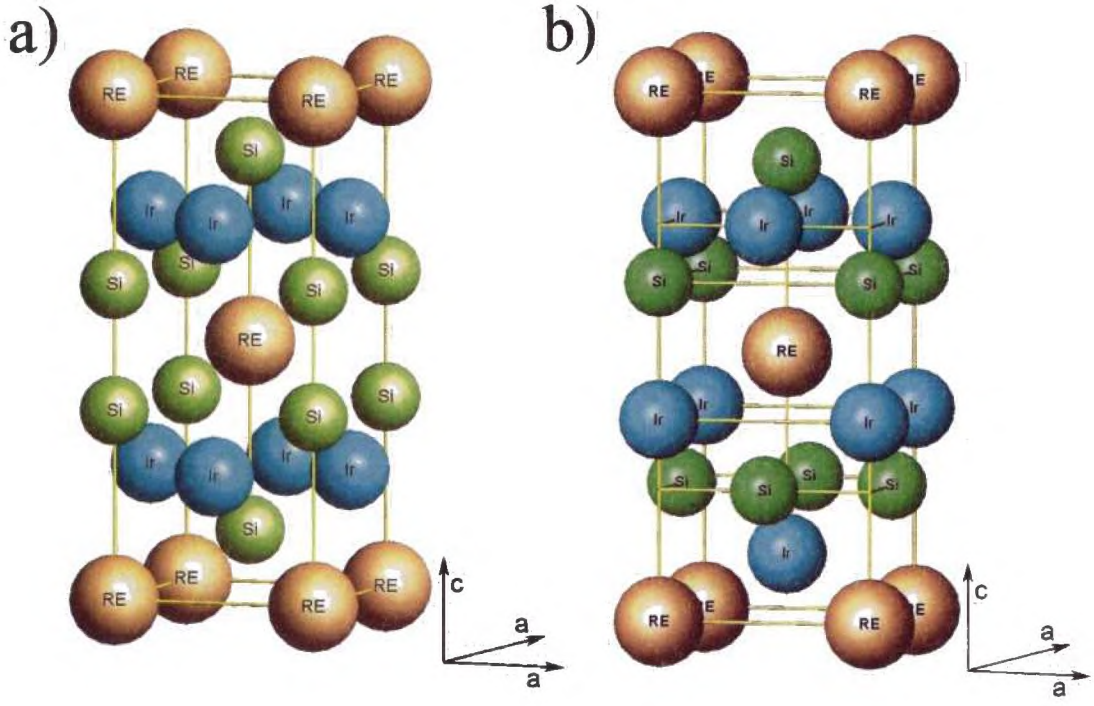

Figure 4.29: *The tetragonal crystal structures of RET_2X_2 compounds: a) $ThCr_2Si_2$-type crystal structure; b) $CaBe_2Ge_2$-type crystal structure.*

compound	phase	a(nm)	c(nm)	c/a	V (nm^3)	ref.
$LaIr_2Si_2$	ht	0.4191(1)	0.9944(4)	2.373(1)	0.1747	[109]
	lt	0.4109(1)	1.0299(3)	2.506(1)	0.1739	[109]
	ht	0.4187(3)	0.9941(2)	2.374	0.1743	this work
	lt	0.4108(1)	1.0297(2)	2.507	0.1738	this work
$CeIr_2Si_2$	ht	0.41460(5)	0.9855(2)	2.3770	0.1694	[110]
	lt	0.40882(2)	1.01696(6)	2.4875	0.1700	[110]
	ht	0.4144(2)	0.9850(1)	2.3769	0.1691	this work
	lt	0.4084(2)	1.0153(3)	2.4860	0.1693	this work
$PrIr_2Si_2$	ht	-	-	-	-	-
	lt	0.4087(1)	1.0154(2)	2.484(3)	0.1696	[111]
	ht	0.4152(2)	0.9847(3)	2.3716	0.1698	this work
	lt	0.4084(2)	1.0145(2)	2.4841	0.1692	this work

Table 4.5: *The comparison of HT $CaBe_2Ge_2$-type crystallographic modification and LT $ThCr_2Si_2$-type crystallographic modifications for $REIr_2Si_2$ compounds.*

critical temperature of 1.6 K, while the LT phase was found to behave as a normal metal down to 1 K [109].

In the case of $CeIr_2Si_2$ Hiebl et. al [112] refers very interesting study of the susceptibility of the polycrystalline sample measured up to 1000 °C. The most interesting part of this study is the kink on the HT $CeIr_2Si_2$ susceptibility at 550 °C. As this susceptibility was measured on the HT sample during increasing temperature, this kink represents the onset of the phase transformation from the HT to the LT phase. At temperatures higher than 550 °C the susceptibility of both samples fits together which is caused by the transformation of HT phase to the LT phase. The inverse susceptibility of HT phase exhibits the local minimum below 700 K, which is commonly observed phenomenon for the mixed valence systems while the LT modification obeys Curie-Weiss law for temperatures above 200 K [112].

In the literature we have found the only one study of the $PrIr_2Si_2$ compound, which was done on the polycrystalline samples and only on the LT phase [111]. This phase was found to order antiferromagnetically at $T_N = 47(1)$ K. It also undergoes another order-to-order magnetic phase transition at $T_t = 25(2)$ K. Above 100 K this phase of $PrIr_2Si_2$ compound obeys the Curie-Weiss law with parameters Θ_P = -6(2) K; $\mu_{eff} = 3.7(1)\ \mu_B$/moll [111].

4.2.2 LaIr2Si2

In the case of the $LaIr_2Si_2$ we have prepared the polycrystalline sample for the comparative analysis of the specific heat by arc-melting. By this arc-melting we were able to prepare HT phase of this compound and by subsequent annealing of the sample[3] we were able to obtain LT crystallographic phase. The crystallographic parameters for both phases are summarized in Table 4.5. As a next step we have measured the specific heat of the both phases (see Fig. 4.30) and we have found no anomalies at the specific heat of the both phases at temperatures higher than 2 K, so we have used it as an nonmagnetic analogue to $CeIr_2Si_2$ compound and $PrIr_2Si_2$ compound.

4.2.3 CeIr2Si2

$CeIr_2Si_2$ single crystal was grown in the tri-arc furnace in Prague from the stoichiometric melt of the high purity[4] elements. The crystal was grown using the rotation of seed of 12 rpm and pulling speed as high as 14 mm/h. After the growing we have checked the grown rod by Laue pattern and we have found a good single crystal of tetragonal symmetry. When we have pulverized part of the grown ingot, we have found that we have grown the HT crystallographic modification of $CeIr_2Si_2$. Also we have annealed the part of grown single crystal at 900 °C for 12 hours and then slowly cooled down. After this procedure, we

[3]For the annealing we wrapped the sample into tantalum foil and sealed it into quartz tube under the argon atmosphere. We have annealed the sample at 1000 °C for 12 hours.

[4]The purity of the elements was at least 3N

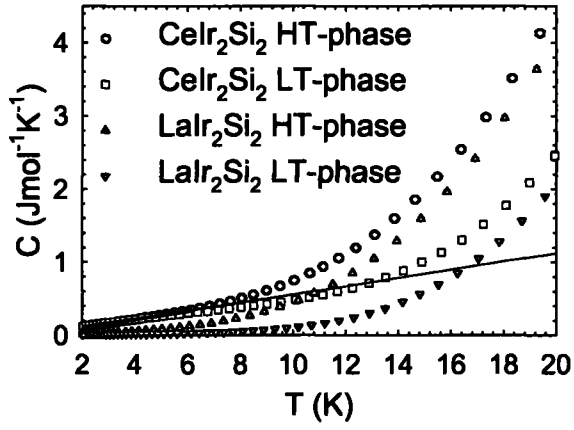

Figure 4.30: The low temperature detail of $CeIr_2Si_2$ specific heat compared with corresponding $LaIr_2Si_2$ nonmagnetic analogue. The line represent the best linear fit of the HT phase.

have observed that the sample already completely recrystallized to the LT crystallographic phase, which is more stable at the room temperature than the HT phase. The measured crystallographic parameters for both phases compared with those obtained from literature are summarized in Table 4.5. Also we have observed, that the easy-cleaving plane for both, HT and LT crystallographic modifications is perpendicular to the c-axis.

Above 25 K the specific heat of $CeIr_2Si_2$ fits very well to its La-based analogue (see Fig. 4.30). So the phonon contribution to the specific heat is similar in the both compounds. At lower temperatures the specific heat of $CeIr_2Si_2$ is higher than its La-based analogue. The specific heat of HT phase of Ce-based compound is linear up to 6 K (Fig. 4.30). Such a behavior was already observed for an interconfiguration-fluctuation compound YbB_4 [113]. The coefficients of the linear fit of the HT phase specific heat are $A = -4(1)$ mJmol^{-1}K^{-1} and $B = 56.2(4)$ mJmol^{-1}K^{-2}. In the case of LT phase we have observed different scenario: we have observed the broad bump which occurs below 5 K. The origin of this bump is yet unknown.

We have measured the susceptibility of $CeIr_2Si_2$ of both HT and LT phases in the temperature range 2 – 300 K and in the magnetic fields of 1, 3 and 5 T applied along both main crystallographic axes (Fig. 4.31a). We have performed this experiment in MPMS (Quantum Design) apparatus [30] and we have always measured during heating the sample. The cooling down we have performed in the zero magnetic field. We have found no difference between 3 and 5 T susceptibility but as the signals were quite weak, we have corrected the low temperature susceptibility data due to the possible ferromagnetic impurity according to the equation 3.30. Also we have made high temperature experiment (Fig. 4.31b). In this experiment we have used the vibrating sample magnetometer with the "oven" option installed inside the PPMS apparatus. In this experiment we have started to

axis	run	temperature range (K)	Θ_P (K)	$\mu_{eff}(\mu_B)$
a-axis	1st decreasing temperature	350 – 900	-480(10)	3.2(1)
c-axis	2nd increasing temperature	310 – 700	-60(1)	2.62(5)
c-axis	2nd increasing temperature	750 – 1000	-240(10)	2.91(3)
c-axis	2nd decreasing temperature	310 – 700	-40(1)	2.59(5)
c-axis	2nd decreasing temperature	750 – 1000	-250(10)	2.92(3)

Table 4.6: *The comparison of the Curie-Weiss constants for the susceptibility of $CeIr_2Si_2$ measured at temperature range 310 – 1000 °C.*

measure the magnetic susceptibility during increasing temperature (rate 3 K/min; B = 1 T) up to 1000 K, than measured M(B) curve at 1000 K and then measured susceptibility during the decreasing temperature.

The inverse susceptibility of this compound (Fig. 4.31) exhibit no magnetic phase transition in temperatures lower than 1000 K for the LT phase and below 300 K for the HT phase. This result is consistent with the previously measured susceptibility on the polycrystalline samples [112]. In the case of the high temperature experiment for configuration B || a-axis we have started from the HT phase. But during the first heating to 1000 K we did not obtain good quality data. While measuring the $1/\chi(T)$ curve during decreasing temperature from 1000 K we have found that $1/\chi(T)$ is linear in temperature range 350 – 950 K. The deviation from the linearity at temperatures above 950 K is probably the apparatus effect. After this experiment we have pulverized this sample and measured the X-ray powder diffraction on it. The analyzing of the X-ray powder pattern unambiguously leads to the crystallographic parameters of a LT phase. From this we can conclude that the temperatures between 300 and 1000 K are high enough to recrystallize the unstable HT phase to the more stable LT phase, but as we have found no anomaly on the $\chi(T)$ curve during the decreasing of the temperature, we think that temperature T = 1000 K is not high enough for the phase transformation from the LT phase to the HT phase. In the case of high temperature experiment for B || c-axis we have again started from the HT phase, but during the first scan to 1000 K we didn't measure. Then, during the second run to 1000 K we have measured during increasing temperature and again during the decreasing temperature. In this experiment both curves fit together very well. So we think, that during the second run the sample was again already completely recrystallized to the LT phase. The $1/\chi(T)$ curve for B || c-axis is linear in temperature range 310 – 700 K, then passes through broad knee and then is again linear at temperature range 750 – 1000 K, but with different slope. The comparison of all coefficients assuming, that the compound obeys Curie Weiss law in all temperature regions in which $1/\chi(T)$ is linear is summarized in table 4.6.

At temperatures lower than 300 K the $1/\chi(T)$ curve increases with decreasing temperature for the field applied along the both main crystallographic axes of the HT phase,

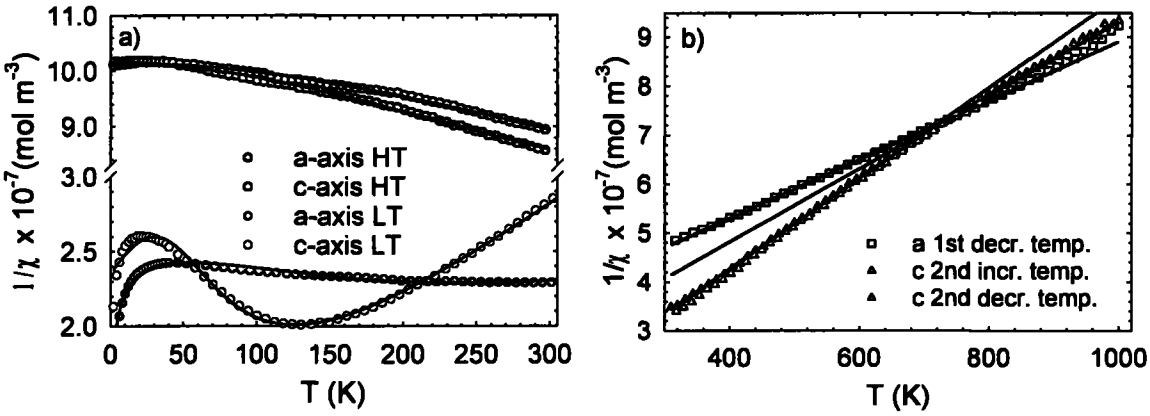

Figure 4.31: The susceptibility of $CeIr_2Si_2$ a) the data measured below 300 K b) data measured in the temperature range 300 - 1000 K. The lines represent the best fit due to the equations described in text.

passing through the local maximum around around 30 K and again decreases. On the other hand in case of LT phase the $1/\chi(T)$ decreases with decreasing temperature almost linearly, passing through the local minimum at 130 K (for c-axis) and then going through the local maximum at 20 K for c-axis and ending with the low-temperature tail similarly to the HT phase inverse susceptibility. The similar, but less-pronounced effects we have also observed for the field applied along the a-axis. The $1/\chi(T)$ curve for the LT phase has some similarities to curves already published on the CeRhIn and $Ce_2Ni_3Si_5$ compound [55, 114]. That's why we have also assumed, that in this phase Ce ions are in two configurations: Ce^{3+} and Ce^{4+}. One of the possibilities how to understand the behavior of the LT magnetic susceptibility is the ionic two-level interconfiguration fluctuation model[5] proposed by Sales and Wohlleben [115]. According to the later modifications made by Franz et al. [116] we can use for the effective temperature equation:

$$T^{+} = \sqrt{T^2 + T_f^2} \tag{4.4}$$

where T_f is the temperature of the spin fluctuations. Then using the Curie-Weiss law for describing the susceptibility of Ce^{3+} ions and using a term χ_0 as a temperature independent diamagnetic background we can write:

$$\chi(T) = (1-n)\left(\frac{\mu P(T)}{T^{+}}\right) + n\frac{C}{T-\theta_p} + \chi_0 \tag{4.5}$$

[5]the basic idea of the model is that the rare earth ion fluctuates in time between two configurations and each configuration is characterized by a different integral occupation of $4f$ shell

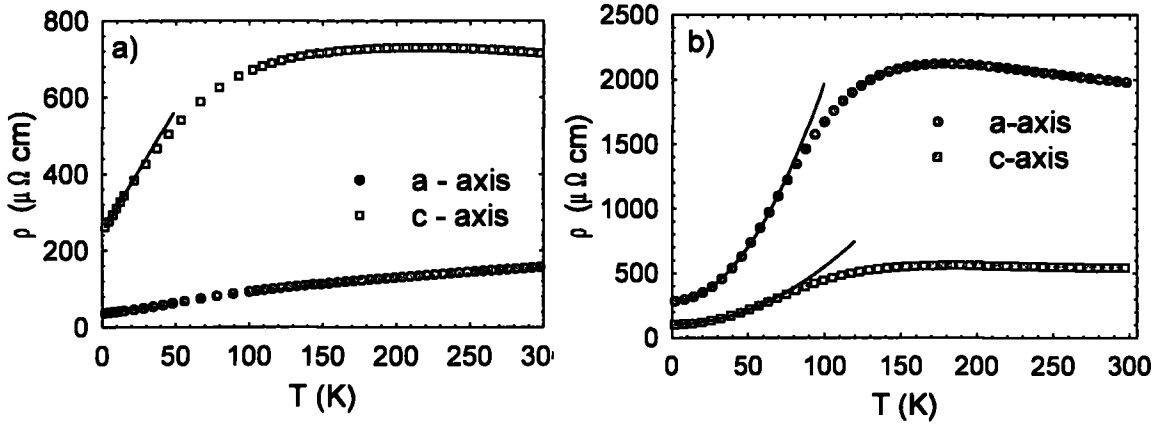

Figure 4.32: The resistivity of $CeIr_2Si_2$: a) the HT phase; b) the LT phase. The lines represent the best fit as described in text.

with

$$P(T) = \frac{2J+1}{2J+1+exp(-E_{ex}/k_BT^{+})} \tag{4.6}$$

where T_f is the spin-fluctuation temperature, n gives the fraction of Ce ions, which are in the interconfiguration state and in normal Ce^{3+} state, J is the total angular momentum, μ is the effective moment of Ce^{3+} ion and E_{ex} is the excitation energy between the interconfiguration states. The case $E_{ex} < 0$ correspond to the situation in which the magnetic $4f^1$ configuration lies energetically higher than $4f^0$ configuration and vice-versa. In equations 4.5 and 4.6 we have already assumed the total angular momentum and the effective moment of Ce^{4+} ion to be 0. The parameters, which we have obtained from the fitting of the LT phase due to equation 4.5 are for the a-axis $n = 2 \times 10^{-5}$, E_{ex} = -590 K; T_f = 192 K, C = 0.002 m^3mol^{-1}; θ_p = -2 K; $\chi_0 = -2.79 \times 10^{-8}$ m^3mol^{-1} and for the c-axis n = 0.001, E_{ex} = -309 K; T_f = 51 K, C = 0.04 m^3mol^{-1}; θ_p = -154 K; $\chi_0 = -1.4 \times 10^{-9}$ m^3mol^{-1}. The coefficient n suggests, that the main contribution to the fit is from the first term (spin fluctuating term) in the equation 4.5, hence the Curie-Weiss parameters are burdened with high error. On the other hand we have demonstrated, that the susceptibility of LT phase of $CeIr_2Si_2$ can be described in terms of interconfiguration model proposed by Sales and Wohlleben [115]. The negative χ_0 in the fit suggests that there is added some diamagnetic contribution to the whole susceptibility. This contribution may originate from the sample holder, so it is the effect from the an apparatus.

When we have fixed $n \equiv 0$ in equation 4.5 we were also be able to fit the susceptibility of the HT phase. In this case we have found parameters $\chi_0 = 9.8(1) \times 10^{-9}$ m^3mol^{-1}; E_{ex} = -2190(10) K and T_f = 250(5) K for the a-axis and $\chi_0 = 8.6(1) \times 10^{-9}$ m^3mol^{-1}; E_{ex} = -1810(10) K and T_f = 380(7) K for the c-axis.

Figure 4.32 demonstrates the measured resistivity of $CeIr_2Si_2$ compound. In the case of the HT phase we have found the broad bump at the c-axis resistivity at approximately 200 K. Such a bumps on the resistivity can be found for the many of the Ce-based intermetallic compounds [93, 117]. In the case of the a-axis resistivity we have found only the monotonous decrease of the resistivity during the decreasing temperature. Also the a-axis resistivity is approximately 5 times lower than the c-axis resistivity. The residual resistivity ratio for this phase is only 4.3 for the a-axis and 2.7 for the c-axis resistivity, respectvely.

At temperatures below 15 K the resistivity of the HT phase can be fitted by the equation:

$$\rho = \rho_0 + AT \tag{4.7}$$

with the coefficients $\rho_0 = 36.1(1)\mu\Omega$cm and $a = 0.44(2)$ $\mu\Omega$cmK^{-1} for the a-axis and $\rho_0 = 247(2)\mu\Omega$cm and $a = 6.4(1)$ $\mu\Omega$cmK^{-1} for the c-axis resistivity, respectively. This suggests that this phase doesn't behave like the normal Fermi-liquid compound.

In the case of the LT sample we have again observed the bump on the c-axis resistivity at approximately the same temperatures as in the case of the HT phase and well-pronounced maximum at around 170 K for the a-axis resistivity. Also the a-axis resistivity of the LT phase is much higher than the a-axis resistivity of the HT phase. At temperatures lower than 65 K the resistivity of the LT phase can be fitted by the equation $\rho = \rho_0 + aT^2$. The coefficients obtained from this fit are $\rho_0 = 280(2)\mu\Omega$cm; $a = 0.17(3)\mu\Omega$cmK^{-2} for the a-axis and $\rho_0 = 103(1)\mu\Omega$cm; $a = 0.045(1)\mu\Omega$cmK^{-2} for the c-axis, respectively. The existence of the cubic law for the p(T) data of the LT phase suggests that this phase behaves as Fermi-liquid compound.

We have measured also the transversal magnetoresistivity of the both, HT and LT phase in the configuration i || a; B || c and in the experimental configuration i || c; B || a. Within the experimental error, we have found zero magnetoresistivity in all measurements except of the magnetoresistivity of HT sample measured at 250 K with electric current applied along the c-axis. For this configuration we have found that the resistivity decreased of aproximately 0.1 % at magnetic field of 9 T.

To conclude the results obtained on the $CeIr_2Si_2$ compound we suppose that this compound is just at the border between non-Fermi-liquid and Fermi-liquid compounds and the side of the border is chosen by the crystal structure of the compound and by the c/a ratio in the crystal structure.

4.2.4 PrIr2Si2

$PrIr_2Si_2$ single crystal was grown in the tri-arc furnace in Prague from the stoichiometric melt of the high purity[6] elements. The parameters of the growing were the same as in the case of $CeIr_2Si_2$. The pulled rod has a tendency to break after approximately 25 mm of length of grown ingot. This we have ascribed to the onset of the crystallographic phase transformation from the HT to LT phase. After the growing we have checked the grown

[6]The purity of the elements was at least 3N

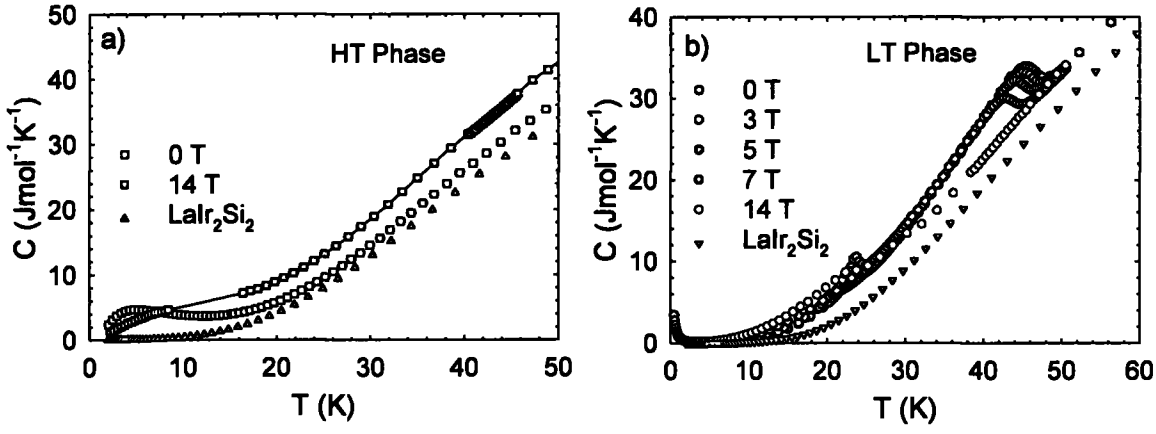

Figure 4.33: *The specific heat of $PrIr_2Si_2$ measured in fields applied parallel to the c-axis compared with the specific heat of $LaIr_2Si_2$: a) HT phase; b) LT phase.*

rod by Laue pattern and X-ray powder diffraction and we have found a good single crystal of the HT crystallographic modification. Also we have annealed the part of grown single crystal at 900 °C for 12 hours and we have observed that the sample already completely recrystallized to the LT crystallographic phase. From this we can conclude that the HT phase of this material is highly unstable at room temperatures and by short annealing this phase can recrystallize to the LT crystallographic phase. Also we have observed, that the easy-cleaving plane for both, HT and LT crystallographic modifications is perpendicular to the c-axis. When we have compared crystallographic data of HT and LT phase (see Table 4.5) we have found that the volume of the unit cell is the same for both phases. On the other hand the c/a ratio is different for both phases, which resulted to very brittle samples of the LT phase.

The specific heat of both, HT and LT phase of $PrIr_2Si_2$ measured at temperatures higher than 50 K was found with no anomaly. This specific heat is quite close to the specific heat of $LaIr_2Si_2$. Below 50 K we have found the bump at the specific heat of the HT phase with the maximum at 5 K (Fig. 4.33a). This bump shifts to the higher temperatures and smears out with applied magnetic field along the c-axis. We have assigned this bump to the Schottky contribution to the specific heat.

The different case is the LT Phase of the $PrIr_2Si_2$ (Fig. 4.33b). For this crystallographic modification we have found two clearly visible peaks on the specific heat: at $T_N = 45.5(1)$ K and at $T_t = 23.7(2)$ K. These transition temperatures are of about 1.5 K lower than the transition temperatures already published for this crystallographic modification by Welter et. al. [111]. The T_t shifts from 23.7(2) K at B = 0 T to 20.7(4) K at B = 5 T; B || c and then disappears at higher fields. The peak connected with T_N shifts monotonously from the 45.5(1) K at zero magnetic field to 42.9(4) K at B = 7 T; B || c. Another increasing of

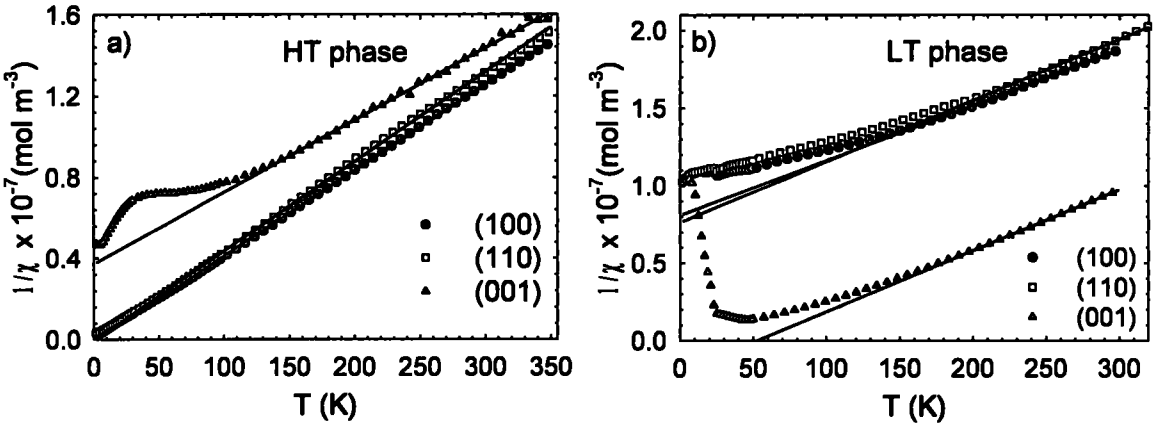

Figure 4.34: The inverse susceptibility of $PrIr_2Si_2$: a) HT phase measured at B = 1 T; b) LT phase measured at B = 3 T. The lines represent the best CW fit.

	HT phase			LT phase		
cryst. direction	fit range(K)	Θ_p (K)	$\mu_{eff}(\mu_B)$	fit range(K)	Θ_p (K)	$\mu_{eff}(\mu_B)$
(100)	50 – 350	2.88	3.88	150 – 300	-228	4.23
(110)	50 – 350	1.43	3.79	200 – 320	-194	4.02
(001)	150 – 350	-105	4.23	200 – 300	52.5	4.02

Table 4.7: The results from the fitting of the inverse susceptibility of $PrIr_2Si_2$ according to CW law.

magnetic field shifts this transition to 22.3(7) K at field B = 14 T; B || *c*. The increase of the specific heat at temperatures below 4 K is connected to the Schottky contribution to the specific heat.

The inverse susceptibility of both, HT and LT phase, is plotted in Fig. 4.34. In the both cases we have found only very small anisotropy in the basal plane. In the case of HT phase we have found no peaks in $1/\chi(T)$ curve and we have found that the inverse susceptibility obeys the CW law in a wide temperature range. The details of the fitting the susceptibility using the CW law are summarized in Table 4.7. The only anomaly which we have observed on the $1/\chi(T)$ curve of HT phase was found in configuration B || *c* at temperatures below 100 K. This anomaly was ascribed to the crystal field in this phase. Also the fitted effective moments for the HT phase are slightly higher than theoretical moment for Pr^{3+} ion for measurements done in basal plane and significantly higher in case of B || *c*. This may be also caused by crystal field effect. In the case of LT phase the $1/\chi(T)$ curve is more or less linear only at temperatures higher than 150 K. This is consequence of the strong crystal field in this compound. That is why also the parameters obtained from the CW fitting

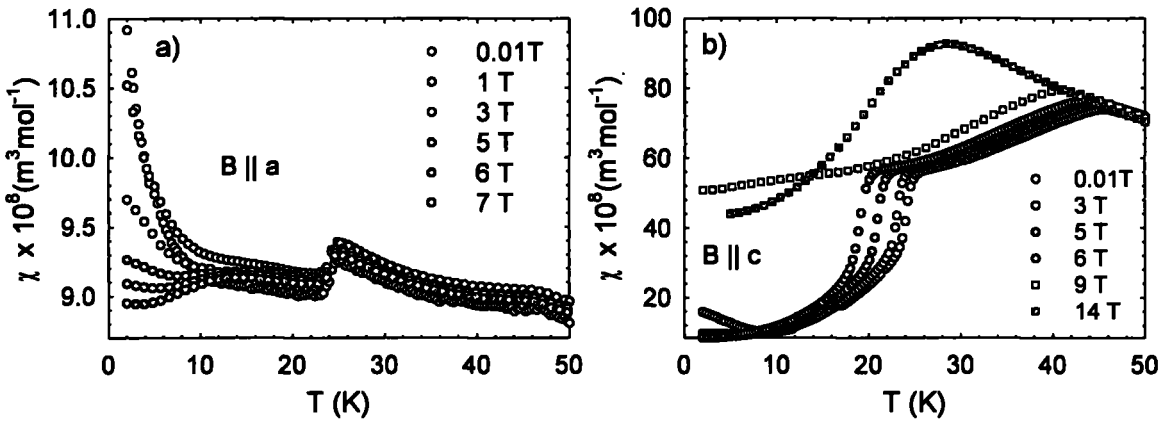

Figure 4.35: *The low temperature detail of $\chi(T)$ curve of the LT phase: a) B || a; b) B || c.*

(Table 4.7) are so different for all three measured crystallographic directions and also the effective moment is much higher than the theoretical moment of Pr^{3+} ion.

At temperatures lower than 50 K we have found two distinct anomalies on the $\chi(T)$ curves of LT phase (see Fig. 4.35). Both anomalies occur at the same temperatures as the anomalies in the specific heat, so we have ascribed these anomalies to T_N and T_t. Beside these two anomalies we have also found the increase of the susceptibility at temperatures lower than 10 K for both orientations of magnetic field. This increase can be suppressed by the applied magnetic field and probably has the same origin as the the low-temperature anomaly in the specific heat (Fig. 4.33b). In the case of B || a the anomalies connected with T_t and T_N are intact to the applied magnetic field. Also the susceptibility measured for this configuration is much lower than the susceptibility measured for the configuration B || c-axis. In the case of B || c the transition connected with T_N shifts monotonously to the lower temperatures which is supposed for the paramagnetic-antiferromagnetic phase transition. Also the anomaly connected with T_t shifts to the lower temperatures but this anomaly completely vanishes in magnetic fields higher than 6 T.

The magnetization curves measured on the HT phase (Fig. 4.36a) again confirmed very small anisotropy in the basal plane. These curves also clearly demonstrate that the moment in HT phase lies in the basal plane and c-axis is a hard magnetization direction. Also we have successfully fitted all magnetization curves of HT phase by the Brillouin function. In the case of magnetic field applied along (100) direction we have found M_{sat} = 2.67(1) μ_B/f.u.; 2.92(1) μ_B/f.u. and 3.15(2) μ_B/f.u. at 10 K; 20 K and 35 K, respectively. In the case of field applied along (110) direction we have found M_{sat} = 2.94(1) μ_B/f.u.; 3.05(1) μ_B/f.u. and 3.26(2) μ_B/f.u. at 10 K; 20 K and 35 K, respectively. In the case of magnetic field oriented along the (001) direction we had to release in addition to M_{sat}

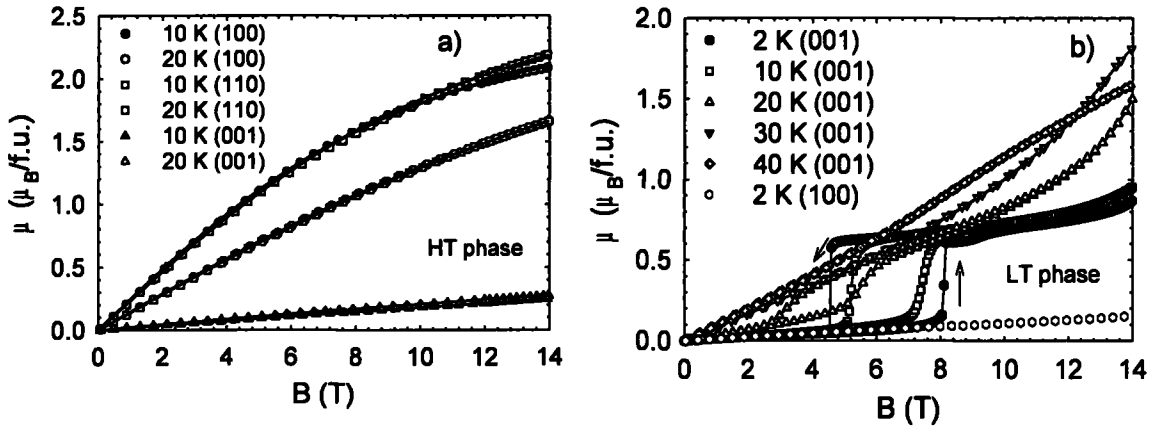

Figure 4.36: The magnetization of $PrIr_2Si_2$ measured in different crystallographic directions and at different temperatures: a) HT phase; the lines represent the best fit due to Brillouin function. b) LT phase; the lines are guides for the eye.

also the temperature of the system to obtain the reasonable fit. This fitted temperature was of about 20 K to 40 K higher than the real temperature measured in the experiment. Nevertheless we have again found saturated magnetization $M_{sat} = 0.61(1)\ \mu_B$/f.u.; 0.90(1) μ_B/f.u. and 1.48(6) μ_B/f.u. at 10 K; 20 K and 35 K, respectively. All results obtained from M(B) curves together with the results obtained from the $\chi(T)$ curves suggests that there the magnetic moment in the HT crystallographic phase of $PrIr_2Si_2$ lies in the basal plane.

The magnetization curves measured on the LT phase (4.36b) exhibit a completely different behavior. First of all in this case the magnetic moments are somehow aligned along the c-axis and this axis became the easy-magnetization axis. The magnetization curves measured in configuration B || a-axis are linear up to 14 T in all measured temperatures. But the magnetization curves measured in configuration B || c-axis exhibit a metamagnetic transition with onset at 8.1 T and with hysteresis of 3.5 T at 2 K. This metamagnetic transition shifts to the lower fields and the hysteresis decreases at higher temperatures than 2 K. This clearly suggests that the magnetic phase below T_t in zero field is an antiferromagnetic phase, which can be destabilized by the magnetic field applied along the c-axis. The metamagnetic transition completely vanishes at temperatures higher than 20 K, which points that this metamagnetic transition is directly connected to the magnetic phase below T_t.

Closer look at the magnetization curves of the LT phase (Fig. 4.36b) at fields higher than 12 T and temperatures lower than 20 K revealed additional upturn of the magnetization, which suggest that something more happen at the magnetic fields higher than 14 T. That's why we have performed a high field experiment on the 50 T pulsed magnet in the

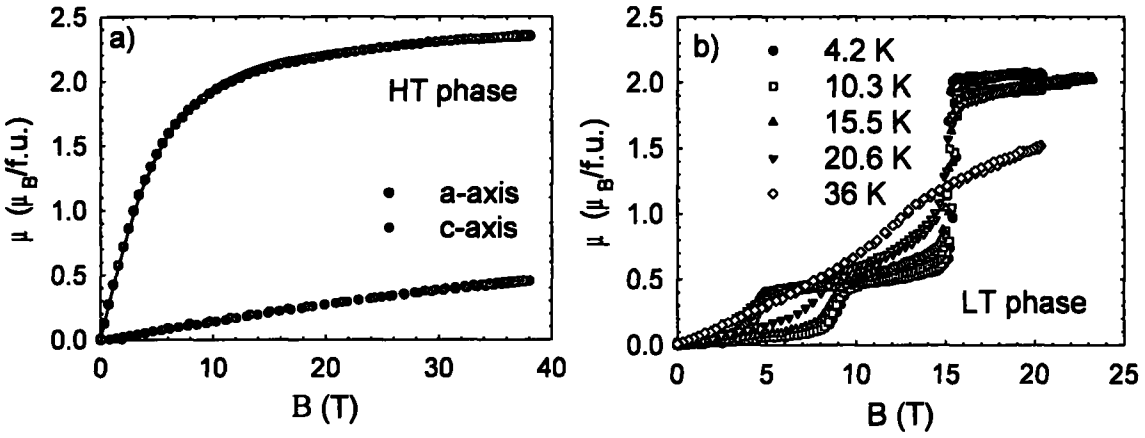

Figure 4.37: The magnetization measured on high field pulsed magnet in Dresden: a) HT phase measured along both main crystallographic axes at temperature T = 4.2 K. The line represent the best fit due to Brillouin function; b) The two-phased sample consisted of 76.7 % of LT phase and 23.3 % of HT phase. In this case the magnetic field was parallel to the c-axis.

Laboratory for pulsed magnetic fields, Leibnitz Institute for Solid State and Materials Research, Dresden, Germany. For this experiment we have used the high quality sample of the HT phase oriented along both main crystallographic axes and one sample with orientation B || c, which was by the accident two-phased. This sample we have pulverized after the experiment, made X-ray powder diffraction and determined that the sample consisted of 76.7 % of LT phase and 23.3 % of HT phase. The results of the high field experiment are plotted on Figure 4.37. The high field magnetization curves of HT phase show no anomally up to 40 T: a-axis magnetization curve can be fitted by the Brillouin function in the whole field range with $M_{sat} = 2.33\mu_B$/f.u. and the c-axis magnetization curve is almost linear in fields up to 40 T. In the case of the mixed-phase sample and field applied parallel to the c-axis we have found another metamagnetic transition at 15.5(2) T with hysteresis of approximately 0.5 T. The critical field for this second transition is temperature independent for temperatures below T_t. At fields higher than 20 T and temperatures lower than T_t the magnetization is constant in the magnetic field. At temperatures higher then T_t we have observed only one metamagnetic transition on this two-phased sample. Taking into account the amount of HT and LT phase in this two-phased sample and taking into account also the field dependency of magnetization on HT phase for configuration B || c we have tried to estimate the saturated moment at fields higher than 20 T applied along the c-axis for the LT phase. This saturated moment is roughly 2.6(2) μ_B/f.u. at 4.2 K. The saturated moment for the LT phase for fhield applied along the c-axis is still much lower than the theoretical moment for the Pr^{3+} ion. On the other hand this moment is comparable with the saturated moment determined for the field parallel to the a-axis of the HT phase.

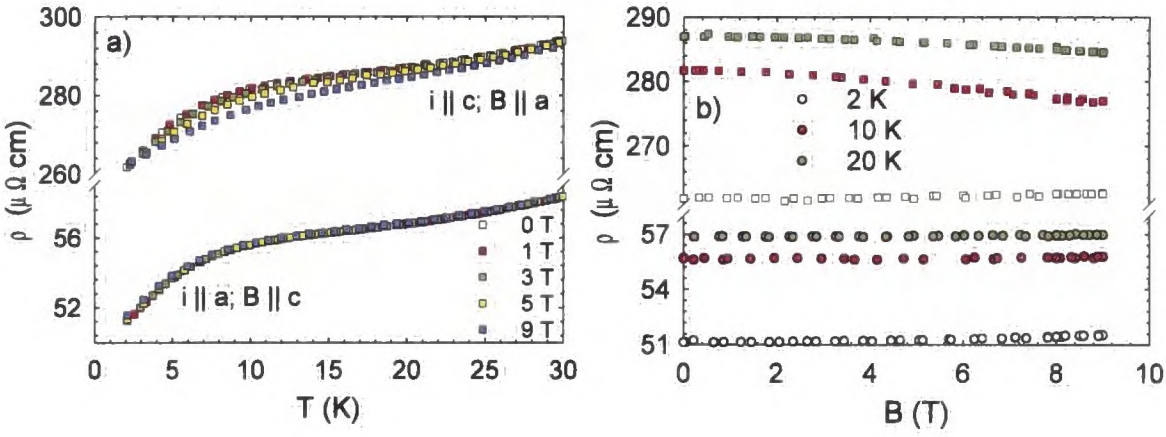

Figure 4.38: *The resistivity and longitudinal magnetoresistivity of the HT phase of $PrIr_2Si_2$: a) temperature scan at constant fields; b) field scans at different temperatures. The circles represent the $i \parallel a$; $B \parallel c$ experimental configuration and squares represent $i \parallel c$; $B \parallel a$ experimental configuration. The same colors represent the same temperatures in which the scans were done.*

The resistivity of HT phase measured along both main crystallographic axes at temperatures higher than 25 K exhibit a metallic behavior. However, at the temperatures lower than 20 K we have found a bump on the resistivity (Fig. 4.38a), which we have ascribed to the crystal field effect in this phase. This bump can be suppressed by the field applied along the a-axis, but is intact to the field applied along the c-axis. When we have performed a field scan in the constant temperatures (Fig. 4.38b) we have found the small positive magnetoresistivity in the configuration i $\parallel$ a; B $\parallel$ c, but the negative magnetoresistivity for the configuration i $\parallel$ c; B $\parallel$ a at temperatures 10 K and 20 K. The small positive magnetoresistivity may be explained by the Lorentz force, which will curve the trajectory of the moving electrons in the magnetic field and hence will increase the resistivity. On the other hand, the negative magnetoresistivity has to be explained as a decreasing of the magnetic contribution to the resistivity. This is consistent with the result that in the HT phase the magnetic moments lies in the basal plane, so magnetic field applied in the basal plane can partially order the magnetic moments, so the scattering of the electrons on the magnetic moments in compound will decrease.

In the case of the resistivity of LT phase we have again observed the metallic behavior for temperatures higher than 50 K. At the lower temperatures (Fig. 4.39) we have observed for current applied along both main crystallographic axes the small increase of the resistivity just below T_N and then abrupt drop of the resistivity at T_t. Another interesting result is that the ρ_c start to increase at temperatures below 10 K. When we have applied the magnetic field along the a-axis and electrical current along the c-axis (Fig. 4.39b) we have observed small positive magnetoresistivity and no shift of the anomalies connected with T_N

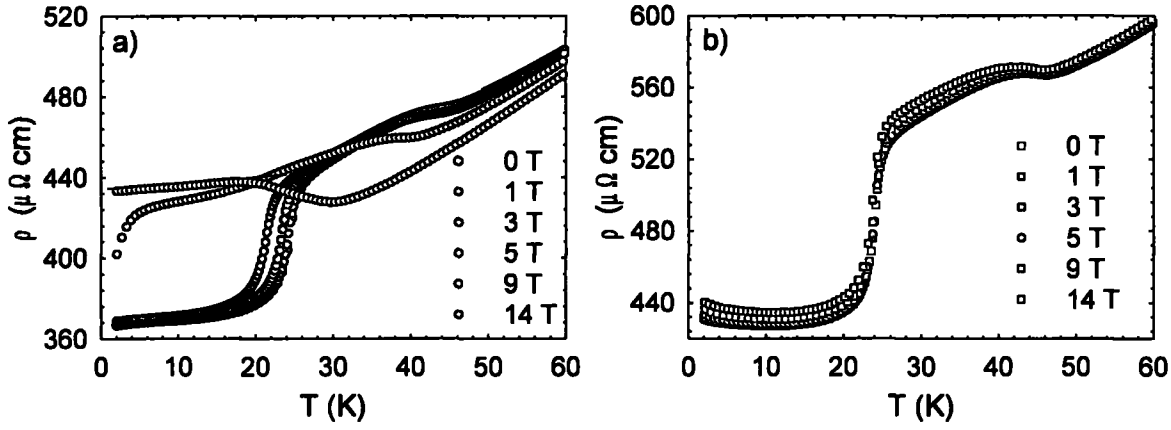

Figure 4.39: The temperature dependence of the resistivity of LT phase of $PrIr_2Si_2$ measured at constant magnetic field: a) experimental configuration $i \parallel a$; $B \parallel c$; b) $i \parallel c$; $B \parallel a$.

and T_t. The similar, positive magnetorestivity was confirmed by the field scans at constant temperature for this experimental configuration (Fig. 4.40b). In the case of current applied along the a-axis and magnetic field applied along the c-axis we have observed the shift of anomalies connected to T_N and T_t similar as in the magnetization measurement for field applied along the c-axis up to fields of 5 T. Instead of this we have found also the onset of the transition connected with T_t even for field B = 9 T close to 2 K. In the case of 14 T the transition connected with T_t completely smears out and we can observe only a minimum at the resistivity at 29.8 K, maximum at 18.8 K and then linear decrease of the resistivity at lower temperatures.

The field scans at the constant temperatures for the experimental configuration i $\parallel$ a; B $\parallel$ c (Fig. 4.40a) again revealed the hysteresis behavior, similar to the magnetization measurements (Fig. 4.36b). The resistivity at the metamagnetic transition increased for temperatures lower than 20 K. The most interesting magnetoresistivity curve is the 20 K curve on which we can observe first increase of the resistivity at 5.7 T, then almost plateau of the resistivity up to 12 T and then start to decrease of the resistivity at higher fields. Also by decreasing the magnetic field we have observed the hysteresis behavior at the lower metamagnetic transition. Such a behavior suggests, that the resistivity at the higher metamagnetic transition will decrease in applied magnetic field.

According to the results of magnetization, magnetic susceptibility and resistivity of the LT phase we suppose that the magnetic moment is parallel to the c-axis and M(T, B) phase diagram (Fig. 4.41) contain phases: AF phase 1 between T_N and T_t and AF phase 2 below T_t. AF 2 phase can be transformed by field of 8.1 T (at 2 K) applied along the c-axis to AF phase 1 and finally by field higher than 15.5(2) T; $B \parallel c$-axis to the field induced ferromagnetic state. This upper critical field, which is needed to completely

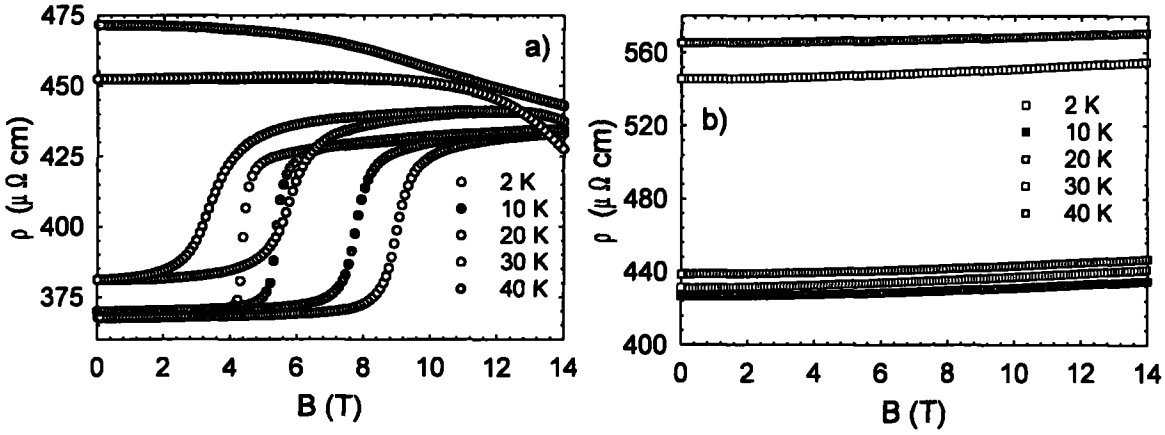

Figure 4.40: The field dependence of the resistivity of LT phase of $PrIr_2Si_2$ measured at constant temperature: a) experimental configuration $i \parallel a$; $B \parallel c$; b) $i \parallel c$; $B \parallel a$.

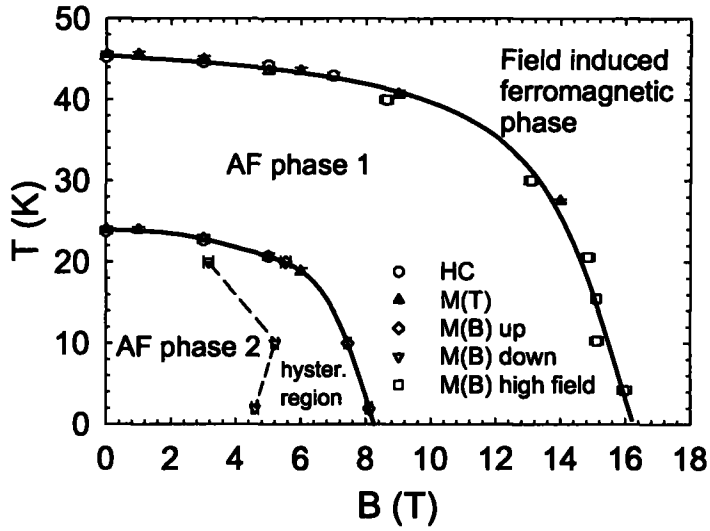

Figure 4.41: The phase diagram of LT phase of $PrIr_2Si_2$ compound for field applied along the c-axis.

transform LT phase to the field-induced ferromagnetic state decreases as the temperature reaches T_N. As there is clear transition from the one antiferromagnetic phase to the other antiferromagnetic phase, one should expect that the magnetic structure in these AF phases is somehow complicated. That's why the neutrons are highly desired to shed more light to the magnetism of LT phase of $PrIr_2Si_2$.

Chapter 5

General discussion

5.1 Single crystals vs. polycrystals

In this thesis we were focused on the preparing of the single-crystalline samples and measuring the basic physical properties on the single crystals. The question is, why to prepare and study the single crystalline samples if the polycrystalline samples can be prepared and studied much more easily? The answer is, that on the polycrystalline samples the spatial distribution of the physical properties is somehow averaged, but in the case of the single-crystalline samples it is not. This may play crucial role in case of the strongly anisotropic materials as used in this thesis. As one of the examples the magnetization may serve: It is quite impossible to obtain for example the information about the easy magnetization axis using the polycrystalline sample, but this information can be obtained by the rotating of the single-crystalline sample. In the case of the resistivity it is even worse, because for the magnetization measurements one can pulverize the sample and then measure on the randomly-oriented fixed powder. In this case one can obtain at least the spatially averaged magnetization. But in the case of the resistivity one had to cut the sample from the pellet, so the sample may consist of a partially oriented grains and one will not obtain even the averaged physical properties. For example the electrical resistivity of the CeRhSn compound measured on the polycrystalline sample exhibit the broad maximum at around 80 K [52], but the measurement on the single-crystalline sample revealed the metallic behavior of the resistivity for electric current applied along the c-axis and the bump on the resistivity only in the case of electric current applied along the a-axis (our measurements and Kim et. al. [93]).

Another problem of the polycrystalline sample might be that it is easy to obtain the impurity phases during the melting. This may cause for example if one start with slightly off-stoichiometric composition (and it is experimentally impossible to start from the ideal composition) or to combine the elements with the different vapor pressures at the melting temperature. In the periodical lattice, every impurity atom will induce some additional strain into the lattice, which will increase the total energy of the lattice, so there is strong

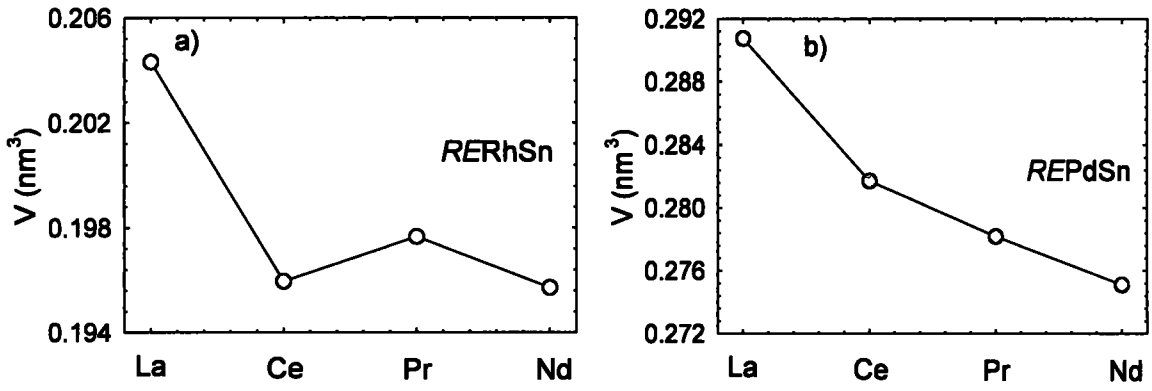

Figure 5.1: The evolution of the volume of a) RERhSn compounds and b) REPdSn compounds. The data for CePdSn were taken from [118]

tendency of the lattice to cast out the impurity atoms during the single crystal growing and in the average, the purity of the obtained single crystal is higher than the purity of its polycrystalline counterpart.

5.2 RETX compounds

The evolution of the volume of *RE*RhSn and *RE*PdSn compounds as obtained from the X-ray diffraction data is plotted on Figure 5.1. In the case of *RE*RhSn the volume of CeRhSn is the smallest from all four compounds. As the atomic volume of pure RE^{3+} ions decreases from La to Nd [119] , this anomalously smallest volume of CeRhSn can not be described by the atomic radius of Ce^{3+} ion, so we suppose, that the valency of Ce in CeRhSn compound is somewhere between 3+ and 4+. This is consistent with the previously published results on CeRhSn [53, 93, 117]. The similar mixed valency has also been observed in other CeRhX compounds [55, 66]. In the case of *RE*PdSn compounds there is no anomaly in the volume evolution, so one can expect that Ce in the CePdSn compound is in the Ce^{3+} state.

Both, LaRhSn and LaPdSn were found to become superconducting in the temperatures lower than 2 K [51, 63, 98]. This behavior is similar to many other La-based ternary intermetallic compounds, which become superconducting in temperatures below 2 K [64]-[66, 120, 121]. There also exists a group of La-based intermetallic compounds, which are not referred to become superconducting at low temperatures (for example LaIrAl [80]; LaNiSb [49]). All these compounds were measured only down to 2 K and they may become superconducting at lower temepratures.

The De Gennes scaling for the *R*RhSn and *R*PdSn compounds (R = Ce - Yb) is plotted on Figure 5.2. One of the most surprising result is that in the both cases the compounds

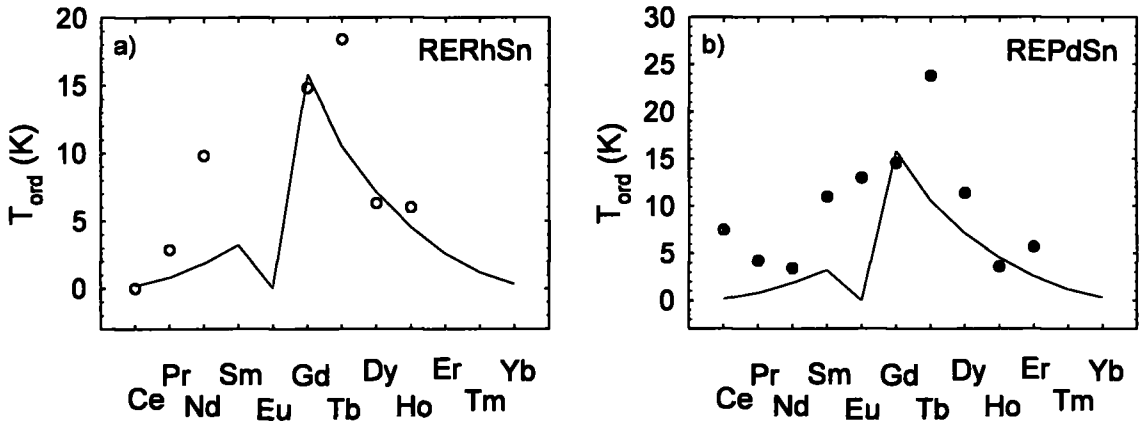

Figure 5.2: *The De Gennes scaling for a) RRhSn and b) RPdSn compounds. The data about the ordering temperatures for compounds, which we didn't studied in this thesis were taken from [53, 122, 123, 124] for RERhSn and from [99, 125, 126, 127] for REPdSn compounds. The line represents* $(g(JLS) - 1)^2 - J(J+1)$ *scaling.*

with Tb have higher ordering temperature than the compounds with Gd. Another very interesting result is that in the *RE*PdSn series the CePdSn orders antiferromagnetically at 7.5 K [69, 118, 128] and the ordering temperature from CePdSn to NdPdSn decreases, while from the De Gennes scaling one should expect the increasing of the ordering temperature. Actually, there exist more CeTX compounds, which order magnetically at anomalously high ordering temperatures (for example CeRhGe at 9.3 K [60], CePtSb at 4.5 K [69] and CePdSb at 17 K [70]). To conclude the results from De Gennes scaling in this two series we state that the both series do not obey De Gennes scaling. All compounds in the *RE*RhSn series crystallize in the ZrNiAl structure and all compounds in the *RE*PdSn series crystallize in the TiNiSi crystal structure which points that the discrepancy in the De Gennes scaling can not originate from the changing of the local crystal symmetry at the position of *RE* atom. The reason, why these two series do not obey De Gennes scaling is probably the strong crystal field effect in these compounds and the non-constant exchange constants between *RE* atoms through these series.

In the case of *RE*RhSn series the type of the magnetic ordering changes from the ferromagnetic for PrRhSn to the case of antiferromagnetic ordering and subsequent ferromagnetic ordering in NdRhSn. The GdRhSn, TbRhSn and DyRhSn compounds order antiferromagnetically [53, 122, 123], but HoRhSn again orders ferromagnetically. Closer look on the magnetization data of DyRhSn [123] compound reveals increase of the magnetization at temperatures below 2 K, so there might be another magnetic phase transition at temperatures lower than 2 K. In case, that this is true, the DyRhSn in this series can be compared with the NdRhSn: both of these compounds are just in the border between

the ferromagnetic and antiferromagnetic ordering in the series, so there are present two magnetic phase transitions[1].

All referred compounds of the *RE*PdSn series order antiferromagnetically. However, we have found another order-to-order magnetic phase transition for NdPdSn at 1.91 K. The similar order-to order magnetic phase transitions were also observed for HoPdSn at 2.5 K [127] and ErPdSn at 2.5 K [129]. As the lower-ordering temperatures are quite low (1.9 - 2.5 K) in these compounds and the ordered phase in this series is antiferromagnetic, one should expect that more of the *RE*PdSn compounds will undergo another order-to-order magnetic phase transition at low temperatures.

Generally, we have found, that for all Pr- and Nd-based compounds the magnetic moments are localized on the *RE* atom and there is no instability in these systems. The results on CePdSn also revealed, that the Ce in this compound is in stable Ce^{3+} configuration and orders antiferromagnetically. The only studied compound in which the *RE* ion was unstable is CeRhSn. Ce in this material was found in the intermediate-valency state. The subsequence of this intermediate-valency state is the non-Fermi liquid behavior in this compound.

5.3 RET2X2 compounds

In 1985 Hoffmann and Zheng [130] tried to calculate the X–X bonding energy in the AB_2X_2-type compounds. They have supposed the layered structure in which the A^{2+} cations were sandwiched between the $B_2X_2^{2-}$ layers. They have found that theoretically there can be two energetic minima caused by the "bonding", "Coulomb" and "packing" requirements in these compounds. As the consequence of these two minima they have predicted a possible phase transition for some compounds. At this time such a compound with two different crystallographic structures was already known ($LaIr_2Si_2$ [109]) and in few years the similar polymorphism[2] as in the $LaIr_2Si_2$ was also observed for $RENi_2As_2$ (*RE* = La, Ce, Pr, Nd and Sm) series [131, 132]. Up to now, there are known some other compounds with the similar polymorphism: UCo_2Ge_2 [133] $CeIr_2Si_2$ [110] and $YbIr_2Si_2$ [134]. Nowadays we have observed this polymorphism also for the $PrIr_2Si_2$ and very recent results indicate such a polymorphism also for the $NdIr_2Si_2$ compound. It is interesting to compare $REIr_2Si_2$ series with another 1-2-2 compounds exhibiting the similar structural instabilities. In the case of $LaNi_2As_2$ Ghadraoui et al. [131] found no superconductivity, which is different from the $LaIr_2Si_2$, where the superconductivity was found [109]. However, Ghandraoui et. al. performed measurements only down to 2 K and many of La-based ternary intermetallic compounds have the critical superconducting temperature lower than 2 K. LT phase of $CeNi_2As_2$ was found to be antiferromagnetic below 5.2 K [131], but we have found both

[1] In the case of NdRhSn T_N = 9.8 K and T_C = 7.6 K; in the case of DyRhSn T_N = 6.3 K and there might be another order-to-order magnetic phase transition.

[2] the compound have two different crystallographic modifications: high temperature, $CaBe_2Ge_2$-type and low temperature $ThCr_2Si_2$ crystal structure.

phases of $CeIr_2Si_2$ with no magnetic ordering. This might be caused by the different electronic configuration of Ni and Ir: Ni has in the valence band one more *d*-electron than Ir, which may cause the fluctuating of the Ce valency in the $CeIr_2Si_2$. Also, both phases of $PrNi_2As_2$ were found to order antiferromagnetically [131], but we have found magnetic ordering only for the LT phase of $PrIr_2Si_2$. In the case of UCo_2Ge_2 the HT phase does not order magnetically above 2 K, but the LT phase orders antiferromagnetically below 174(3) K [133]. This makes UCo_2Ge_2 better compound to compare with $PrIr_2Si_2$.

We have found the both phases of $CeIr_2Si_2$ to be in the intermediate configuration fluctuation state. This result place the $CeIr_2Si_2$ into the same group of materials as intermediate configuration fluctuating compounds YB_4 [113], U_2Ru_2Sn [135], U_2RuGa_8 [135] and $Yb_2Ni_{12}P_7$ [136]. The resistivity of HT phase of $CeIr_2Si_2$ is linear at low temperatures, which apply that this phase behaves as a non-Fermi liquid compound. On the other hand the resistivity of LT phase obeys T^2 law, which suggests that this phase behaves as Fermi liquid compound. So $CeIr_2Si_2$ seems to be just at the border between the non-Fermi liquid and Fermi liquid compounds and the side of the border is chosen by the crystal structure of the compound. In the literature there are known many compounds in which the change from Fermi liquid to non-Fermi liquid state is induced for example by applied hydrostatic pressure (UGa_3 [137], $BaVS_3$ [138] and many others) but up to our knowledge $CeIr_2Si_2$ compound is the first compound in which this change occurs by the changing of the crystal symmetry.

Chapter 6

Summary and conclusions

We have grown the single crystals of *RE*RhSn (*RE* = La, Pr and Nd) series; *RE*PdSn (*RE* = La, Pr and Nd) series and $CeIr_2Si_2$ and $PrIr_2Si_2$ compounds. Note that many of these single crystals are up to our knowledge the first single crystals of these compounds in the world.

LaRhSn compound was confirmed to become superconducting at temperatures lower than 1.85(5) K. We can also conclude that the superconductivity in this material can not be fully described by the BCS theory.

In the case of CeRhSn we have confirmed the maximum in the *a*-axis resistivity at 54 K, while *c*-axis resistivity decreased monotonously with the decreasing temperature. At low temperatures we have fitted the resistivity of CeRhSn by the equation $\rho(T) = \rho_0 + AT^n$ with the exponents $n = 0.76$ and $n = 1.7$ for the *a*-axis and *c*-axis, respectively. This, together with the upturn in C/T vs. T curve at low temperatures points to the NFL scenario in this compound.

PrRhSn was found to order ferromagnetically at $T_c = 2.85(3)$ K. This compound exhibits the strong magnetocrystalline anisotropy with the *c*-axis to be the easy magnetization axis. The magnetic anisotropy in this compound was extrapolated to be around 65 T. According to the specific heat measured in the applied magnetic field along the *c*-axis we have calculated the strong magnetocaloric effect in this compound at temperatures around 10 K. The resistivity of this compound measured along the both main crystallographic axes exhibits a bump below 15 K which we have ascribed with the strong crystal field in this compound.

In the case of NdRhSn we have found two magnetic phase transitions: paramagnetic – antiferromagnetic phase transition at $T_N = 9.8$ K and antiferromagnetic – ferromagnetic phase transition at $T_C = 7.6$ K. We have found no superconducting phase transition as proposed by Łątka et. al. [97]. Similarly to PrRhSn we have found that *c*-axis is the easy magnetization axis also for the NdRhSn. The fragility of the magnetic structure between T_N and T_C was concluded after finding out that the metamagnetic transition in this compound occurs between 0.08 and 0.1 T for temperatures between T_N and T_C. The magnetic moment in this compound was observed only on Nd^{3+} ions, reaching only

2.2(1) μ_B/Nd at 2 K. Both magnetic phase transitions shift to the lower temperatures and the metamagnetic transition shifts to the higher applied magnetic fields by applying the hydrostatic pressure up to 0.8 GPa. Nowadays, our collaborators have also performed the uniaxial-pressure experiment on this material which is not included in the thesis and the single crystal neutron diffraction experiment, which is included in [104]. The next step in the studying of this material will be the neutron diffraction experiment under the applied hydrostatic and uniaxial pressure. For this our collaborators already obtained the beamtime on the E4 diffractometer in BENSC, Berlin.

LaPdSn was found to be normal metal down to 2 K, but our collaborators nowadays found that the compound undergoes a superconducting transition at 150 mK [98]. Analysis of the specific heat data of this compound leads to the coefficients $\gamma = 11(1)$ mJmol^{-1}K^{-2} and $\Theta_D = 196(1)$ K.

PrPdSn was found to be antiferromagnetic with $T_N = 4.2(1)$ K. The magnetization curves of this compound measured along all main crystallographic axes obey the Curie-Weiss law at temperatures higher than 50 K and the behavior of the magnetization near T_N suggests that there is ferromagnetic coupling of the magnetic moments along the a-axis and antiferromagnetic coupling along the remaining two axes. Also the b-axis is the easy-magnetization direction in this system and the metamagnetic transition for the field applied along this axis occurs at fields less than 1 T.

NdPdSn was found to be with two phase transitions: from paramagnetic to antiferromagnetic phase at $T_N = 3.4(1)$ K and with another order-to-order phase transition at $T_1 = 1.91(3)$ K. The lower transition was never referred before. The entropy of this system reaches only $R \ln 7$ at 80 K which is much smaller than the expected value for the Nd^{3+} ion. The $M(T)$ curves at the paramagnetic state are linear and fits together, but this is only a coincidence. The $M(B)$ curves measured along all main crystallographic axes do not fit together and these curves unambiguously revealed strong magnetocrystalline anisotropy in this compound.

Both, $CeIr_2Si_2$ and $PrIr_2Si_2$ compounds crystallize in the two different crystallographic phases: high-temperature (HT) phase of $CaBe_2Ge_2$-type crystal structure and low temperature (LT) phase of $ThCr_2Si_2$-type crystal structure.

Both phases of $CeIr_2Si_2$ were found not to order magnetically at temperatures higher than 2 K. However, we have found that the susceptibility can be described in the terms of the interfluctuating configuration model and that the majority of Ce atoms is in the 4+ configuration. According to the resistivity measurements of both phases it seems that $CeIr_2Si_2$ is just at the border between the non-Fermi-liquid and Fermi-liquid compounds and the side of the border is chosen by the crystal structure of the compound and by the c/a ratio in the crystal structure.

In the case of $PrIr_2Si_2$ is that the HT phase is nonmagnetic, while the LT phase exhibits very complex magnetic phase diagram: it undergoes paramagnetic-antiferromagnetic phase transition at $T_N = 45.5(1)$ K and another change of the antiferromagnetic phase at $T_t = 23.7(2)$ K. $PrIr_2Si_2$ in this phase also undergoes two metamagnetic phase transitions

for the magnetic field applied along the c-axis at temperatures lower than T_t. The lower-field metamagnetic transition (at B = 8.1 T; T = 2 K) exhibit a hysteresis as large as 3.5 T at 2 K. The higher-field metamagnetic transition (at B = 15.5(2) T; T = 4.2 K) seems to be with hysteresis lower than 0.5 T. Another very important result is that in the case of HT phase we suppose that the magnetic moment lies in the basal plane, but in the case of LT phase the magnetic moment is aligned along the c-axis. As there is no difference of the volume between the HT and LT phase, this is also the consequence of different c/a ratio and hence different distance between the nearest neighbor and next-nearest neighbor atoms. To better understand of the magnetism in this compound we have applied for the neutron diffraction experiment in the BENSC, Berlin and as a first step we have obtained the beamtime for the powder diffraction experiment on E6 diffractometer. The next step will be the application for the single crystal neutron diffraction experiment.

Bibliography

[1] N. W. Ashkroft and N. D. Mermin, Solid State Physics, Saunders College Publishing, (1976).

[2] M. T. Hutchings, Solid State Phys. **16** (1964), 227.

[3] M. Diviš, J. Rusz, G. Hilscher, H. Michor, P. Blaha and K.Schwarz, Czechoslovak J. of Phys. **52** (2002), 283.

[4] M.A. Rudreman and C. Kittel, Phys. Rev. **96** (1954), 99.

[5] I. A. Campbell, J. Phys. **2** (1972), L47.

[6] M. Mihalik, H. Kitazawa, M. Diviš and V. Sechovský, J. All. & Comp. **460** (2008), 26.

[7] Y. Haga, M. Nakashima, R. Settai, S. Ikeda, T. Okubo, S. Araki, T. C. Kobayashi, N. Tateiwa and Y. Ōnuki, J. Phys.: Condens. Matter **14** (2002), L125.

[8] N. Iwata, Y. Matsuzaki and T. Shigeoka, J. Magn. Magn. Mater **128** (1993), 279.

[9] N. Harrison, M. Jaime and J.A. Mydosh, J. Magn. Magn. Mater **272 - 276** (2004), e135.

[10] R. Abbaschian: Crystal Growth; The Encyklopedia of Materials, Elsevier Science Publishers, 2001.

[11] V. Valvoda, M. Polcarová and P. Lukáč, Základy strukturní analýzy, Karolinum Praha, (1992).

[12] J. Baruchel, J. L. Hodeau, M. S. Lehmann, J. R. Regrand, C. Schlenker, Neutron and synchrotron radiation for condensed matter studies, Springer-Verlag, 1993.

[13] `http://www-llb.cea.fr/fullweb/fp2k/fp2k_os.htm4`.

[14] `http://www.ccp14.ac.uk/tutorial/lmgp/orientexpress.htm`.

[15] Ch. Kittel, Úvod do fyziky pevných látek, Academia Praha, 1985.

[16] P. Svoboda, P. Javorský, M. Diviš, V. Sechovský, F. Honda, G. Oomi and A. A. Menovsky, Phys. Rew. B **63** (2001), 212408.

[17] D. C. Mattis, The theory of magnetism II. Thermodynamics and statistical mechanics, vol. 55, Springer Verlag, 1985.

[18] A. Czopnik, N. Shitsevalova, A. Krivchikov, V. Pluzhnikov,Y. Paderno and Y. Ōnuki, J. Sol. State Chem **177** (2004), 507.

[19] M. Rotter, M. Doerr, M. Loewenhaupt, U. Whitte, P. Svoboda, J. Vejpravová, H. Sassik, C. Ritter, D. Eckert, A. Handstein and D. Hinz, Phys. Rew. B **64** (2001), 134405.

[20] J. D. Baloga and C. W. Garland, REv. Sci. Instrum **48** (1977), 105.

[21] J. S. Hwang, K. J. Lin and Ch. Tien, Rev. Sci. Instr. **68** (1997), 94.

[22] `http://www.qdusa.com/products/ppms.html`.

[23] H. Nowotny and E. Gratz: Boltzmann Equation and Scattering Mechanisms; The Encyklopedia of Materials, Elsevier Science Publishers, 2001.

[24] A.R. Mackintosh, Phys. Let. **4** (1963), 140.

[25] A.R. Mackintosh, Phys. Rev. Let. **9** (1962), 90.

[26] N. H. Andersen and H. Smith, Phys. Rev. B **19** (1979), 384.

[27] E. Gratz: Magnetoresistance: Magnetic and Nonmagnetic Intermetallics; The Encyklopedia of Materials, Elsevier Science Publishers, 2001.

[28] A. Fert and P. M. Levy, Phys. Rev. B **36** (1987), 1907.

[29] *J. Brož a kolektív, Základy fysikálních měření, Státní Pedagogické nakladatelství Praha, 1967.*

[30] `http://www.qdusa.com/products/mpms.html`.

[31] `http://www.nims.go.jp/TML/english/maglist.html#anc01`.

[32] `http://www.ifw-dresden.de/institutes/imw/sections/22/`.

[33] G. Oomi, M. Ohashi, Y. Uwatoko, I. Satoh and T. Komatsubara, Phys. B **359-361** (2005), 67.

[34] J. Kamarád, Z. Arnold and M.R. Ibarra, J. Magn. Magn. Mater **140-144** (1995), 837.

[35] M. Eremets: High pressure experimental methods; Oxford Science Publications 1996.

[36] High Pressure CuBe Cell "SQUID"; Instruction manual, High Pressure Lab, IP ASCR.

[37] J. Baruchel, J.L. Holdeau, M. S. Lehmann, J.R. Regnard and C. Schlenker; Neutron and Synchrotron Radiation for Condensed Matter Physics, Springer-Verlag, (1994).

[38] `http://www.goodfellow.com/csp/active/STATIC/`.

[39] `http://www.ill.eu/html/d1b/home/`.

[40] V. F. Sears, Neutron News **3** (1992), 26.

[41] `http://www.ill.eu/vivaldi/home/`.

[42] A. Szytuła in Handbook of Magnetic Materials, vol. 6, Elseviere Science Publishers B. V., 1991.

[43] M. G. Haase, T. Schmidt, C. G. Richter, H. Block and W. Jeitschko, J. Sol. State Chem. **168** (2002), 18.

[44] M. Kasaya, H. Suzuki, T. Yanaguchi and K. Katoh, J. of the Phys. Soc. of Jap. **61** (1992), 4187.

[45] R. Welter, G. Venturini, B. Malaman and E. Ressouche, J. All. & Comp. **202** (1993), 165.

[46] R. Welter, G. Venturini, B. Malaman and E. Resouche, J. All. & Comp. **201** (1993), 191.

[47] R. Welter, G. Venturini, E. Ressouche and B. Malaman, J. All. & Comp. **210** (1994), 279.

[48] R. Welter, G. Venturini and B. Malaman, J. All. & Comp. **189** (1992), 49.

[49] K. Hartjes and W. Jeitscho, J. All. & Comp. **226** (1995), 81.

[50] A. Zygmunt and A. Szytula, J. All. & Comp. **219** (1995), 185.

[51] F. Canepa and S. Cirafici, J. All. & Comp. **232** (1996), 71.

[52] A. Ślebarski, M. B. Maple, E. J. Freeman, C. Sirvent, M. Radłowska, A. Jezierski, E. Granado, Q. Huang and J. W. Lynn, Phyl. Mag. B 82 (2002), 943.

[53] Ch.D. Routsi, J.K. Yakinthos and H. Gamari-Seale, J. Magn. Magn. Mater **117** (1992), 79.

[54] K. Lątka, R. Kmieć, J. Gurgul, A. W. Pacyna, M. Rams, T. Schmidt, R. Pottgen, J. Magn. Magn. Mater **301** (2006), 359.

[55] D. T. Adroja, S. K. Malik, B. D. Padalia and R. Vijayaraghavan, Phys. Rev. B **39** (1989), 4831.

[56] H. Fujii, T. Takabatake and Y. Andoh, J. All. & Comp. **181** (1992), 111.

[57] D. Niepmann, Y. M. Prots, R. Pottgen and W. Jeitschko, J. Sol. Stat. Chem. **154** (2000), 329.

[58] A. E. Dwight, J. Less.-Comm. Met. **93** (1983), 411.

[59] A. Szytuła, B. Penc and N. Stusser, J. Magn. Magn. Mater. **265** (2003), 94.

[60] B. Chevalier, P. Rogl, J. Etourneau and M. J. Besnus, J. Magn. Magn. Mater. **83** (1990), 303.

[61] S. Yoshii, D. Tazawa and M. Kasaya, Phys. B **230 - 232** (1997), 380.

[62] B. Chevalier, J.-L. Bobet, M. Pasturel, E. Gaudin and J. Etourneau, J. All. & Comp. **356 - 357** (2003), 147.

[63] Matúš Mihalik, V. Sechovský, M. Diviš, S. Gabáni and Marián Mihalik, J. All. & Comp. **452**(2008), 241.

[64] Y. Echizen, K. Umeo and T. Takabatake, Sol. Stat. Commun. **111** (1999), 153.

[65] S.K. Malik, H. Takeya and K.A. Gschneider, J. All. & Comp. **207 - 208** (1994), 237.

[66] N. H. Kumar and S. K. Malik, Sol. Stat. Commun. **114** (2000), 223.

[67] I. Karla, J. Pierre and R.V. Skolozdra, J. All. & Comp. **265** (1998), 42.

[68] M. Kasaya, T. Tani, F. Iga and T. Kasuya, J. Magn. Magn. Mater **76 - 77** (1988), 278.

[69] M. Kasaya, T. Tani, K. Ohoyarna, M. Kohgi and Y. Isikawa, J. Magn. Magn. Mater. **104 - 107** (1992), 665.

[70] S.K. Malik and D.T. Adroja, Phys. Rev. B **43** (1991), 6295.

[71] B. D. Rainford and D. T. Adroja, Phys. B **194 - 196** (1994), 365.

[72] K. Satoh, T. Fujita, Y. Maeno, Y. Uwatoko and H. Fujii, J. Phys. Soc. Jpn **59** (1990), 810.

[73] L. Rebelsky, K. Reilly, S. Horn, H. Borges, J. D. Thompson, J. O. Willis, R. Caspari and C. D. Bredl, J. Appl. Phys. **63** (1988), 3405.

[74] H. Higaki, I. Ishii, M.-S. Kim, D. Hirata, T. Takabatake and T. Suzuki, Phys. B **359-361** (2005), 136.

[75] S. K. Malik and D. T. Adroja, Phys. Rev. B **43** (1991), 6277.

[76] S. Yoshii, M. Kasaya, H. Takahashi and N. Mori, Phys. B **223 - 224** (1996), 421.

[77] I. Karla, J. Pierre, A. P. Murani and M. Neumann, Phys. B **271** (1999), 294.

[78] K. A. McEwen, J. Jensen, E. D. Beirne, J. P. Allen, K. Habicht, D. T. Adroja, R. I. Bewley and D. Fort Phys. Rev. B **73** (2006), 014402.

[79] A. Szytuła, M. Koleda, E. Ressouche and A. Zygmunt, J. All & Comp. **259** (1997), 36.

[80] N. H. Kumar, L. Menon, C. R. V. Rao, S. K. Malik, P. Raj, A. Sathyamoorthy, K. Shashikala, Sol. Stat. Commun. **109** (1999), 345.

[81] V. I. Zaremba, Y. M. Kalychak, V. P. Dubenskiy, R.-D. Hoffmann and R. Pottgen, J. Sol. Stat. Chem. **152** (2000), 560.

[82] P. Javorský, V. Sechovský, R.R. Arons, P. Burlet, E. Ressouche, P. Svoboda and G. Lapertot, J. Magn. Magn. Mater **164** (1996), 183.

[83] P. Javorský, V. Sechovský, L. Havela and H. Michor, J. Magn. Magn. Mater. **177-181** (1998) 1052.

[84] L. Keller, A. Donni, H. Kitazawa, J. Tang, F. Fauth and M. Zolliker, Phys. B **241 - 243** (1998), 660.

[85] M. Kurisu, R. Hara, G. Nakamoto, Y. Andoh, S. Kawano, D. Schmitt, Physica B **312-313** (2002), 861.

[86] P. A. Kotsanidis, J. K. Yakinthos, E. Roudaut and H. Gamari-Seale, J. Magn. Magn. Mater. **131** (1994), 139.

[87] Y. M. Prots, R. Pottgen, D. Niepmann, M. W. Wolff and W. Jeitschko, J. Sol. Stat. Chem. **142**, (1999) 400.

[88] S. Ramakrishnan, K. Ghosh, A. D. Chinchure, V. R. Marathe and G. Chandra, Phys. Rev. B **52** (1995), 6784.

[89] W. Bażela, A. Zygmunt, A. Szytula, E. Ressouche, J. Leciewicz and W. Sikora, J. All. & Comp. **243** (1996), 106.

[90] S. Baran, J. Leciejewicz, N. Stusser, A. Szytuła, A. Zygmunt and V. Ivanov, J. Phys. Cond. Mater. 8 (1996), 8397.

[91] P. C. Canfield, J. D. Thompson, W. P. Beyermann, A. Lacerda, M. F. Hundley, E. Peterson, Z. Fisk and H. R. Ott, J. Appl. Phys. **70** (1991), 5800.

[92] P.-C. Ho, V. S. Zapf, A. Ślebarski and M. B. Maple, Phil. Mag. 84 (2004), 2119.

[93] M. S. Kim, Y. Echizen, K. Umeo, S. Kobayashi, M. Sera, P. S. Salamakha, O. L. Sologub, T. Takabatake, X. Chen, T. Tayama, T. Sakakibara, M. H. Jung and M. B. Maple, Phys. Rev. B **68** (2003), 054416.

[94] A. Ślebarski, M. Radłowska, T. Zawada, M. B. Maple, A. Jezierski and A. Zygmunt, Phys. Rev. B **66** (2002), 104434.

[95] T. Schmidt, D. Johrendt, C. P. Sebastian, R. Pottgen, K. Łątka and R. Kmieć, Z. Naturforsch. **60b** (2005), 1036.

[96] K. Łątka, R. Kmieć, J. Gurgul, M. Rams, A.W. Pacyna, T. Schmidt, R. Pottgen, J. Sol. Stat. Chem. **178** (2005) 3101.

[97] K. Łątka, R. Kmieć, R. Kruk, A. W. Pacyna, M. Rams, T. Schmidt, R. Pottgen, Nukleonika **48** (2003), S35.

[98] H. Ryll, "Aufbau und Vergleich verschiedener thermometrischer Messverfahren fur den Temperaturbereich T = 0.005 - 1 K in hohen Magnetfeldern bis 20 T", diploma thesis, Technische Universitat Berlin, 2008.

[99] D.T. Adroja and S.K. Malik, Phys. Rew. B **45** (1992), 779.

[100] M. Kolenda, S. Baran, A. Oleś, N. Stusser , A. Szytuła, J. All. & Comp. **269** (1998), 25.

[101] Y. Aoki, J. Urakawa, H. Sugawara, H. Sato, T. Fukuhara and K. Maezawa, J. Phys. Soc. Jpn. **66** (1997) 2993.

[102] F. R. Kroeger and C. A. Swenson, J. Appl. Phys. **48** (1977), 853.

[103] A. Ślebarski, K. Grube, R. Lortz, C. Meingast, H.v. Lohneysen, J. Magn. Magn. Mater. **272-276** (2004), 234.

[104] Prokleška J., Cohesive and magnetoelastic properties of materials with strongly correlated electrons, PhD Thesis, Charles University (2008).

[105] K. Kadowaki and S. B. Woods, Sol. Stat. Commun. **58** (1986), 507.

[106] A. Domman, F. Hulliger and Ch. Baerlocher, J. Less-Common Met. **138** (1988), 113.

[107] J.K. Yakinthos and P.F. Ikonomou, Sol. Stat. Commun. **34** (1980), 777.

[108] K. Hiebl and P. Rogl, J. Magn. Magn. Mater. **50** (1985), 39.

[109] H. F. Braun, N. Engel and E. Parthé, Phys. Rev. B **28** (1983), 1389.

[110] D. Niepmann and R. Pottgen, Intermetallics **9** (2001), 313.

[111] R. Welter, K. Halich and B. Malaman, J. All. & Comp. **353** (2003), 48.

[112] K. Hiebl, C. Horvath and P. Rogl, J. Less-Common Met. **117** (1986), 375.

[113] J. Y. Kim, B. K. Cho, H. J. Lee and H.-C. Kim, J. Appl. Phys. **101** (2007), 09D501.

[114] Ch. Mazumdar, R. Nagarajan, S. K. Dhar, L. C. Gupta, R. Vijayaraghavan and B. D. Padalia, Phys. Rev. B **46** (1992), 9009.

[115] B. C. Sales and D. K. Wohlleben, Phys. Rev. Let. **35** (1975), 1240.

[116] W. Franz, F. Steglich, W. Zell, D. Wohlleben and F. Pobell, Phys. Rev. Let. **45** (1980), 64.

[117] Y. Bando, T. Suemitsu, K. Takagi, H. Tokushima, Y. Echizen, K. Katoh, K. Umeo, Y. Maeda and T. Takabatake, J. All & Comp **313** (2000),1.

[118] F. Iga, M. Kasaya, H. Suzuki, Y. Okayama, H. Takahashi and N. Mori, Phys. B **186-188** (1993), 419.

[119] V. Sechovský: Magnetism in Solids: General Introduction; The Encyklopedia of Materials, Elsevier Science Publishers, 2001.

[120] J. Evers, G. Oehlinger, A. Weiss and C. Probst, Sol. Stat. Commun. **50** (1984), 61.

[121] W. H. Lee, F. A. Yang, C. R. Shih and H. D. Yang, Phys. Rev. B **50** (1994), 6523.

[122] S. Barana, M. Bałanda, P. Fischer, W. Sikora and A. Szytula, J. Magn. Magn. Mater. **261** (2003), 369.

[123] S. Baran, D. Kaczorowski, D. Sheptyakov and A. Szytula, J. Magn. Magn. Mater. **296** (2006), 89.

[124] K. Lątka, R. Kmieć, A. W. Pacyna and R. Po ttgen, J. Magn. Magn. Mater. **320** (2008), L18.

[125] S. K. Malik, D. T. Adroja, S. K. Dhar, R. Vijayaraghavan and B. D. Padalia, Phys. Rev. B **40** (1989), 2414.

[126] Y. Andoh, M. Kurisu, G. Nakamoto, T. Himi and S. Kawano, J. Magn. Magn. Mater. **272-276** (2004), e361.

[127] Y. Andoh, M. Kurisu, G. Nakamoto, T. Tsutaoka, Y. Makihara, T. Kosugi and S. Kawano, Phys. B **327** (2003), 389.

[128] G. M. Kalvius, D. R. Noakes, A. Kratzer, K. H. Munch, R. Wappling, H. Tanaka, T. Takabatake and R. F. Kiefl, Phys. B **206-207** (1995), 205.

[129] G. André, F. Bouré, M. Guillot, M. Kolenda, A. Oleś, W. Sikora, A. Szytula and A. Zygmunt, J. Magn. Magn. Mater **140-144** (1995), 879.

[130] R. Hoffmann and Ch. Zheng, J. Phys. Chem. **89** (1985), 4175.

[131] E. H. El Ghadraoui, J. Y. Pivan, R. Guérin, O. Pena, J. Padiou and M. Sergent, Mat. Res. Bull. **32** (1988), 1345.

[132] W. Jeitschko, W. K. Hofmann and L. J. Terbuchte, J: Less-Comm. Met. **137** (1988), 133.

[133] T. Endstra, G. J. Nieuwenhuys, A. A. Menovsky and J. A. Mydosh, J. Appl. Phys. **69** (1991), 4816.

[134] Z. Hossain, C. Geibel, F. Weickert, T. Radu, Y. Tokiwa, H. Jeevan, P. Gegenwart, and F. Steglich, Phys. Rev. B **72** (2005), 094411.

[135] R. Troć, Mat. Sci.-Pol. **24** (2006), 585.

[136] B.K. Cho, F.J. DiSalvo, J.S. Kim, G.R. Stewart and S.L. Budko, Phys. B **253** (1998) 40.

[137] M. Nakashima, Y. Haga, F. Honda, T. Eto, G. Oomi, T. Kagayama, N. Takeshita, T. Nakanishi, N. Môri, D. Aoki, R. Settai and Y. Ōnuki, J. Phys. Cond. Matter **13** (2001) L569.

[138] L. Forró, R. Gaál, H. Berger, P. Fazekas, K. Penc, I. Kézsmérki and G. Mihály, Phys. Rev. Let. **85** (2000), 1938.

Appendix A

RETX compounds

A.1 Structural corresponding

The confusion, if the X-ray pattern be indexed due to 1–2 phase or by its ternary superstructure (combined of two or more unit cells of 1–2 phase) is in the most cases caused by the similar scattering lengths of p and d metal, so in case of not sufficient statistic the peaks of the superstructure can be left unspotted in the X-ray pattern. This section recapitulates the possible 1–2 structures and their ternary superstructures:

CaF_2 ($Fm3m$) → MgAgAs ($F\bar{4}3m$)

$MgCu_2$ ($Fd\bar{3}m$) → PrMnGa ($Fd\bar{3}m$)

$CaIn_2/MgZn_2$($P6_3/mmc$) → LiGaGe ($P6_3mc$)

Fe_2P ($P\bar{6}2m$) → ZrNiAl ($P\bar{6}2m$)

AlB_2/Ni_2In ($P6/mmm$) → ZrBeSi ($P6_3/mmc$)

Si_2Th ($I4_1/amd$) → LaPtSi ($I4_1md$)

$CeCu_2/KHg_2$ ($Imma$) → TiNiSi ($Pnma$)

$PbCl_2$ ($Pnma$) → TiNiSi ($Pnma$)

A.2 Crystal structures

MgAgAs type:

Space group: $F\bar{4}3m$; crystallographic positions:	RE	4(c)	1/4	1/4	1/4
	T	4(a)	0	0	0
	X	4(d)	3/4	3/4	3/4

PrMnGa type:

Space group: $P2_13$; crystallographic positions:	RE	4(a)	0.1325[1]	0.1325[1]	0.1325[1]
	T	4(a)	0.4230[1]	0.4230[1]	0.4230[1]
	X	4(a)	0.839[1]	0.839[1]	0.839[1]

LaIrSi type:

Space group: $Fd\bar{3}m$; crystallographic positions:	RE	16(d)	5/8	5/8	5/8
	T	16(d)	5/8	5/8	5/8
	X	8(a)	0	0	0

LiGaGe type:

Space group: ($P6_3mc$); crystallographic positions:	RE	2(a)	0	0	0.247[1]
	T	4(b)	1/3	2/3	0.059[1]
	X	2(b)	1/3	2/3	0.444[1]

ZrNiAl type:

Space group: ($P\bar{6}2m$); crystallographic parameters:	RE	3(f)	0.59[1]	0	0
	T1	1(a)	0	0	0
	T2	2(d)	1/3	2/3	1/2
	X	3(g)	0.24[1]	0	1/2

ZrBeSi type:

Space group: ($P6_3/mmc$); crystallographic parameters:	RE	2(a)	0	0	0
	T	2(c)	1/3	2/3	1/4
	X	2(d)	1/3	2/3	3/4

LaPtSi type:

Space group: ($I4_1md$); crystallographic parameters:	RE	4(a)	0	0	0.010[1]
	T	4(a)	0	0	0.589[1]
	X	4(a)	0	0	0.419[1]

CeFeSi/PbFCl type:

Space group ($P4/nmm$); crystallographic parameters:	RE	2(c)	1/4	1/4	0.67[1]
	T	2(a)	3/4	1/4	0
	X	2(c)	1/4	1/4	0.17[1]

[1]free parameter in the structure

TiNiSi/CaCuGe type:

	RE	4(c)	0.19[1]	1/4	0.59[1]
Space group: ($Pnma$); crystallographic parameters:	T	4(c)	0.80[1]	1/4	0.58[1]
	X	4(c)	0.01[1]	1/4	0.20[1]

CeCoAl type:

	RE	4(i)	0.13[1]	0	0.33[1]
Space group: $C2/m$; crystallographic parameters:	T	4(i)	0.41[1]	0	0.19[1]
	X	4(i)	0.19[1]	0	0.85[1]

[1]free parameter in the structure

Appendix B

RET2X2 compounds

B.1 Crystal structures

$ThCr_2Si_2$ type:

Space group: $I4/mmm$; crystallographic parameters:

RE	2(a)	0	0	0
T	4(d)	0	1/2	1/4
X	4(e)	0	0	0.37[1]

$CaBe_2Ge_2$ type:

Space group: $P4/nmm$; crystallographic parameters:

RE	2(c)	1/4	1/4	0.24[1]
T_1	2(b)	1/4	3/4	1/2
T_2	2(c)	1/4	1/4	0.87[1]
X_1	2(a)	3/4	1/4	0
X_2	2(c)	1/4	1/4	0.63[1]

$CaAl_2Si_2$ type:

Space group: $P\bar{3}m1$; crystallographic parameters:

RE	1(a)	0	0	0
T	2(d)	1/3	2/3	0.63[1]
X	2(d)	1/3	2/3	0.27[1]

[1] free parameter in the structure